IMPROVED MODELING OF CAPACITIVE MICROMACHINED ULTRASONIC TRANSDUCERS (CMUTS)

A Dissertation

by

R. Erkan Kemal

Submitted to the

Graduate School of Sciences and Engineering

In Partial Fullfilment of the Requirements for

The Degree of

Doctor of Philosophy

In the

Department of Electrical and Electronics Engineering

Ozyegin University

May 2020

IMPROVED MODELING OF CAPACITIVE MİCROMACHINED ULTRASONIC TRANSDUCERS (CMUTS)

Advisor: Prof. Taylan Akdoğan

Co-Advisor: Dr. Goksen Goksenin Yaralıoğlu

Approved by:

Prof. Taylan Akdoğan, Advisor,
Department of Natural and Mathematical Science
Özyeğin University

Assoc. Prof. Ayhan Bozkurt,
Faculty of Engineering and Natural Sciences
Sabancı University

Assist. Prof. Ahmet Tekin,
Department of Electrical and Electronics Engineering
Özyeğin University

Assoc. Prof. Arif Sanli Ergün
Department of Electrical and Electronics Engineering
TOBB University of Economics and Technology

Date Approved:

Assist. Prof. Cenk Demiroğlu,
Department of Electrical and Electronics Engineering
Özyeğin University

ABSTRACT

Capacitive micromachined ultrasonic transducers (CMUTs) have been studied intensively in academia as well as in industry over the last two decades. Traditional ultrasound imaging technology mainly relies on piezoelectric transducers whereas CMUTs provide advantages such as providing wide bandwidth operation, ease of fabrication, potential to fabricate large 2D arrays, integration with IC and low cost.

With the design flexibility that CMUTs offer, it is possible to fabricate complex CMUT structures with different sizes and shapes including non-uniform membranes. This necessitates development of fast and accurate modeling tools for medical imaging community. In this thesis we demonstrate two methods that were developed to simulate the frequency of a CMUT, namely; Equivalent circuit models and finite element models (FEM). FEM provide very accurate calculations for various membrane geometries and evaluate the device performance. However, FEM analysis is much more time consuming compared to equivalent circuit models and it typically is not suitable for optimization where a series of simulations are required. Therefore, equivalent circuit models are preferred for the device optimization. There are several equivalent circuits models were presented previously. However, to be able to obtain frequency bandwidth accurately, anti-resonance of a CMUT must be included by the equivalent circuit. The first focus of the dissertation is to develop a new equivalent circuit model to simulate frequency bandwidth of a CMUT including anti-resonances.

The second aim of the dissertation is to design and simulate of ultra-wide bandwidth CMUTs for acoustic angiography applications. Currently, dual-frequency transducers are used for this application. In this process, two sets of transducers are

used; one of them transmits ultrasonic waves at low frequencies and the other one receives the harmonic waves of the incident ultrasound, which is coming from the tissue. The process requires precise designing the transducers bandwidths and hence is overly complex. Moreover, some of the information may be lost with undetected harmonics. Another difficulty arises due to the fact that it is difficult to align the transducers coaxially so that most of the generated ultrasound is detected by the receiver. However, if a transducer bandwidth can be increased enough, a single transducer can be used and hence both the design complexity of the process is reduced and more harmonics can be detected. Therefore, the second part of this thesis focuses to optimize plate size and geometry as well as electrode area to obtain maximum frequency bandwidth. Within the frame work of this dissertation, we demonstrated very high bandwidth transducers by introducing novel membrane geometries where we engineered the anti-resonance frequencies. Since the membrane geometry is not uniform the equivalent circuit model that was developed in the first part of the thesis is not accurate to estimate the bandwidth. Therefore, in the second part of the thesis, we used FEM analysis to design various membrane geometries to achieve very wide bandwidth.

ÖZETÇE

Kapasitif mikro işlenmiş ultrasonik dönüştürücüler akademide ve endüstride 20 yıldan fazla süredir yoğun olarak çalışılmaktadır. Geleneksel ultrasonic görüntüleme, piezoelektrik dönüştürücüler üzerine kurulmuştur. Ancak kapasitif mikro işlenmiş ultrasonik dönüştürücüler daha geniş frekans bantlı olmaları, kolay fabrikasyonu ve geniş 2 boyutlu üretilebilirliği, birleştirilmiş devreler ile uyumu, düşük maliyet özellikleri bakımından piezoelektrik dönüştürücülerden üstündür.

Kapasitif mikro işlenmiş ultrasonik dönüştürücülerin sağladığı dizayn rahatlığı ile, düzgün olmayan şekiller dahil olmak üzere farklı boyut ve geometrilerde kompleks dönüştürücüler üretilebilir. Bu durum medical görüntüleme topluluğunda hızlı ve doğru modelleme araçları geliştirilmesi gereğini doğurmuştur. Bu tezde, kapasitif mikro işlenmiş ultrasonic dönüştürücüler için geliştirilmiş olan iki method; eş değer devre ve sonlu element modellerini gösterdik. Sınırlı element modelleri farklı membran geometrilerini değerlendirip bu dönüştürücülerin performansını doğru bir şekilde verir. Ancak, bu method eşdeğer devre modellerine kıyasla oldukça uzun sürmektedir ve seri simülasyonların gerekli olduğu optimizasyon için uygun değildir. Bundan dolayı optimizasyon için eş değer devreler tercih edilir. Bir çok eşdeğer devre modeli sunulmuştur. Ancak frekans bandını doğru bir şekilde elde edebilmek için kapasitif mikro işlenmiş ultrasonic dönüştürücü anti-rezonansının eş değer devre tarafından eklenmesi gerekir. Bu tezin ilk amacı Kapasitif mikro işlenmiş ultrasonik dönüştürücülerin frekans bandını ve anti-rezonans frekanslarını gösteren yeni bir devre tasarlamaktır.

Tezin ikinci amacı ise akustik anjiyografi uygulamaları için ultra geniş frekans bantlı kapasitif mikro işlenmiş ultrasonik dönüştürücüler dizayn etmektir. Şuanda bu uygulama için çift frekanslı dönüştürücüler kullanılmaktadır. Bu işlemde iki set dönüştürücü kullanılır; Bir tanesi düşük frekansta ultrasonik dalga yollar, diğeri de ilk gönderilen dalganın hücreden gelen harmoniklerini algılar. Bu işlem dönüştürücülerin frekans bandının dikkatli şekilde ayarlanmasını gerektirir ve bundan dolayı oldukça komplekstir. Bazı bilgiler algılanamayan harmoniklerde kaybedilebilir. Diğer bir zorluk ise dönüştürücülerin ortak eksen üzerinde, alıcının oluşturulan ultrasonic dalgaların çoğunu algılayacağı biçimde yerleştirilmesidir. Bundan dolayı, eğer dönüştürücü frekans bandı yeterince geniş yapılabilirse, sadece bir tek dönüştürücü kullanılabilir ve böylece işlem daha az kompleks olur ayrıca daha fazla harmonic algılanabilir. Bundan dolayı tezin ikinci kısmı maksimum frekans bandı elde etmek için membrane geometrisini, boyutunu ve eletrot alanini optimize etmeye odaklanmıştır. Bu tez çerçevesinde, anti-rezonans frekansı üzerinde çalışarak yeni bir membrane geometrisi ortaya koyarak çok geniş bantlı dönüştürücü ortaya koyduk. Membran geometrisi düz olmadığı için bu tezin ilk kısmında geliştirdiğimiz eşdeğer devre bu dönüştürücü bandını doğru şekilde bulamamakta. Bundan dolayı tezin ikinci kısmında çok geniş frekans bandı elde etmek üzere farklı membran geometrileri dizaynı için sonlu elemet modeli kullandık.

ACKNOWLEDGEMENTS

First and foremost, I would like to express my gratitude to my co-advisor, Dr. G. Goksenin Yaralioglu for his invaluable guidance and to my dissertation committee member Dr. Ayhan Bozkurt for his consistent support and having his door open anytime for discussion.

I would like to thank my advisor Prof. Taylan Akdoğan and the other members of my committee, Assist.Prof.Ahmet Tekin, Assoc.Prof. Arif Sanli Ergün and Assist.Prof. Cenk Demiroglu. I would like to convey my appreciations to Prof. Taylan Akdoğan for helping and supporting me to complete my PhD degree. I would also like to extend my thanks to Prof.Ömer Oralkan for the opportunity of working closely with him and his research group when I was in North Carolina State University. It was the most educational and enjoyable time of my PhD degree.

I would like to reserve my special thanks for my friends, Hakan Çetin and Mohammed R. Sophani who have enriched my life in Özyeğin University.

Finally, I would like to express my deepest gratitude to my family. I cannot thank enough to them for all the sacrifices they have made for me to succeed in life. I am grateful for their endless support.

Last but not least, I would like to express my deepest gratitude to Tugce Kale. I consider myself lucky for having her in my life making every moment memorable and enjoyable.

TABLE OF CONTENTS

LIST OF TABLES

LIST OF FIGURES

CHAPTER I

INTRODUCTION

1.1. Overview of Ultrasound

The journey of ultrasound imaging had started in 1880, when Pierre Curie and Paul-Jacques Curie discovered the piezoelectric effect in certain crystals. Later, Paul Langevin developed piezoelectric materials, which can generate and receive mechanical vibrations with ultrasound. This discovery was used in navy to detect enemy submarines during WW1. Ultrasound in medical imaging was first used for therapeutic purposes in 1952 [1]. The first two dimensional ultrasound scan was obtained from a living subject in 1952 [2]. First commercial two dimensional ultrasonic scanner was described by Donald et al. [3]. Stuart Campbell described the B mode technique in 1968 [4]. Since then, researchers have been working on ultrasound and trying to improve its applications. Today, Ultrasound imaging is well known and intensively used technology in many fields including sonar, acoustic microscopy, nondestructive evaluation of materials & structures and medical imaging & therapy. Ultrasound is defined frequencies over 20 kHz up to several gigahertz whereas the diagnostic ultrasound imaging frequency typically ranges from 1 MHz to 20 MHz. Diagnostic ultrasound is used to visualize muscles, tendons and internal organs to investigate their structure such as cardiac structures [5], blood flow [6] as well as for any pathological or physical anomalies. In addition, much higher frequencies have been used in dermatology [7], small animals, and intravascular imaging [8]. Ultrasound imaging offers safe, cheap, portable and minimally invasive alternative to X-ray imaging, magnetic resonance and nuclear medicine imaging systems. The most crucial element of an ultrasound system is a transducer. There are two types of transducers used in medical imaging; piezoelectric transducers and capacitive micromachined ultrasonic transducers (CMUTs).

CMUT were invented in the mid-1990s [9] and have been intensively studied during the past two decades. Although piezoelectric transducers have been predominantly used to generate and detect ultrasound over the years, advances in microfabrication technology in recent years has made it possible to build CMUTs competing with piezoelectric transducers and hence, CMUTs have become a viable alternative to conventional piezoelectric transducers. First years of invention, research on CMUT was focused on fabrication methods [10-18]. Now it has been known that CMUTs have several manufacturing and performance advantages over piezoelectric transducers [19]. In addition, CMUT takes advantage of mature microfabrication techniques and therefore enables cost effective fabrication with small dimensions. Moreover, complex array structures easier to fabricate [20-25]. Furthermore, piezoelectric transducers have limited bandwidth while CMUTs are broadband devices. It has been shown that a CMUT with a very large bandwidth that exceeds 100% can be fabricated [21-34]. This makes them very attractive for medical imaging applications especially for contrast agent imaging [35]. 2D and 3D FEM were used to explain and understand CMUT behavior [39-50]. Moreover, there is several equivalent circuit models have been developed in the literature [51-59].

In this chapter, a brief introduction to ultrasound imaging is given and ultrasonic transducers namely piezoelectric and capacitive micromachined ultrasonic transducers are discussed.

1.2. Basics of Ultrasound Imaging

Ultrasound imaging operation starts with an electrical pulse excitation of a transducer. Then, the pulse is converted to acoustic waves by the transducer. This is referred as pulse mode. The emitted acoustic pulse travels through forward direction at the speed of sound in the medium. The echoes generated by the pulse are recorded by the transducer at echo mode (Figure 1). The received acoustic signals are converted to electrical signals by the transducer to construct the image.

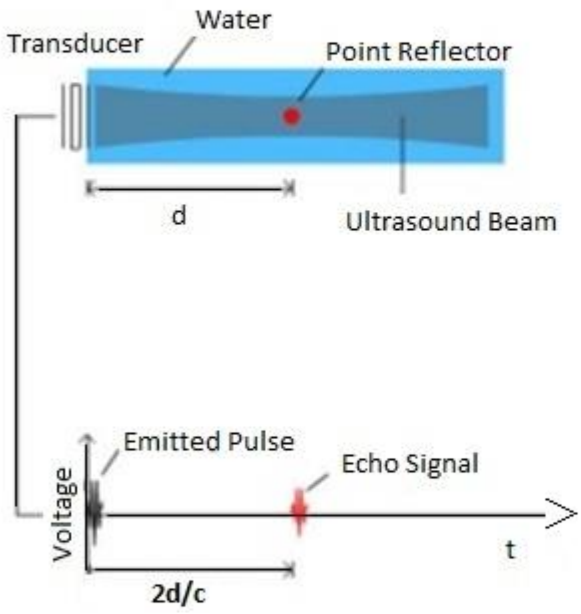

Figure 1: Pulse-Echo excitation of a ultrasonic transducer [61]

1.2.1. A - Mode Imaging

A-mode works by emitting a pulse and measuring the time and amplitude of the echo. This can generate information on the number of interfaces the wave has passed through. The display of amplitude spikes of different heights depending upon the tissues or interfaces. A-Mode consists of a x and y axis, where x represents the depth and y represents the Amplitude. When an ultrasound wave is transmitted to a body, due to discontinuity between transducer surface and the skin some of the transmitted waves are reflected back as shown in Figure 2. The reflected and transmitted wave amplitudes are functions of the density and sound speed of the medium. The transmitted signal propagates and reflects back towards the transducer. The echoes within a time frame are collected and electrical signals are turned to an image and hence amplitude mode (A-mode) image is constructed. The transducer is moved slightly and transmit-receive cycle is repeated to complete imaging.

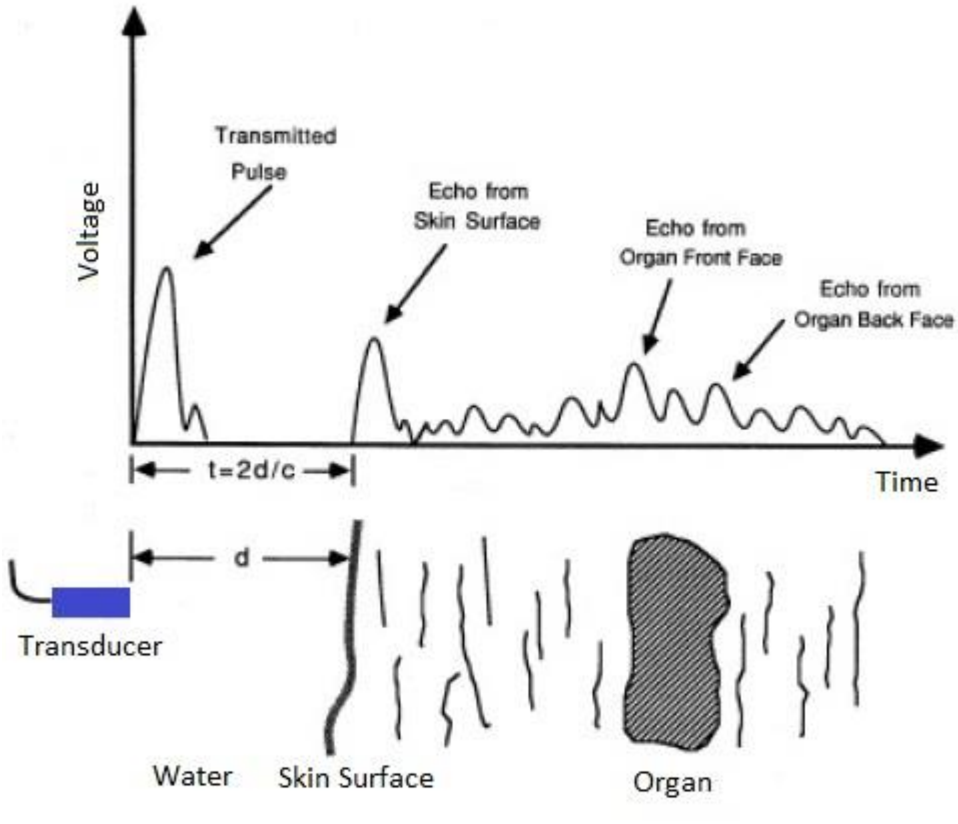

Figure 2: A-Mode imaging of a ultrasonic transducer [61]

Density of the different tissues and organs affects the reflected signals. If the difference in density is increased, the proportion of reflected sound is increased, which means that the proportion of the transmitted signal is decreased. If the density of the tissues is so different than each other, most of the transmitted signal is reflected back which causes acoustic shadowing. On the other hand, if there is no echo is produced means that there is no density difference between tissues. A-mode imaging is used in ophthalmology (eye length, tumors), localization of brain midline, liver cirrhosis, myocardium infarction.

1.2.2. B-Mode Imaging

B-mode (Brightness mode) images are obtained repeating A-mode imaging while moving transducer along x axis as shown in Figure 3. Unlike A-Mode, B-Mode is based on brightness and there are no vertical spikes. The brightness depends upon the amplitude or intensity of the echo. There is a z axis, which represents the echo intensity or amplitude, and x axis, which represents depth. The A-mode images are converted to gray scale images, where higher amplitude correspond to white, and lower amplitudes correspond to black.

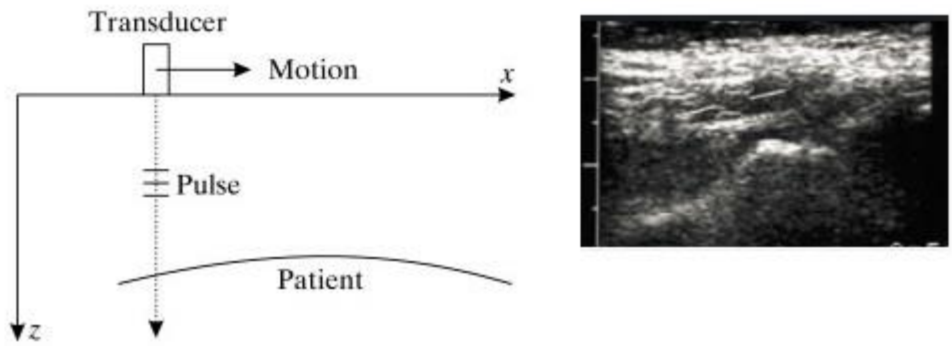

Figure 3: Brightness mode imaging of a ultrasonic transducer [61]

1.3. Imaging Technologies

There are mainly two ultrasound imaging systems; one is single element transducers (as explained above) and the other one is phased array systems. Phased array systems are formed with many transducer elements and have many advantages over single element systems. First of all, single element transducer systems suffer from limited imaging depth due to fixed focal point whereas phased array systems allow steering to intended directions and depths with focusing ultrasound energy [62]. On the other hand, in multi-element array, the echo must be received at the same time at the transducer interface. Due to the difference in path length, signals received from each element should be delayed to align the received signal as if they come to the surface of the transducer simultaneously. This process is referred as beamforming as shown in Figure4.

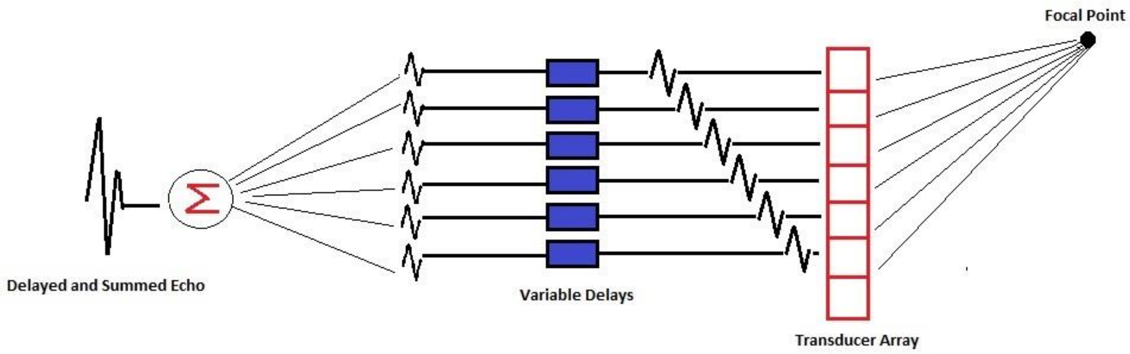

Figure 4: A beamforming system [63]

Moreover, with beamforming optimal focusing can be maintained over greater axial range, which enhances resolution for a greater depth with phased array systems.

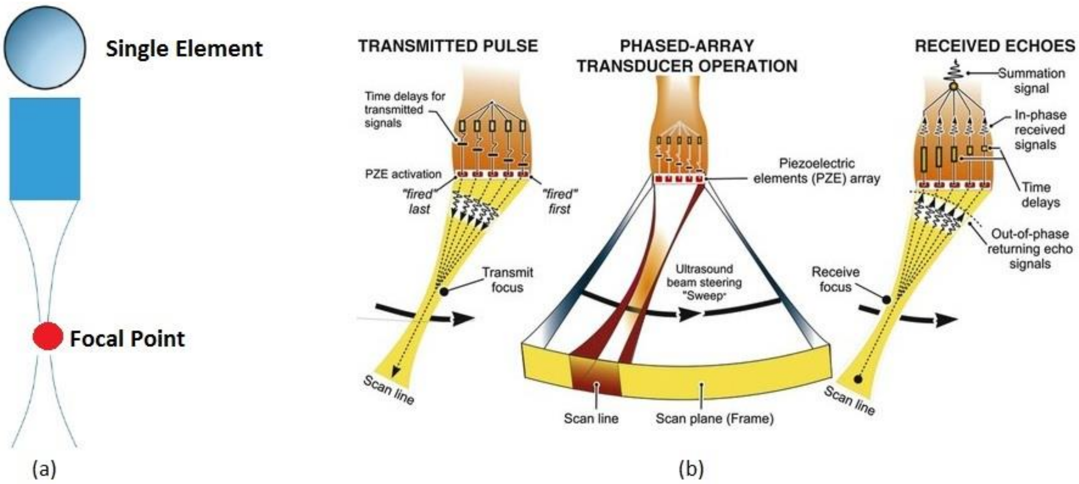

Figure 5: a) Single Element imaging, b) phased-array imaging [64]

1.3.1. Array Types

Arrays are composed of array elements and the array elements are composed of single cells. There are different type of arrays were developed depending upon the physical dimensions of the array structure. 1D, 1.25D, 1.5D, 1.75D and 2D arrays were proposed by various research groups [65-73].

1.3.1.1. 1D Phased Arrays

1D array transducers are used to obtain 2D images. The elements in 1D array are aligned along the azimuthal direction. 1D array is formed of long and thin transducers and the number of elements ranges from 32 to 128 [67-70]. There are 3 types of 1D array structures; a linear array, a convex array and a phased array as given in Figure 6. The 1D array structures have different imaging features. The method of acquiring the images from both linear and convex arrays is similar. However, image of the linear array has rectangular shape and operation frequency is higher. In convex array is used for deep imaging and hence the resolution can be poorer. When an object to be image is behind some obstacles, it is not possible to image the object and hence ultrasound beam must be steered using phased array. However, 1D array transducers cannot be used to image elevation direction. The image of the object is likely to be blurry out of the focal zone.

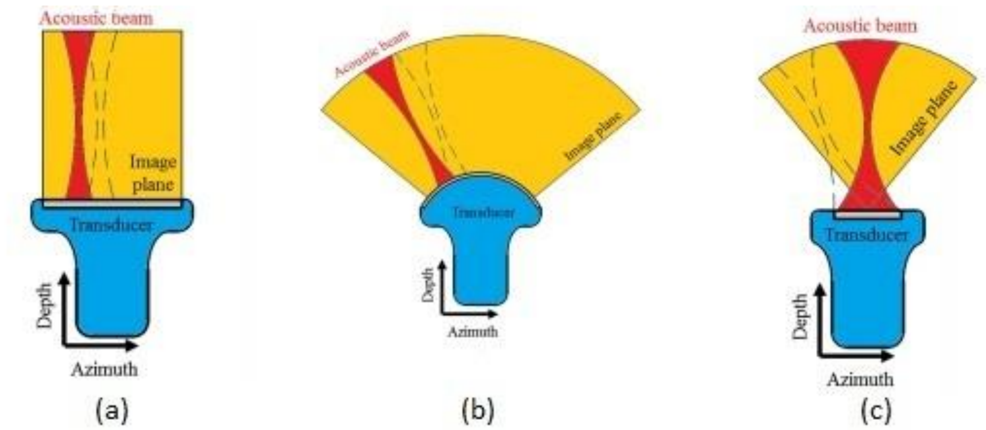

Figure 6: a) A linear array, b) a convex array, c) a phased array [66]

The first pulse-echo B-scan sector imaging using a 1-D CMUT array was presented by Oralkan et al. [67]. In the experiment, a 16-element portion of a 64-element 1-D CMUT array was used to generate ultrasound and receive echo signals. Later, Utkan et al. fabricated 64 and 128 element immersion 1D CMUT arrays [68]. Oralkan et al. presented the first pulse-echo phased-array B scan sector images using a 128-element 1D linear CMUT array. They also investigated the preliminary analysis of the effects of crosstalk between array elements [69]. Mills et al. fabricated 1-D CMUT arrays using the wafer-bonding [70].

1.3.1.2. 1.25D, 1.5D and 1.75D Arrays

To modify ultrasound beam on the elevation and depth 1.25D, 1.5D and 1.75D array transducers have been developed [71]. These arrays are intermediate between 1D and 2D arrays and have been used to reduce the numbers of elements relative to a fully populated 2-D array. The elements are formed along the elevation direction in addition to azimuthal direction. The addition of the extra rows enables a limited amount of steering of the imaging plane in the y–z plane. These arrays each sub-element electronically is delayed to focus in the elevation direction.

1.3.1.3. 2D Arrays

3D ultrasound images are obtained using two approaches. In the first approach 1D array is scanned over a volume mechanically and obtained multiple 2D images are rendered over a volume. This is very time consuming and prone to motion artifacts. In the second approach 2D arrays are used. The 2D arrays consist of much more elements than 1D array and those elements are arranged both azimuthal and elevation directions. Therefore, volumetric data can be obtained instantly. However, due to large number of transducer, it has the maximum complexity. There are researches to solve this complexity issue. Due to transducer array elements are densely packed together, the electrical connections must be supplied from the back side of the array elements. Special designed connector to join pads was designed for integrated circuits. Multilayer ceramic connector was developed by Smith et al [74]. Later, Multi-flex layer circuit made from polyimide thin films was used [75]. CMUT was directly fabricated on the electronics [76], [77]. A 128×128-element 2-D array was fabricated by Oralkan et al. The electrical connections were sustained from a through-wafer via interconnects [78].

3-D imaging results were obtained using a 8×16 element portion of this array. A 16 × 16-element capacitive micromachined ultrasonic transducer (CMUT) array for 3-D ultrasound imaging by Wygant et al. and Zuhang et al. [79, 80]. Photoacoustic imaging was performed using 16 × 16 CMUT array [81]. Bhuyan et al. fabricated a 32×32-element 2-D array CMUT to increase resolution [82].

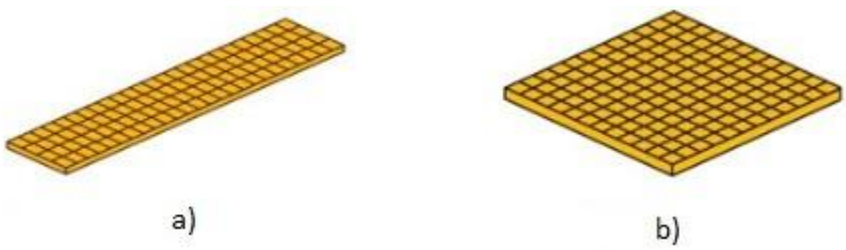

Figure 7: a) 1.5D array, b) 2D array [83]

1.3.1.4. Annular Arrays

Annular arrays were fabricated for high frequency imaging [84], high intensity focused imaging [85], photo acoustic imaging [86] and intravascular imaging [87, 88]. Annular transducers (Figure8) have advantages over the other transducer designs. They have dynamic focusing capability and hence they provide larger depth. Moreover, they need fewer elements than linear phased array transducers to form an image yielding improved SNR [89]. Due to their structure, they can form symmetrical beam unlike linear arrays [89]. On the other hand, beam steering is not possible and focusing is limited with these transducers.

Figure 8: An annular array. There are 7 elements in this array.

1.3.1.5. Other Array Types

Various alternative array structures have been suggested. Transducer elements are arranged in a series three concentric circles by Martinez et al. [90] as shown in Figure 9(a). Also Norton et al [91] designed a single circle (Figure 9b). The Mill cross structure in Figure 9c was proposed by Mondal et al. [92].

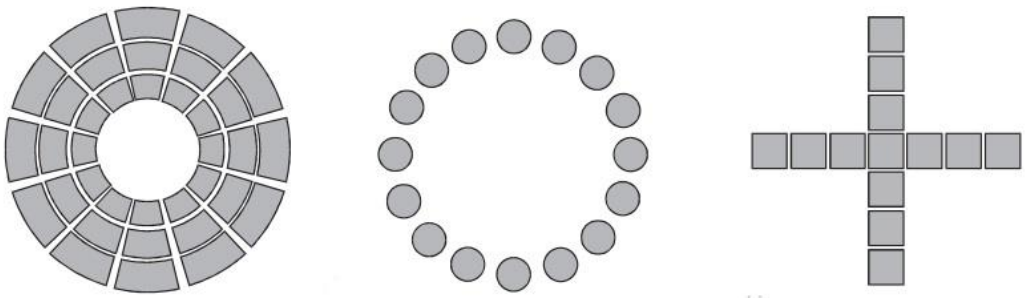

Figure 9: a) Three concentric circle array, b) Annular array, c) The mill cross array [93]

1.3.2. Image Resolution

To be able to distinguish the features in the image, the imaging resolution must be high enough. In order to sustain that, the pulse length must be kept smaller than the thickness of the feature that is intended to image. Shorter transmitted pulse length results in better axial resolution for an imaging system whereas a transducer is limited with its bandwidth. Therefore, transducers with a large bandwidth is necessary for medical imaging systems to achieve greater resolution. In addition to axial resolution, the lateral resolution is another quality parameter for an image construction. Lateral resolution determines the minimum distance the image system can resolve between two features in the image. It is a function of the transducer geometry such as transducer size and curvature. The width of the transmitted beam determines the lateral resolution.

1.3.2.1. Axial Resolution

Minimum separation between structures within the image is determined with spatial resolution. Spatial resolution is categorized into axial and lateral resolution. Axial (longitudinal or azimuthal) resolution is referred as the direction that is parallel to the acoustic wave propagation. Axial resolution is given as;

$$Axial\ Resolution = \frac{Nx\lambda}{2} \qquad [173]$$

Where N is the number of cycles in the pulse and λ is the wavelength of the transmitted signal. Axial resolution can be increased with higher bandwidth, since the duration (number of the cycle) of the transmitted pulse is reduced.

1.3.2.2. Lateral Resolution

Lateral resolution is the resolution that is perpendicular to the direction of the ultrasound beam. Unlike axial resolution, lateral resolution depends on the distance from transducer because diameter of the beam is important. When the beam diameter is smallest at a point, which is defined as focal point, the lateral resolution is maximized because wider beams diverge further in the far field and any ultrasound beam diverges at greater depth. Lateral resolution is given as;

$$Lateral\ Resolution = \frac{F\ x\ \lambda}{D} \qquad [173]$$

where F is the distance of focal point and D is the transducer diameter.

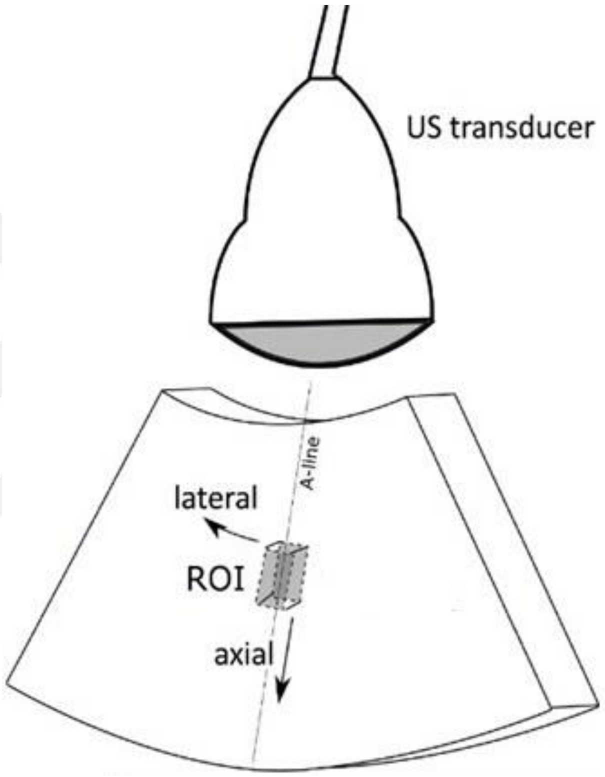

Figure 10: Axial and Lateral resolution [94]

In addition to axial and lateral resolution, frame rate is also important parameter for real time imaging systems because frame rate is the ability to detect that an object has moved over time. If the receive period is too long, frame rate is naturally small. The duration of each transmit-receive cycle depends on the imaging depth. The echoes from the deepest tissue has to come back to complete the cycle. For example, if imaging depth is 20 cm, each receive period must be at least ≈ 270 micro-seconds. This indicates a tradeoff between the image frame rate and the imaging depth.

1.4. Ultrasonic Transducers

The most crucial component of an ultrasound imaging system is a transducer component. An ultrasonic transducer is an electromechanical device that converts electrical energy to ultrasound waves or vice versa. There are two types of transducers available for ultrasonic imaging systems; Piezoelectric transducers and CMUT.

1.4.1. Piezoelectric Transducers

Piezoelectricity was discovered by Nobel Lauretes, Pierre and Jacques Curie in 1880 [95]. During WWII Barium titanate was developed for sonar applications [96]. In 1952, lead zirconate titanate (PZT) was discovered and has become the mostly used piezoelectric material ever since due to strong piezoelectric properties it possesses (d33 > 2500 pC/N). However, PZT material contains lead oxide, which is highly toxic. Therefore, new lead oxide free materials have been developed such as bismuth titanate (BTN) [97], bismuth potassium titane (BKT) [98] and potassium sodium niobate (KNN) [99] whereas these materials suffer from low piezoelectric properties and corrosiveness. More recently, barium zirconate titanate-barium calcium titanate (BZT-BCT) based piezoelectric materials have been developed with higher piezoelectric properties (d33 > 600 pC/N) [100].

Piezoelectric effect can be described as the ability of developing electrical charge proportional to an applied mechanical stress. An electric potential can be induced if a material with a piezoelectric properties is mechanically strained either in compression or tension [101]. This is defined as a direct piezoelectric effect. An applied mechanical stress shifts the positive and negative charge centers resulting electrical field (Figure 11a and 11b). Conversely, piezoelectric material shrinks or expands if a voltage is applied (Figure 11c and 11d).

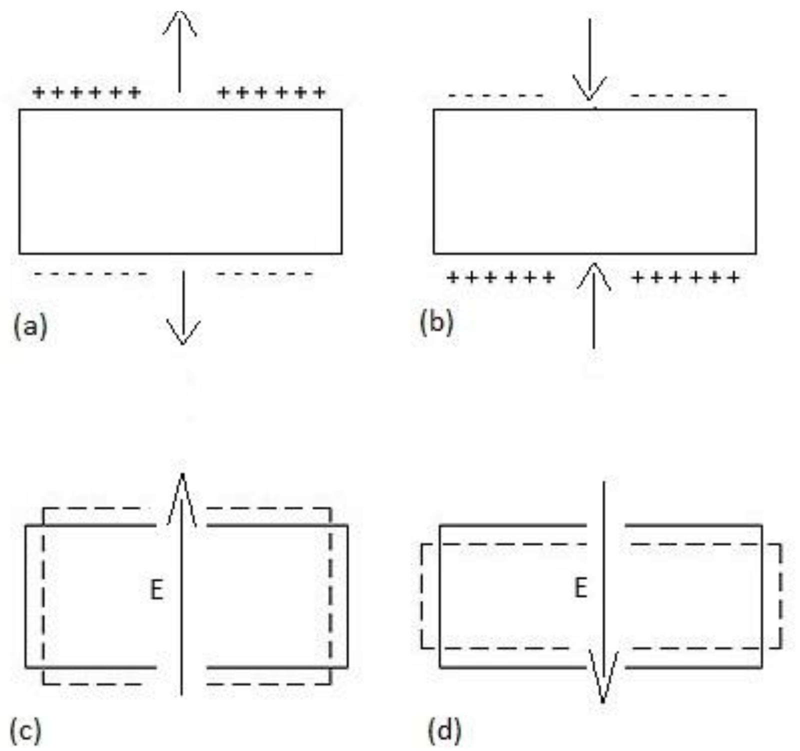

Figure 11: Piezoelectric effect; (a) effect of tensile stress, (b) effect of compressive stress, c) effect of application of electric field, d) effect of reversing application of electric field [101]

Today, the transducers which are used in clinic applications are mostly made from piezoelectric material. The most common piezoelectric material in medical systems is PZT which is a polycrystalline ferroelectric ceramic material. PZT crystallites have microscopic domains in which elementary cell dipoles arbitrarily distributed and hence material shows no piezoelectric properties. The material must be exposed to a strong electrical field which aligns the dipoles in the direction of applied electric field. The dipoles maintain this orientation even after the electric field is cut off. This process is referred as polarization as shown in Figure 12.

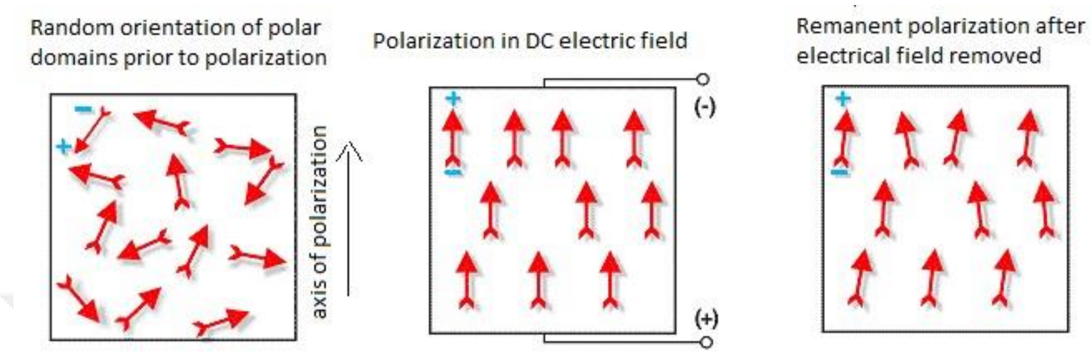

Figure 12: Polarization of a ferroelectric material [102]

Moreover, a ferroelectric material is a material that exhibits piezoelectric effect within a certain temperature range. At temperatures below the Curie temperature T_C, the lattice structure of the PZT crystallites becomes distorted and asymmetric. Therefore, dipoles can be formed. Above the Curie temperature the piezoceramic material loses its piezoelectric properties [103]. PZT is used for various applications such as actuators and sensors, sonar transducers for naval applications, flow control, fuel injector systems and energy harvesting [104-109].

In addition to PZT, piezoelectric polymers have been used in ultrasonic transducer applications [110] due to several advantages of this material including moderately wide frequency bandwidth, flexibility and inexpensiveness. Later, piezoelectric composite materials were produced. These composites have higher coupling coefficient and better impedance matching than PZT. Therefore, their sensitivity and bandwidth are higher than PZT [111].

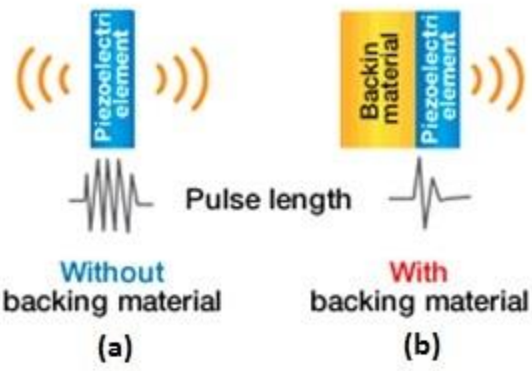

Figure 13: Affect of backing material [112]

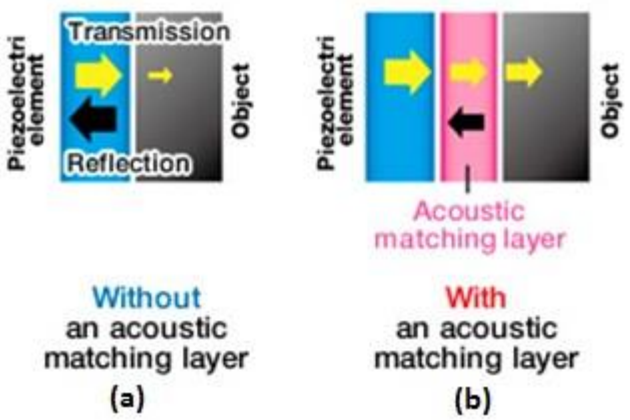

Figure 14: Affect of a matching later [112]

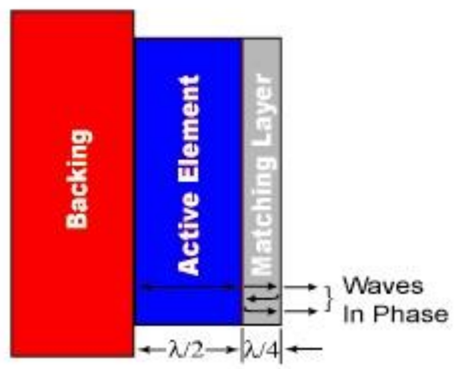

Figure 15: Basic structure of a piezoelectric transducer [113]

An ideal transducer is expected to have impedance which matches perfectly to human body, high sensitivity and wide transducer bandwidth. When a piezoelectric transducer is driven by an electrical pulse, it rings at its natural frequency. The generated energy can radiate both forward and reverse direction (Figure 13a). Therefore, to direct the generated energy to forward direction a backing material is needed. Backing materials absorbs the energy and hence reduce ringing as shown in Figure 13b. Acoustically lossy materials are preferred for this purpose. Backing materials have great influence on transducers and are used to damp out the ringing and to increase bandwidth. If the mismatch in impedance between the active element and the backing material increases, sensitivity is reduced. Therefore, the most suitable backing materials must have acoustic impedance similar to active elements that is used. Moreover, due to mismatch in acoustic impedance between piezoelectric transducer and a medium (air or tissue), most of the acoustic energy at the interface moves back to piezoelectric material as shown in Figure 14a. Therefore, an intermediate material is needed between piezoelectric material and a medium and hence ultrasonic waves can enter the object to be image as shown in Figure14b. Piezoelectric element is usually cut to ½ to desired wavelength and for optimal impedance matching thickness is ¼ of the desired wavelength [114] (Figure 15) as explained below.

$$\Delta P_{1\rightarrow} = Z_1 v_{\rightarrow} \qquad (i)$$

$$\Delta P_{1\leftarrow} = Z_1 v_{\leftarrow} \qquad (ii)$$

$$\Delta P_1 = \Delta P_{1\rightarrow} + \Delta P_{1\leftarrow} \qquad (iii)$$

$$v_1 = v_{\rightarrow} + v_{\leftarrow} \qquad (iv)$$

$$\Delta P_{1\rightarrow} + \Delta P_{1\leftarrow} = \Delta P_2 \qquad (v)$$

Where $\Delta P_{1\rightarrow}$ and $\Delta P_{1\leftarrow}$ are pressure differences going in and out from a medium (2)

$$\frac{\Delta P_{1\rightarrow}}{Z_1} - \frac{\Delta P_{1\leftarrow}}{Z_1} = \frac{\Delta P_2}{Z_2} \qquad (vi)$$

Multiplying (ii) with Z_1;

$$\Delta P_{1\rightarrow} - \Delta P_{1\leftarrow} = \frac{\Delta P_2}{Z_2} Z_1 \qquad (vii)$$

and summing up (i) and (iii);

$$2\Delta P_{1\rightarrow} = \frac{\Delta P_2}{Z_2} Z_1 + \Delta P_2 \qquad (viii)$$

$$\Delta P_2 = \frac{2Z_2}{Z_1 + Z_2} \Delta P_{1\rightarrow} \qquad (ix)$$

It is known that transmitted pressure (Pt) to the incident pressure (Pi) is calculated as;

$$\frac{P_t}{P_i} = \frac{2Z_2}{Z_{1+}Z_2} \qquad (x)$$

And the ratio of transmitted intensity (It) to the incident intensity (Ii) is equal to;

$$\frac{I_t}{I_i} = \frac{4Z_1Z_2}{(Z_1 + Z_2)^2} \qquad (xi)$$

The equations should be modified for three layers (a transducer surface to matching layer and to tissue) as;

$$\frac{P_t}{P_i} = \frac{4Z_M Z_L}{(Z_M + Z_T)(Z_L + Z_M)} - \frac{4Z_M Z_L (Z_L - Z_M)(Z_T - Z_M)}{(Z_M + Z_T)^2 (Z_L + Z_M)^2} + \frac{4Z_M Z_L (Z_L - Z_M)^2 (Z_T - Z_M)^2}{(Z_M + Z_T)^3 (Z_L + Z_M)^3}$$

$$= \frac{4Z_M Z_L}{(Z_M + Z_T)(Z_L + Z_M)} \frac{(Z_M + Z_T)(Z_L + Z_M)}{(Z_M + Z_T)(Z_L + Z_M) + (Z_L - Z_M)(Z_T - Z_M)}$$

$$= \frac{2Z_M Z_L}{Z_T Z_L + Z_M^2} \qquad (xii)$$

$$\frac{I_t}{I_i} = \frac{p_t^2 / Z_L}{p_i^2 / Z_T} = \frac{4Z_M^2 Z_L Z_T}{(Z_T Z_L + Z_M^2)^2} \qquad (xiii)$$

The equation above is equal to '1' when; $Z_M = \sqrt{Z_T Z_L}$

For immersion medium transducers, the matching layers' impedances are kept between the impedance of the immersion medium and active element.

Table 1: Acoustic Impedances

Material	**Impedance ($\frac{kg}{m^2 s}$)**
PZT	33.7×10^6
Air	400
Water	1.5×10^6
Fat	1.38×10^6

Piezoelectric transducers are made from a crystal rod and require intensive fabrication steps. The crystal rod is diced out using a saw. This limits the smallest feature size due to aspect ratio of the elements after dicing. For high frequency applications, the wavelength becomes smaller and required precision on the production increases and hence the cost rises. Capacitive micromachined ultrasonic transducers are better alternatives for ultrasonic imaging offering ease of fabrication, low cost, wide frequency bandwidth and integration with IC.

1.4.2. Capacitive Micromachined Ultrasonic Transducers (CMUTs)

CMUTs are basically capacitors that consist of a movable plate that is anchored around its edges and suspended over a vacuum gap as shown in Figure 16.

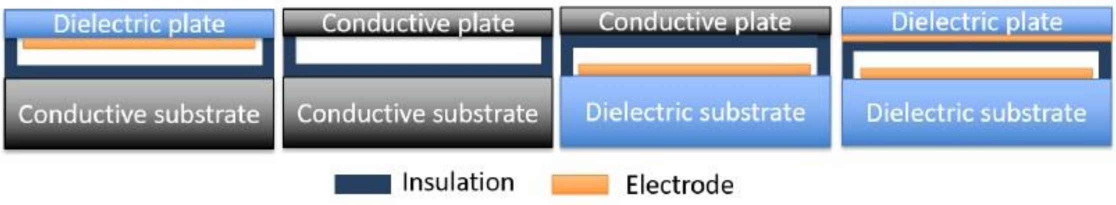

Figure 16: CMUT structures [115]

The movable top plate itself or a metal layer, which can be made partially or completely conductive, on top of forms the top electrode. There is layer at the bottom that acts as a bottom electrode and hence a capacitor is form with a gap between these two conductive layers. When a DC voltage is applied between the two electrodes, the top electrode is attracted toward the substrate due to electrostatic force. A resistive force to the electrical force is built up by the stiffness of the plate. An alternating voltage is applied and hence ultrasound is generated. On the other hand, if the movable plate is subjected to ultrasound, an electrical current is generated because of the change in capacitance. These operation modes are called transmit and receive, respectively.

Table 2: Comparison of piezoelectric transducers and CMUTs

	Piezoelectric Transducers	CMUT
Fabrication method	Dicing	Silicon micromachining
Array fabrication	Difficult for 2D and high frequency arrays	2D arrays can be fabricated with through wafer interconnections
Frequency bandwidth	Moderate, matching layers required	Wideband, no need for matching layer
Array uniformity	Moderate	High
Thermal stability	Low	High
IC integration	Difficult	Monolithic or hybrid integration
Output pressure	High	Relatively low

1.4.2.1. Basics of a CMUT

CMUTs offer many advantages over piezoelectric transducers and hence they become very competitive for medical imaging with piezoelectric transducers over the years. Powerful computing tools (FEM) and equivalent circuit models have been developed to simulate the behavior of a CMUT [38-49]. FEM can provide accurate calculations and explain the nonlinearities of a CMUT. There are various FEM tools such as ANSYS, COMSOL, CONVENTOR, etc. Equivalent circuits simplified the design of a CMUT and helped to find out important parameters much faster [51-59]. Analogy between mechanical and electrical domains is used to convert mechanical systems into electrical circuits. Forces in mechanical domain can be converted into voltage sources, velocities to electrical currents, damping factors to resistors, masses to impedances and spring constant can be converted to capacitors. This methodology is how the equivalent circuit models are made for a CMUT. After that, CMUT interconnection and integration with electronics were studied [116, 117]. More recently, CMUTs have started to be used in industry. Hitachi introduced super-wide bandwidth CMUT (2MHz-22MHz) [118]. Also, Kolo Medical fabricated high and low frequency Linear CMUT arrays with center frequencies 30MHz and 15MHz, respectively [119]. According to Yole Development, market research and strategy consulting company, around 25-30% of the medical imaging systems will use CMUT by 2023 and hence CMUTs can be the next big MEMS product in the medical field [120]. The progress regarding CMUTs is depicted below in Figure17.

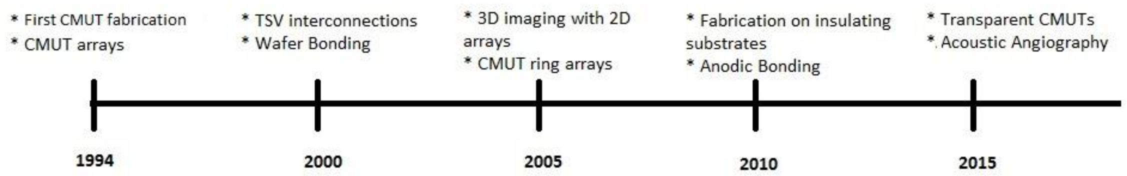

Figure 17: Timeline of a CMUT evaluation

1.4.2.2. CMUT Characterization

The first step of characterization of a CMUT is to measure input impedance. Resonant frequency, quality factor, device capacitance and static collapse voltage can be determined with the help input impedance. The real part of the input impedance peaks at the open circuit resonant frequency. The input impedance is measured with using an impedance analyzer or a network analyzer. A bias T (Figure 18) is needed to superimpose AC voltage on top od DC bias on a CMUT.

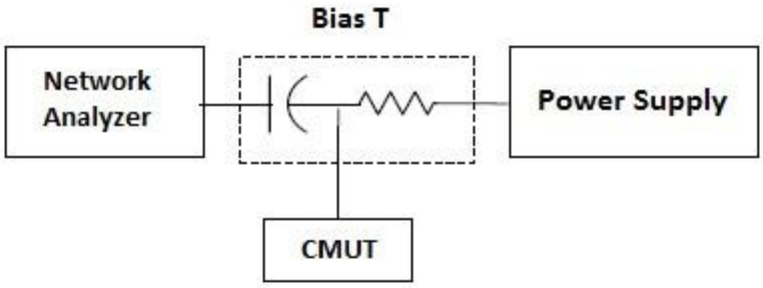

Figure 18: Bias-T circuit

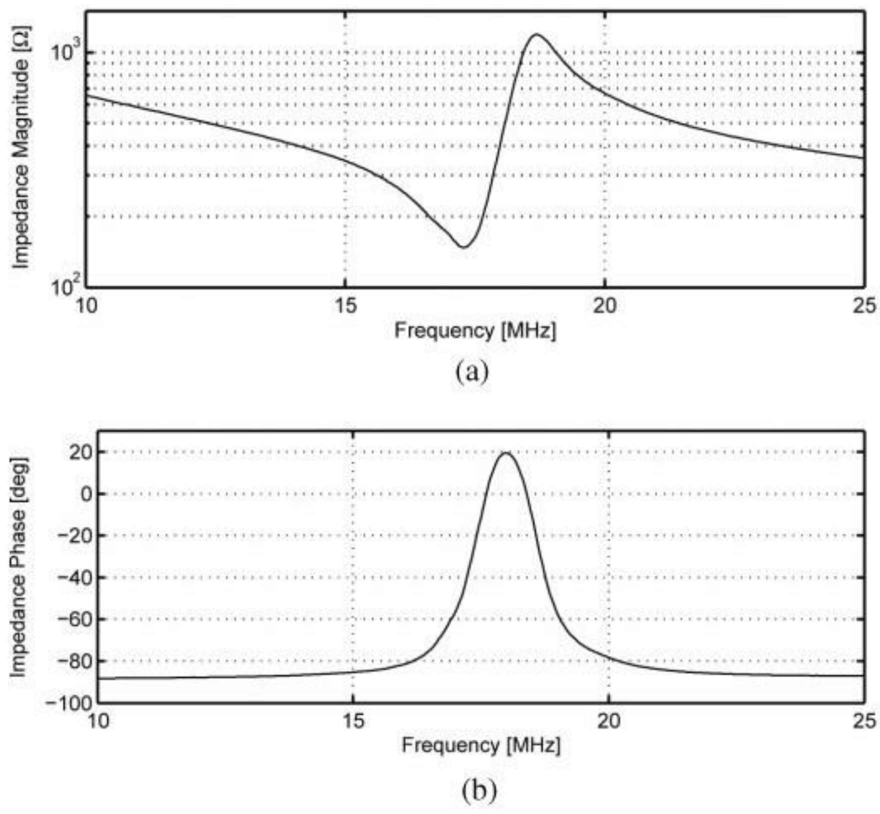

Figure 19: An Electrical impedance example of a CMUT a) Impedance Magnitude, b) Impedance phase [174]

Resonance frequency is decreased with increased DC bias. Also, due to higher transduction efficiency the amplitude of the resonance peak increases. Moreover, when the electrostatic force overcomes mechanical restoring force, a sudden increase in resonance frequency is observed as shown in Figure 19. This is due to much stiffened plate spring [121] and hence the collapse voltage can be determined experimentally by observing this change.

1.4.2.3. CMUT Characterization in immersion

In medical imaging, CMUTs are used in contact with tissue. Therefore, water or oil medium is used to characterize a CMUT due to their impedance which is close to tissue. The behavior of a CMUT is determined using pulse-echo measurement as given in Figure 20. CMUT is biased with a DC voltage and electrical excitation pulse is superimposed on top of the DC voltage. Fluid-air interface away from couple of centimeters away from the CMUT reflects acoustic waves. These reflected acoustic waves come back to the CMUT and change the CMUT capacitance due to voltage change across the CMUT. This electrical signal then is read by the oscilloscope and with the application of the Fast Fourier Transform bandwidth can be obtained as shown in Figure 21. It should be noted that the bandwidth must be corrected for medium, diffraction and excitation pulse shape.

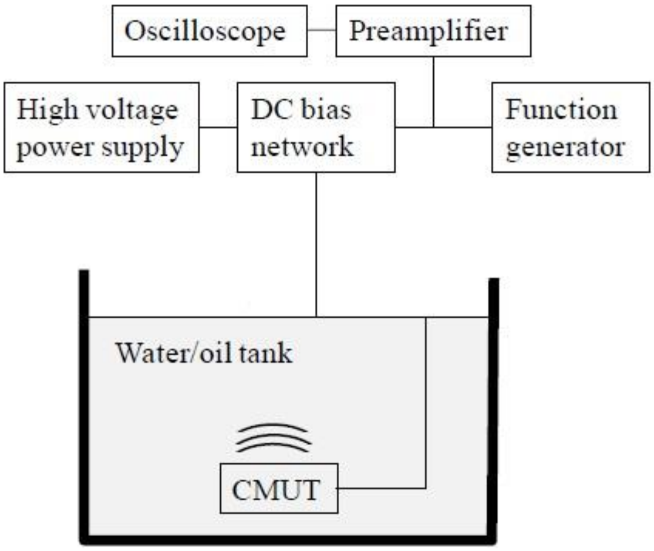

Figure 20: An experimental setup of an imaging system

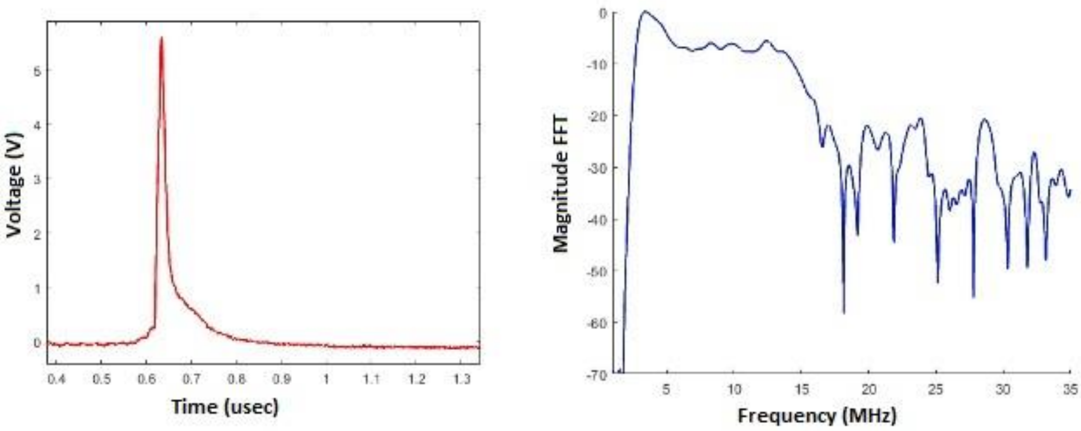

Figure 21: An example of applied pulse and corresponding output pressure vs frequency data of a CMUT [177]

1.4.2.4. Fabrication Methods

There are two main fabrication methods have been developed, namely; sacrificial release process [9] and wafer bonding process [122].

1.4.2.4.1. Sacrificial release process

Sacrificial layer process is the first process that was developed to fabricate a CMUT [9] and the process is widely used because the surface micromachining approach is compatible with the IC fabrication process [126].

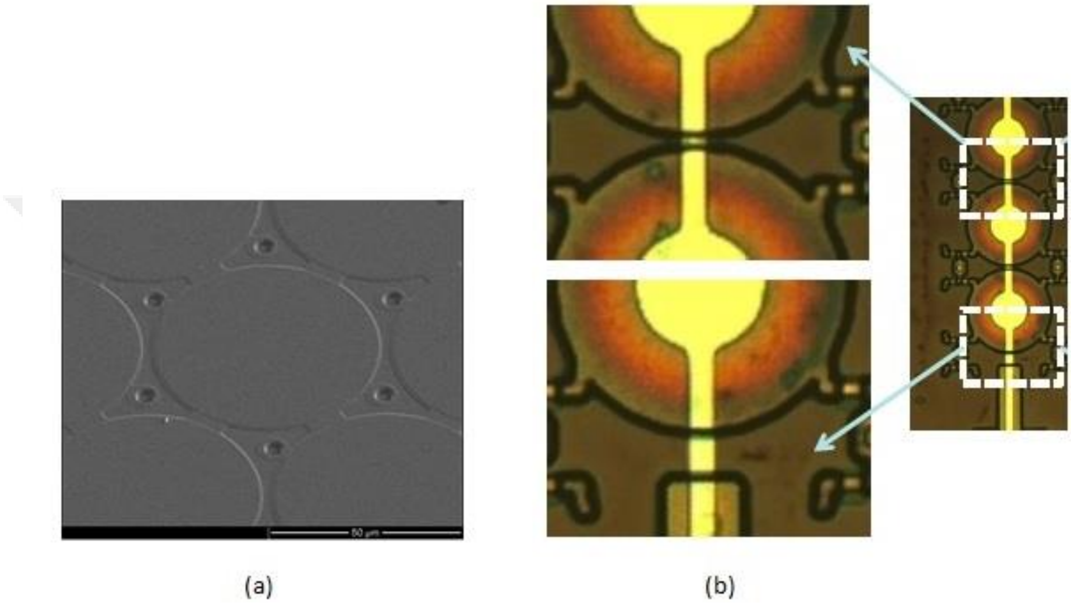

Figure 22: a) A CMUT that is fabricated with sacrificial layer method [123], b) Bottom electrode of a CMUT [124].

The process relies on forming a cavity by depositing sacrificial layer on the substrate and then selectively removing the sacrificial layer on the substrate using appropriate etchants. The sacrificial layer is chosen such that the etchant only removes the sacrificial layer without etching the plate layer underneath. A variety of sacrificial layers were used; nitride membrane with an oxide sacrificial layer [125], a polysilicon membrane with an oxide sacrificial layer [11], nitride membrane with a polysilicon sacrificial layer [15]. Later, to achieve a better etching selectivity, silicon nitride membrane with amorphous silicon sacrificial layer were used [12]. Cianci et al., reported metal sacrificial layer which has an excellent etching selectivity against silicon nitride [17]. The first step of fabrication is to clean the wafer. Then, bottom electrode is deposited (Figure 23a). After that, photoresist is deposited and patterned (Figure 23b). Next, sacrificial layer is deposited (Figure 23c). Photoresist is removed Figure 23d. Then, generally Silicon Nitride is deposited to form top plate (Figure 23e). In the next step, top electrode is deposited. On the other hand, the membrane can be highly connective (if doped) and hence can be used as top electrode (Figure 23f). Holes are defined into the nitride later to reach the sacrificial layer (Figure 23h). Appropriate etchant is used depending upon the sacrificial layer is used (Figure 23.i). The holes are sealed with low pressure chemical vapor deposition of silicon nitride. Sacrificial layer process is simple, and it can be done low temperature (~250^0C) which allows CMOS integration [127]. The major disadvantages of the sacrificial release process are the poor control over uniformity, plate thickness, gap height and residual stress [127].

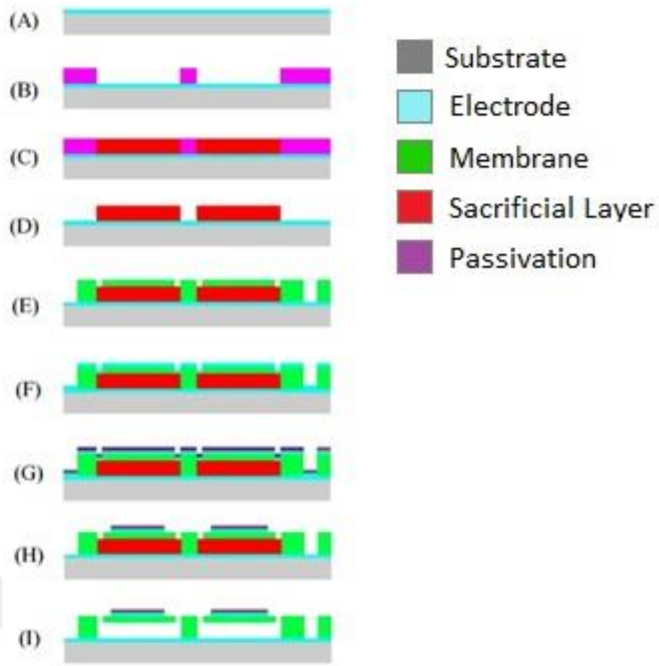

Figure 23: Sacrificial Layer process

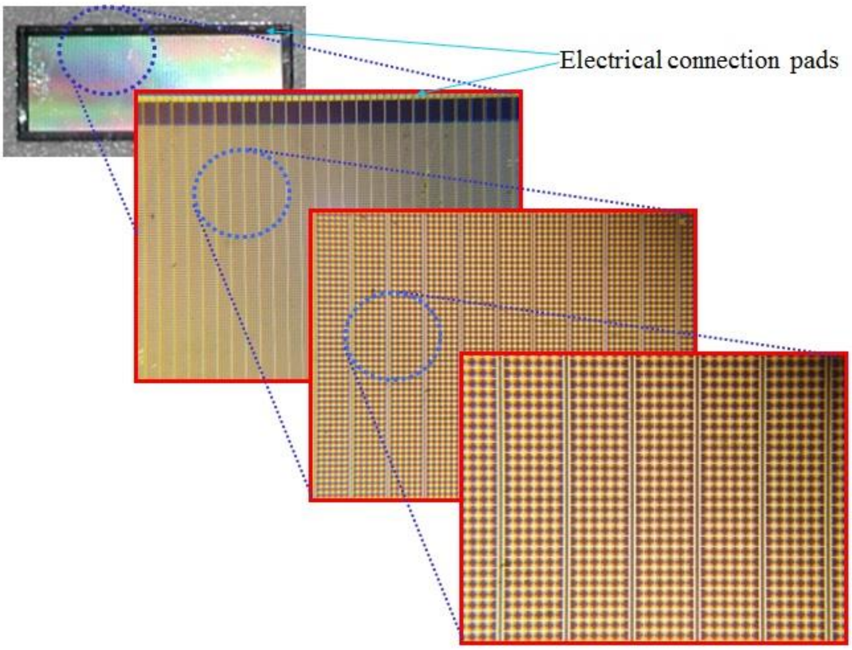

Figure 24: Typical CMUT array

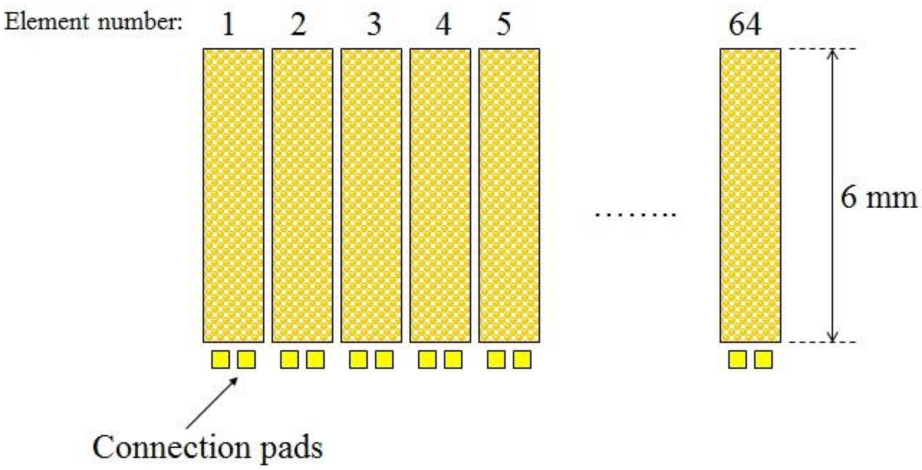

Figure 25: Schematic drawing of the array shown in Figure 24.

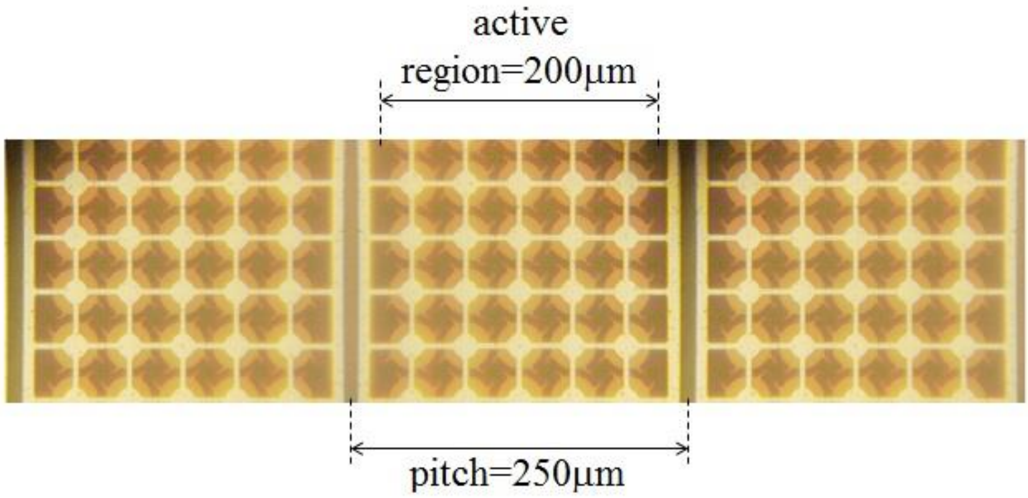

Figure 26: Zoomed version of the picture shown in Figure 24.

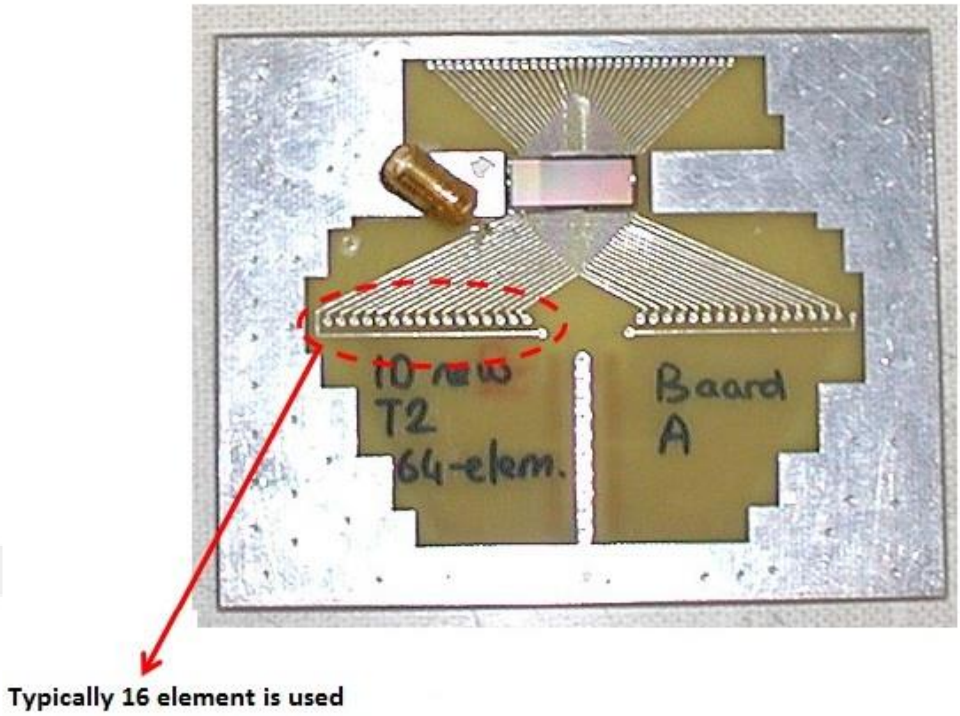

Figure 27: A typical fanout PCB used for the array shown in Figure 24.

1.4.2.4.2. Wafer through via

Electrical connectivity can be sustained from the back side of the membrane with adding couple of process steps. This process is called through wafer via [128-130]. The process allows controlling CMUT elements individually and hence it is important for the fabrication of the 2D arrays in which transducer elements are densely populated. Many processes have been previously used to fabricate through-wafer interconnects. T. R. Anthony proposed several techniques including capillary wetting, wedge extrusion, wire insertion and electroplating, electroless plating, electroforming, double-sided sputtering and through-hole electroplating [131]. The techniques based on laser drilled holes on wafer and the techniques were not suitable for small interconnections ($> 100um$) and densely populated elements. Later, dry etched polysilicon filled interconnects by Chow et al [132]. A double sided polished Silicon wafer is used for through Wafer via process. The etching is done half way from both sides. The side walls and wafer front and backside pads are grown thermal oxide layer. Then, polysilicon is deposited and heavily doped to enchance conductance. A layer of LTO is deposited to serve as an etch stop. The holes are filled with polysilicon.

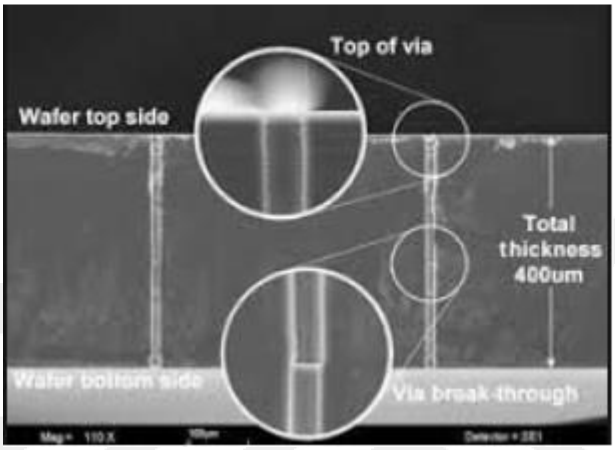

Figure 28: Wafer through via [133]

1.4.2.4.3. Wafer Bonding

Wafer bonding was first developed by Huang et al. [122]. The method simplifies the fabrication of a CMUT. In wafer bonding technique, there are two wafers; one is silicon wafer and the other one is silicon on insulator (SOI) wafer. The first step is to clean the wafer (Figure 29a) and then grow silicon dioxide on the wafer (Figure 29b). Then, using photolithography the oxide layer is patterned (Figure 29c) and followed by a second thermal oxidation to form the insulation layer (Figure 29d). After cleaning the surface, the SOI wafer and prime wafer are brought together in vacuum (Figure 29e). The bonded wafer is annealed at ~1000^{o}C. The top portion (the handle layer) of the SOI wafer and buried oxide layer are removed (Figure 29f and 29g). After that, the silicon layer is patterned to open via through the top layer to contact the bottom electrode (Figure 29h). Top electrode is deposited and then patterned (Figure 29i and 29j).

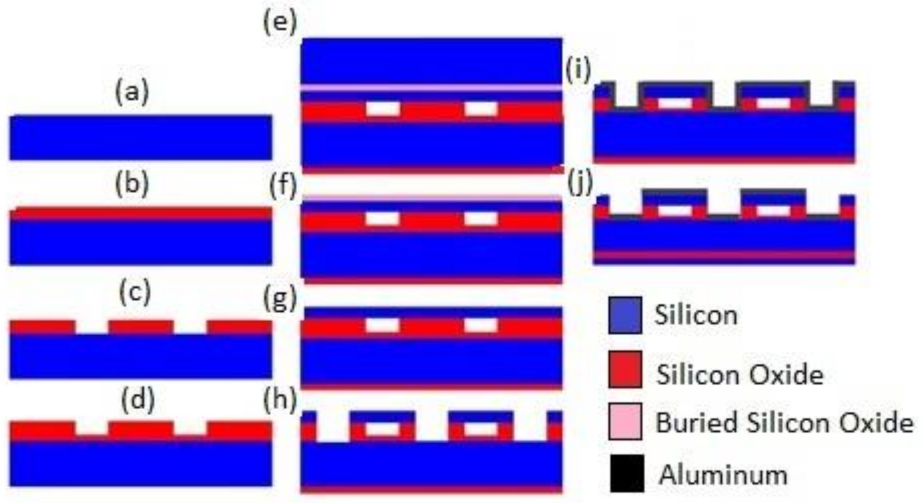

Figure 29: Wafer bonding process; a)Prime wafer, b)thermal oxidation, c)etching the cavity, d)thermal oxidation, e)SOI wafer bonding, f)SOI handle etching, g)etching buried oxide layer, h)patterning for metallization, i)metallization, j)metal patterning

There is also LOCOS (local oxidation of silicon) process which is another form of wafer bonding method. LOCOS is used to grow oxide at the specific locations and hence reduced parasitic capacitance as well as control gap height [134]. However, LOCOS process is not suitable for 2D arrays. Therefore, only the bottom electrode region can be isolated as shown in Figure 30. Also, the capacitance in the post region can be minimized [134].

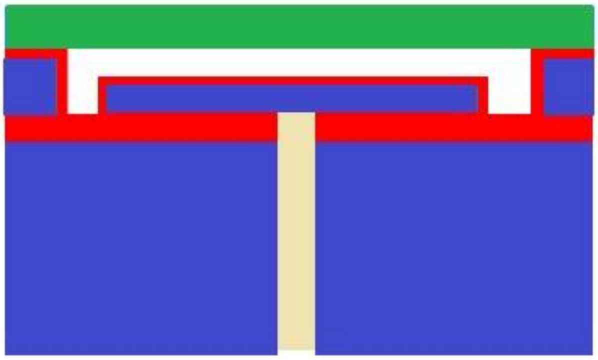

Figure 30: A wafer after Locos process

Compared to surface micromachining process there are several advantages of wafer bonding. The major advantage is that, it is easier and faster to form cavity and the cavity shape is independent of the membrane shape. Therefore, the design parameters of the cavity and membrane can be optimized separately. Also, the sacrificial layer etching is no more a problem (slow etch rate, the aspect ratio of the cavity). Better control over the cavity depth makes possible to fabricate large gaps with high precision. On the other hand, surface roughness can cause problems at the wafer bounding step. Also, the process is costly.

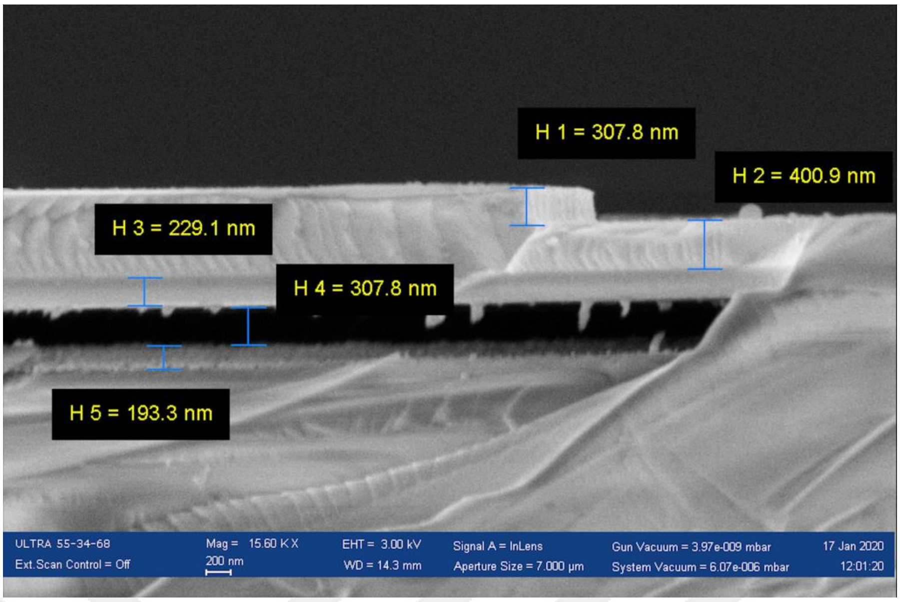

Figure 31: SEM image of a wafer bonded CMUT [175]

Wafer bonding technique can be also used with Insulating substrates to eleminate complicated isolation steps as well as paracitic capacitance [135], [136]. Moreover, using transparent insulating substrate such as glass, quartz and fused silica enables transparency.

CHAPTER II

2. CMUT MODELLING

Due to the growing demand of applications in diagnostic medical imaging, fast evaluation of CMUTs is required. Therefore, both equivalent circuit and finite element models have been developed over the years. In the simplest form, CMUTs can be modeled using Mason's equivalent circuit model [44]. The model is composed of two ports; one port stands for electrical part and the other port stands for mechanical section. The electrical port contains the device capacitance and in the mechanical port; there is mechanical membrane impedance. The impedance of the membrane is defined with inductor and capacitor, which are analogous to mass and spring constant of the membrane. Moreover, spring softening effect is included with a negative capacitance. The circuit is shorted when the medium is vacuum. If a CMUT is operated in immersion medium, the circuit is terminated with the impedance of the medium. However, the model is inaccurate when there is a medium loading. Several equivalent circuit models have been developed for air and immersion. Haller et al. and later Ladabaum et al. developed an equivalent circuit that explains the device behavior in vacuum [9, 10]. Soh et al. proposed an equivalent circuit for immersion medium [19]. Caronti et al. included the effect of air inside the cavity into the equivalent circuit [52]. Goksen et al. developed an equivalent circuit which can describe the device behavior in immersion medium [53]. Most of these models also defined turns ratio for partial metallization. Lohfink et al. proposed an equivalent circuit that describes CMUT behavior by defining a piston that has the same acoustical and electrical behavior as the membrane [39].

Complex radiation impedance was defined by Bozkurt et al. for immersion medium [55]. The nonlinear behavior of the circular membrane was included in an equivalent circuit by Oguz et al [54]. Olcum et al. proposed an equivalent circuit for the collapse mode operation of a CMUT [57]. Mao et al. developed an equivalent circuit model that can simulate axisymmetric modes of the membrane [58] and later, the equivalent circuit was modified for multiple CMUT cells [59]. In addition to equivalent circuit models, there is various research groups have been working on finite element models. Goksen et. al. studied and compared 2D axisymetric and 3D FEM models and experimantally validated [40]. Periodic structure and radiation conditions of the CMUTs were studied in [42]. G. Wojcik et al. İnvestigated propagating waves between CMUT and medium interface [45]. Propagation modes of a membrane were disscussed by S. Ballandras et al. [48]. Bozkurt et al. [137] stuided the effect of electrode area on bandwidth using FEM. Bayram et al. [138] defined a new operation regime in which a CMUT is operated higher than collapse voltage. Moreover, they calculated average membrane displacement for different operation regimes. Time domain analysis was studied by M. Kaltenbacher et al. [50]. Cross talk between membranes were analyzed using 2D FEM [139]. FEM are extensively used as well to understand CMUT behaviour. Effect of electrode area on bandwidth was studied with FEM by Bozkurt et al. Bayram et al studied the size, thickness, type, and position of the metal electrode within the membrane [140]. Moreover, same group showed average membrane displacement for different operation regimes. 3D FEM was developed to calculate output pressure by Goksen et al. In [40], 2D axisymetric and 3D FEM were compared.

The research regarding equivalent circuit and finite element models are disscussed in detail in the following section.

2.1. *Finite Element Modeling*

Finite element models have been used to obtain CMUT parameters and higher order membrane modes, output pressure and frequency bandwidth. Commercially available ANSYS program was used throughout this study. The program provides several types of analyses such as modal, static, harmonic and transient analysis. Modal analysis is used to find out the mode shape of the structures with various shape and size as well as non-uniform ones. When optimizing the operation frequency of a CMUT, modal analysis can be used. Static analysis is used to determine the collapse voltage of a CMUT. Deflection of a membrane at different bias voltages is shown in the Figure 32.

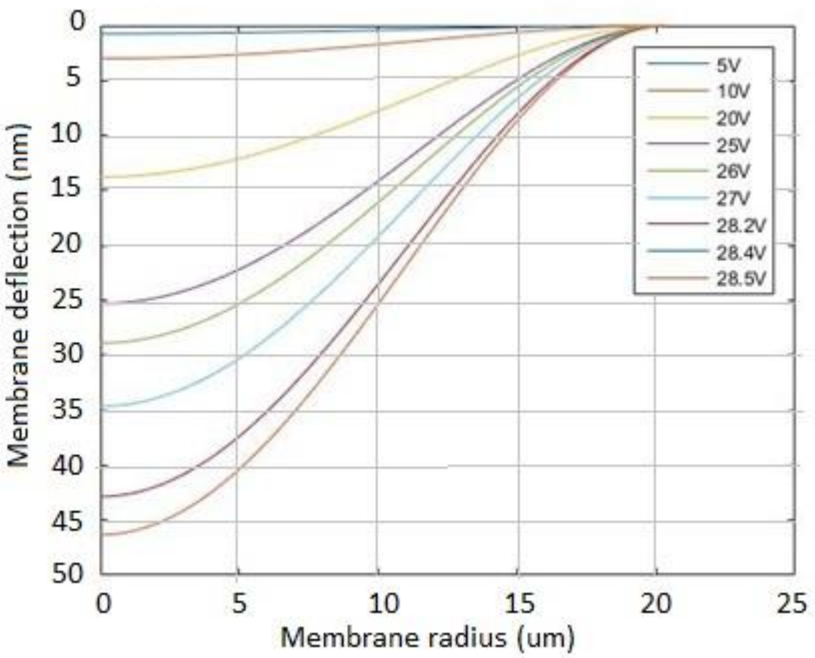

Figure 32: An example of static analysis

Moreover, static analysis is used along with the harmonic response analysis. Harmonic analysis is used to obtain frequency bandwidth and output pressure of the transducer. The analysis requires two part; In the first part, a static solution needs to be obtained and saved for the second subsequent part. In the second part, the reponse of the transducer for a frequency range. For bandwidth calculations a short pulse is applied to the transducer and the created output pressure by the transducer is observed for a frequency range of concerned. Additionally, displacement of the transducer (d) can be observed and using the relation between pressure (p) and displacement which is given with; $p = 2\pi f Z$, where f is frequency and Z is the impedance of the medium, which is 1.5Mraly. On the other hand, harmonic analysis works until a certain cut off frequency, which is given as; $f_c = \frac{1.22 * v_{med}}{2r_{pitch}}$, where vmed is the velocity in the medium and rpitch is the cell radius. At low frequencies below the cut off frequency, the wave fronts moves parallel through the absorbing boundary.

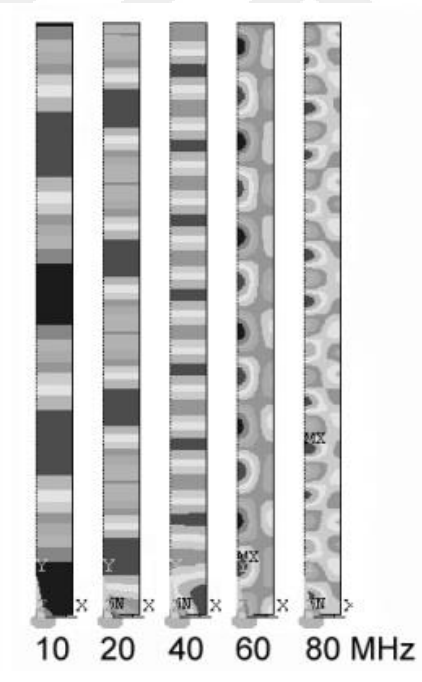

Figure 33: Wave fronts in waveguide [41]

However, at high frequencies, above the cut off frequency, wave fronts propagate with oblique angle (Figure 33) and hence they can't be fully absorb by the absorbing boundary. Therefore, the data become corrupted. (Figure 34). Furthermore, impedance of a transducer is calculated using harmonic analysis (Figure 35).

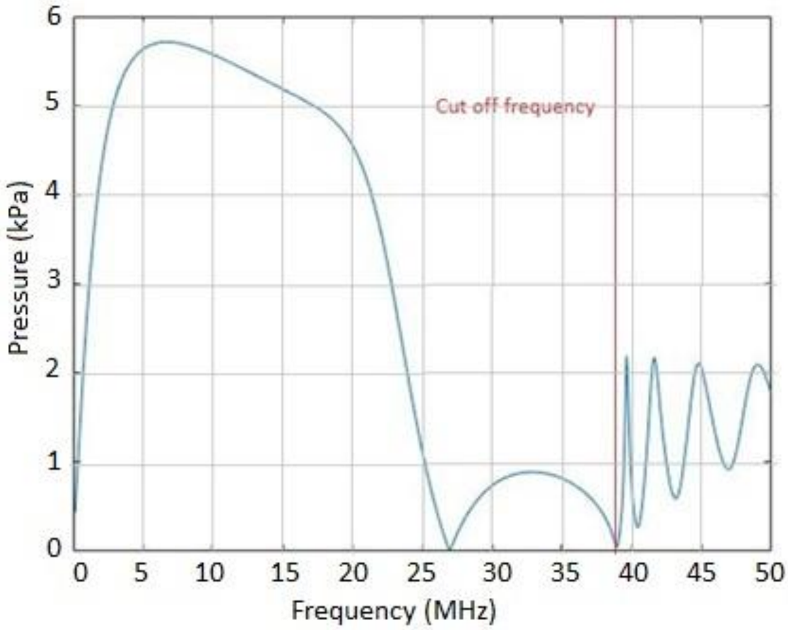

Figure 34: An example of a distorted data after cut off frequency

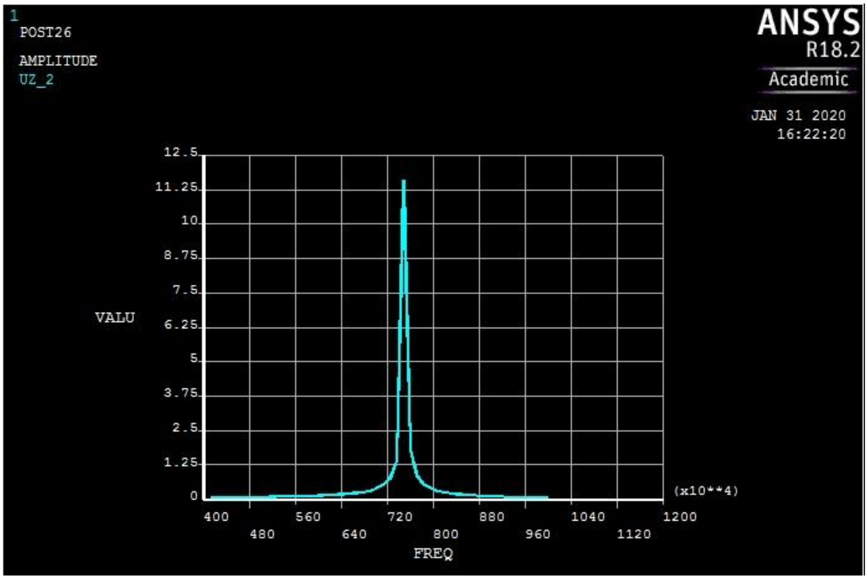

Figure 35: An example of transducer resonance in vacuum.

Therefore, transient analysis is a better option to observe the transducer's response for a broader frequency range as shown in Figure 36. However, transient analysis is much more time consuming than harmonic analysis. In transient analysis, first a bias voltage (80% of the collapse voltage is usually applied) is applied to the transducer until the transducer becomes stable. Then a short duration pulse is applied similar to harmonic analysis. After that, the bias voltage, same as before, is applied until the transducer becomes stable again. The information obtained from transient analysis is in time domain so usually the data is transformed to frequency domain using Fast Fourier Transform (FFT).

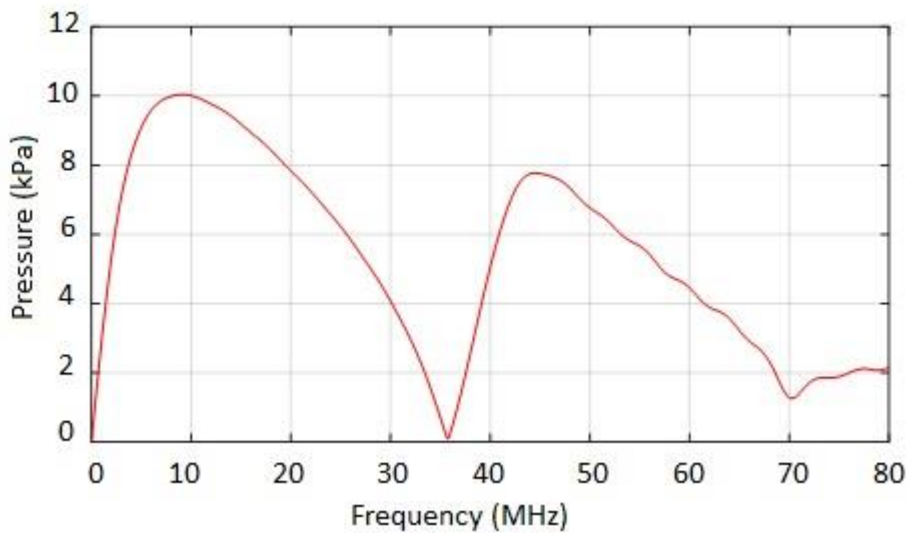

Figure 36: An example of transient analysis result after FFT

All the analysis mentioned above can be constructed by 2D and 3D FEM. There are vast amount of elements provided in the program. CMUT models are usually built with plane elements in 2D analysis and solid elements in 3D analysis. 2D models are constructed as axisymmetric models as shown in Figure 37. The model is axisymmetric around the center, where it is only fixed at x direction. DC bias and AC signal are applied using capacitor like elements (TRANS126), which are attached to the membrane. The fluid-solid region (the red region shown in Figure 37) is defined using appropriate elements. Long rectangular fluid region is constructed as waveguide on top of membrane. Absorbing boundary can be implemented at the end of the fluid column or fluid region can be made long enough so that the reflected waves at the boundary don't affect the calculations.

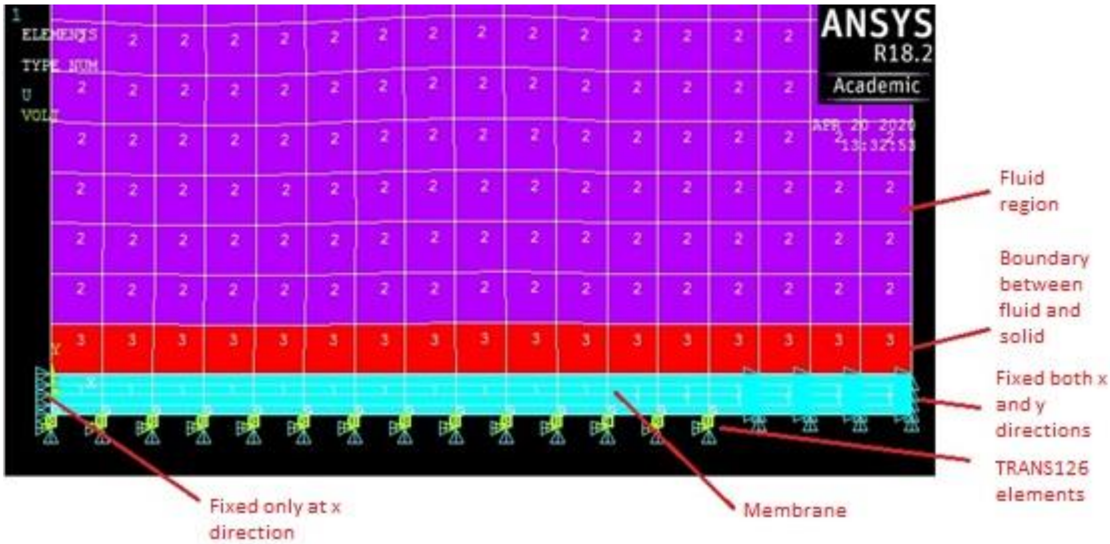

Figure 37: ANSYS 2D axisymmetric CMUT model

Other than constructing fluid region only with rectangular column in 2D, a quarter circles are added on top of rectangular wavguide as shown in Figure 38. The model was designed to eliminate standing waves created by the oblique angle waves at high frequencies. However, the waves still reflects back from the edge, where the rectangular and quarter circle waveguide meets. Therefore, the cut off frequency problem can't be overcome.

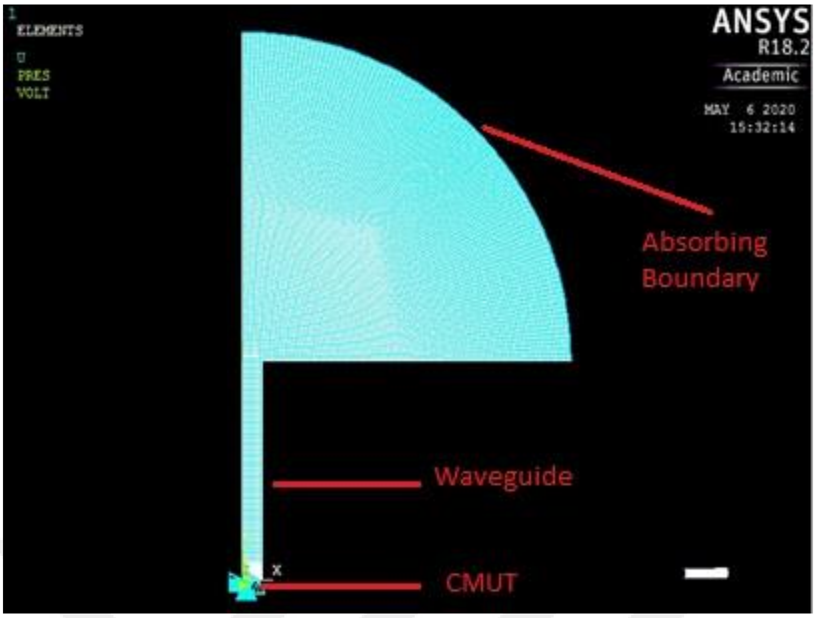

Figure 38: An example of 2D CMUT design

3D models are constructed in similar manner (Figure 39a). 3D models give same output as 2D models [40]. However, if the bottom electrode area is kept much less than the membrane area, the models give different results because unlike 2D models, in 3D models the connection lines can be modeled (Figure 39b). The connection lines go to the pads from which a DC bias is applied. However, the lines cannot be modeled in 2D FEM. The addition of the lines effects plate deflection mechanically and hence results in low bandwidth.

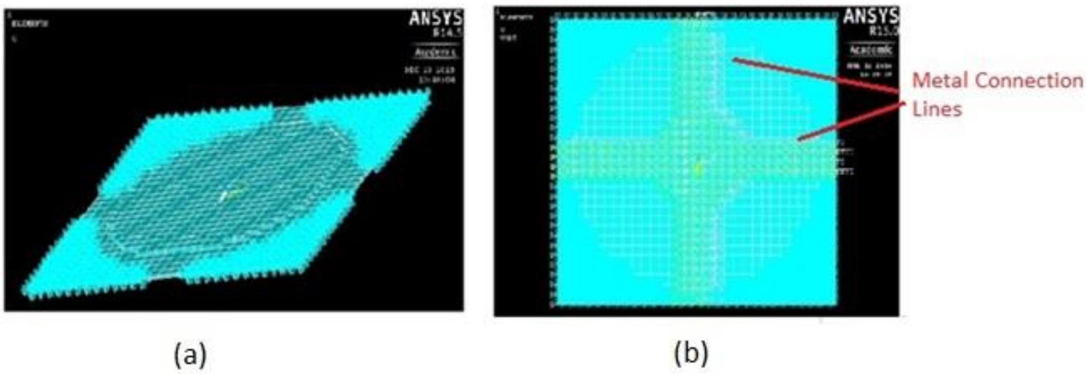

Figure 39: An example of 3D CMUT model, a) top view of a membrane b) bottom view of a membrane

Additionally, 1D piston model can be constructed as shown in Figure 40. In the model, transducer is modeled with a point mass and a spring. Displacement of a membrane can be obained fastly with the model.

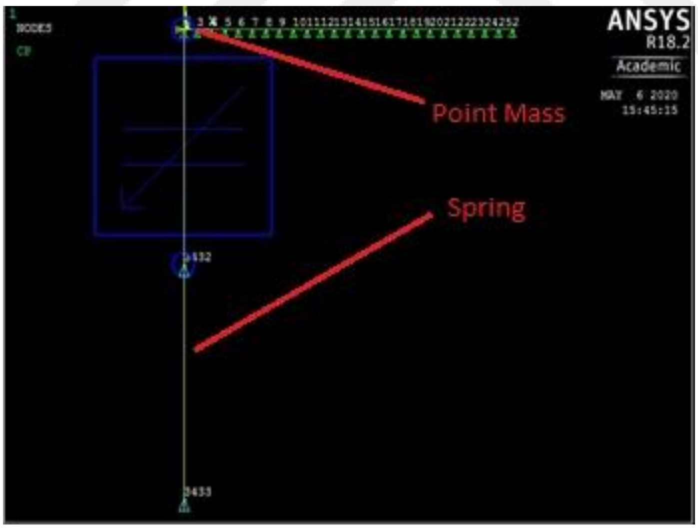

Figure 40: 1D FEM

We also compared the datas obtained from both harmonic and transient analysis including far field and surface pressure differences (Figure 41). The results are matched well and in harmonic analysis aforomentioned cut off frequency is observed whereas transient analysis provide smooth data without cut off frequency limitation. Moreover, the membrane displacement profile for different frequency values were observed for the model given in Figure 41. As it can be seen clearly form Figure 42 that the displacement profile of the transducer changes form the fundamental mode (0,1) to second mode (0,2) as the frequency is increased.

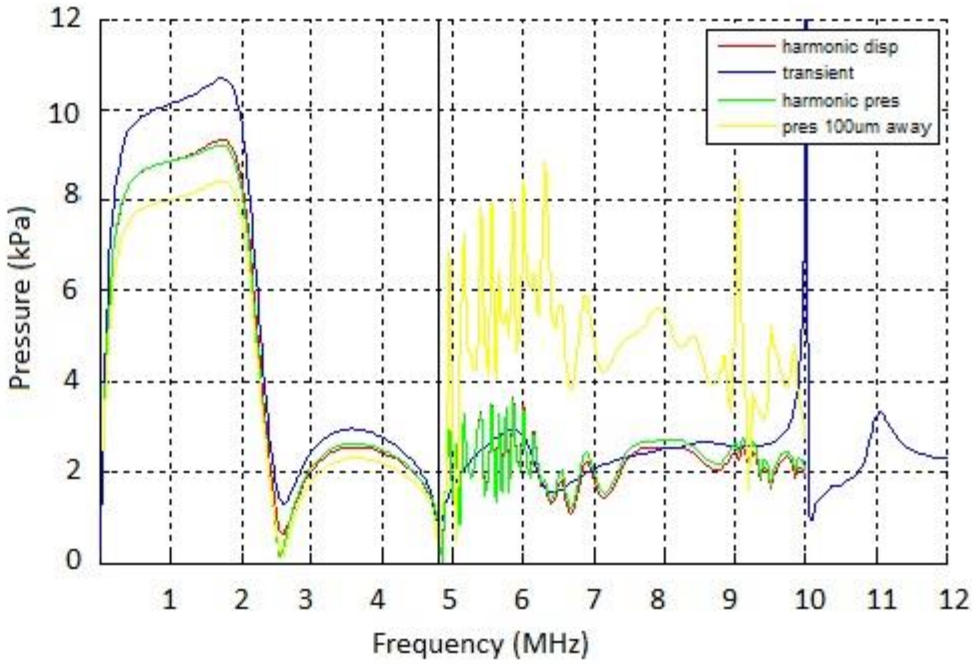

Figure 41: Harmonic vs. Transient analysis

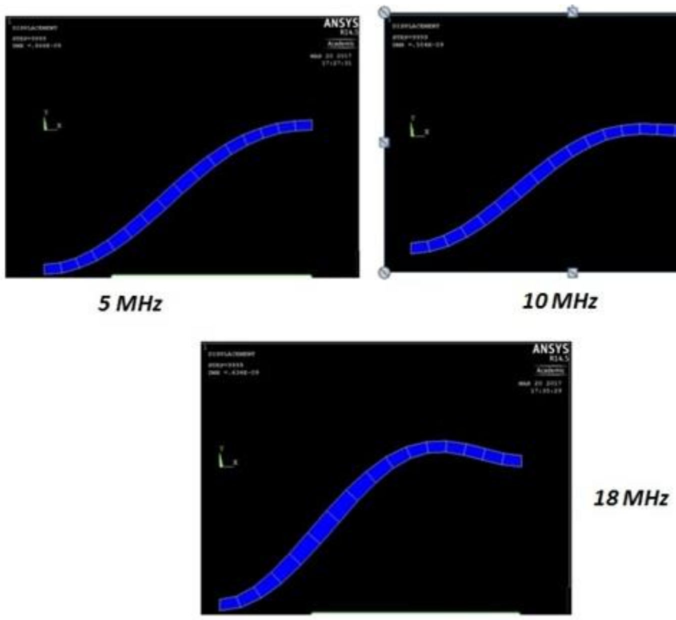

Figure 42: Deflection shape of the membrane at different frequencies

2.2. *Parallel Plate Model*

The dynamics of a CMUT can be derived using a simple parallel plate capacitor model as shown in Figure 40. The model allows one to find out parameters such as the pull-in voltage, center frequency, bandwidth, maximum achievable output pressure, transmission efficiency and receive sensitivity. In the model, only top plate moves like a piston, which means that there is no deflection of the membrane. The bottom electrode is fixed and there is a gap (g_0) between top and bottom electrodes. The plate is simplified as a rigid plate with an equivalent mass (*m)* supported by a spring with an equivalent spring constant (*k)* anchored on a substrate. A damping factor (*b)* is used to represent all mechanical and acoustical damping mechanisms in the CMUT as given in Figure 40. The model neglects the higher order vibrations and also the spring softening effect.

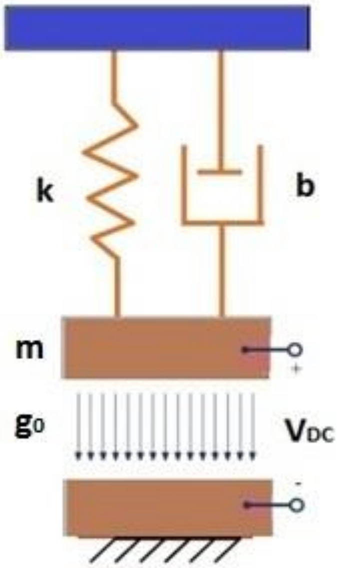

Figure 43: Parallel plate model

CMUTs require a DC bias voltage to operation. When a DC bias is applied between the top and bottom electrode, top electrode is attracted towards the bottom electrode due to electrical force (F_{elec}). This motion is balanced by the mechanical restoring force of the membrane (F_{mec}). If DC bias is increased, the deflection of the top plate increases. However, if DC voltage reaches a certain voltage, which is called collapse voltage, the electrostatic force overwhelms the restoring force and the membrane collapses down on to the bottom electrode.

$$\sum F = F_{elec} + F_{mec} \tag{1}$$

The force is applied on the membrane by electrostatic force;

$$F_{elec} = \frac{\mathcal{E}_0 A V^2}{2(g_0 - g)^2} \tag{2}$$

where $\mathcal{E}_0$ permittivity of free space, A is area, V is applied DC bias voltage, g is membrane displacement and g_0 is initial gap height.

The mechanical force exerted by the membrane is;

$$F_{mec} = kg \tag{3}$$

When the electrostatic force overcomes the mechanical force;

$$\frac{\partial F}{\partial g} = \frac{\mathcal{E}_0 A V^2}{2g^3} - k = 0 \tag{4}$$

And the collapse voltage can be calculated from (4) as;

$$V_{col} = \sqrt{\frac{kg^3}{\mathcal{E}_0 A}} \tag{5}$$

from the equation (4) spring constant is calculated as;

$$k = \frac{\mathcal{E}_0 A V^2}{{g_0}^3} \tag{6}$$

Using (1) and (6), the relation between displacement and vacuum gap can be calculated as;

$$g = g_0 - \frac{\mathcal{E}_0 A V^2}{2kg^2} \tag{7}$$

$$g = \frac{2}{3} g_0 \tag{8}$$

From the (5) and (8)

$$V_{col} = \sqrt{\frac{8kg_0^3}{27\mathcal{E}_0 A}} \tag{9}$$

If the membrane moves beyond the 2/3 of the vacuum gap, the membrane collapses on to the bottom electrode. If the top plate isn't conductive so that there is a metal deposited on top of the plate, the formula above requires a simple modification. In this case;

$$g_{eff} = \frac{t_m}{\mathcal{E}_r} + g \tag{10}$$

where t_m is membrane thickness and $\mathcal{E}_r$ is the dielectric constant of the membrane material.

2.2.1. Center Frequency

The center frequency of the transducer is used to determine operation point. It is different in vacuum and in immersion due to mass loading of the medium. In air, in which the medium damping can be ignored, the center frequency of a mass-spring-damper system is given by the equivalent mass m_{eq} and the equivalent spring constant k_{eq}.

$$\omega = \frac{2.95t_m}{a^2}\sqrt{\frac{E}{\rho(1-\Upsilon^2)}} = \sqrt{\frac{k_{eq}}{m_{eq}}} \tag{11}$$

and in immersion;

$$\omega = \frac{\frac{2.95t_m}{a^2}\sqrt{\frac{E}{\rho(1-\Upsilon^2)}}}{\sqrt{1+0.67\frac{\rho_m a}{\rho t_m}}} = \alpha\sqrt{\frac{k_{eq}}{m_{eq}}} \tag{12}$$

ρ_m and ρ are density of the medium and membrane, respectively. α=*1* in the air and α<*1* in immersion, which means that the center frequency shifts down when there is medium damping. As a numerical example resonance frequency was calculated below in air for a 1umm thick and 20um radius membrane.

$$\omega_{air} = \frac{2.95 \times 1 \times 10^{-6}}{(40 * 10^{-6})^2} \sqrt{\frac{148 \times 10^9}{2338 \times (1 - 0.17^2)}}$$

$$= 14.9\ MHz$$

and

$$\omega_{water} = \frac{14.88 \times 10^6}{\sqrt{1 + 0.67 \times \frac{1000 \times 20 \times 10^{-6}}{2338 \times 1 \times 10^{-6}}}}$$

$$= 5.74\ MHz$$

As it can be seen from the results that without a considerable mass loading, resonance frequency was calculated as 14.9 MHz whereas when mass loading was no longer neglected in water, it was calculated as 5.74 MHz.

and α can is;

$$\alpha = \frac{5.74}{14.9} = 0.385$$

2.2.2. 3dB cut off Frequencies, fractional bandwidth and Quality factor

For a spring-mass-damper system, 3-dB low (w_L) and high (w_H) cut off frequencies are given as;

$$w_L = w_0\left(-\frac{1}{2Q} + \sqrt{\left(\frac{1}{2Q}\right)^2 + 1}\right) \tag{13}$$

and

$$w_H = w_0\left(\frac{1}{2Q} + \sqrt{\left(\frac{1}{2Q}\right)^2 + 1}\right) \tag{14}$$

In (13 and 14), Q is the quality factor of the system and it is defined as store energy over dissipated energy.

$$Q = \frac{\sqrt{k(m + b_i)}}{b_r} \tag{15}$$

An example of a calculation of a quality factor, in water, is given below. The acoustic damping through b_r and is known as the radiation impedance can be calculated as;

$$b_r = j\omega ARe\{Z\}$$

$$= v_{water}\rho_{water}A$$

$$= 1.5 \times 10^6 \times \pi \times (20 \times 10^{-6})^2$$

$$= 1.885 \times 10^{-3}\ \frac{kg}{s^2}$$

And imaginary b_i contributes to mass term and calculated as;

$$b_i = j\omega AIm\{Z\}$$

$$= \rho_{water} \times A \times r \times \frac{8}{3}$$

$$= 6.7 \times 10^{-11} kg$$

And if the spring constant, which is given in (6), is calculated for a DC bias of 28 V, which is just before the membrane collapse, and for a vacuum gap of 150nm;

$$= \frac{8.85 \times 10^{-12} \times \pi \times (20 \times 10^{-6})^2 \times 28^2}{(150 \times 10^{-9})^3}$$

$$= 2583.2\ \frac{kg}{s^2}$$

and effective mass can be calculated from resonance frequency and spring constant;

$$\omega_{water} = \sqrt{\frac{k}{m}} = 5.74\ MHz$$

$$5.74\ MHz = \sqrt{\frac{1291.6}{m}}$$

$$m = 7.84 \times 10^{-11}\ kg$$

Using m, k, br and bi, now quality factor in air can be calculated from (15);

$$Q = \frac{\sqrt{k(m + b_i)}}{b_r} = \frac{\sqrt{2583.2 \times (7.84 \times 10^{-11} + 6.7 \times 10^{-11})}}{1.885 \times 10^{-3}} = 0.325$$

The fractional bandwidth is inversely proportional of quality factor and hence given as;

$$FBW = \frac{w_H - w_L}{w_0} = \frac{1}{Q} = \frac{b_r}{\sqrt{k(m + b_i)}} \tag{16}$$

2.2.3. Transmit Sensitivity

When the electrical input voltage is applied, acoustic pressure is delivered to the medium by the transducer. The transmission efficiency expressed as the ratio of the resultant pressure to the applied voltage. The energy stored by the CMUT is given as;

$$W = \frac{\mathcal{E}AV^2}{2(d+x)} \tag{17}$$

From this equation electrostatic force can be found as;

$$f = \frac{\partial W}{\partial x} = -\frac{\mathcal{E}AV^2}{2(d+x)^2} \tag{18}$$

Here $V^2 = V_{DC}^2 + V_{AC}^2(t) + 2V_{DC}^2 V_{AC}^2(t)$ and for the fundamental frequency only the 3rd parameter contributes to the output pressure and hence the output pressure is equal to;

$$p(t).A = F(t) = -\frac{\mathcal{E}AV_{DC}V_{AC}}{(d+x)^2} = CEV_{AC}(t) \equiv nV_{AC}(t) \tag{19}$$

Therefore, transmit sensitivity is calculated as;

$$S_{TX} = \frac{p(t)}{V_{AC}(t)} = \frac{n}{A}\left(\frac{Pa}{V}\right) \tag{20}$$

2.2.4. Receive Sensitivity

On the contrary to transmit sensitivity; in receive sensitivity, there is an incoming pressure to the CMUT surface and hence, as an output a current is generated.

$$I_{AC} = V_{DC}w_0C_0\frac{\Delta x}{x_0} \tag{21}$$

The fractional displacement, $\frac{\Delta x}{x_0}$, occurs due to incident wave. By using the equations $C_O = \frac{\varepsilon A}{x_0}$ and $= \frac{V_{DC}}{x_0}$;

$$I = CE\frac{\partial x}{\partial t} \tag{22}$$

The Pressure is given as;

$$P = Re\left(Z_m\frac{\partial x}{\partial t}\right) \tag{23}$$

And hence receive sensitivity is calculated as;

$$S_{RX} = \frac{I}{P} = \frac{CE}{Z_m}A = \frac{nA}{Z_m} \tag{24}$$

2.2.5. Summary

In conclusion, for practical applications collapse voltage must be as low as possible. Therefore, gap should be small or plate thickness can be made thinner. However, small gap causes low sensitivity due to low output pressure. Plate radius can be increased to obtain low collapse voltage whereas in this case FBW is decreases since the mass of the membrane increases. Therefore, parameters must be optimized according to application.

2.3. *Equivalent circuit models*

2.3.1. Mason's Model

Mason's equivalent circuit [51] is widely used in the equivalent circuit representation of CMUTs (Figure 44). The circuit is composed of mechanical impedance of a CMUT membrane, Z_m , a medium impedance Z_a, a negative capacitor, $-C_0$, in the mechanical domain and a capacitor in electrical domain and voltage source in the electrical domain. Mason's equivalent circuit is in good agreement when the medium is air.

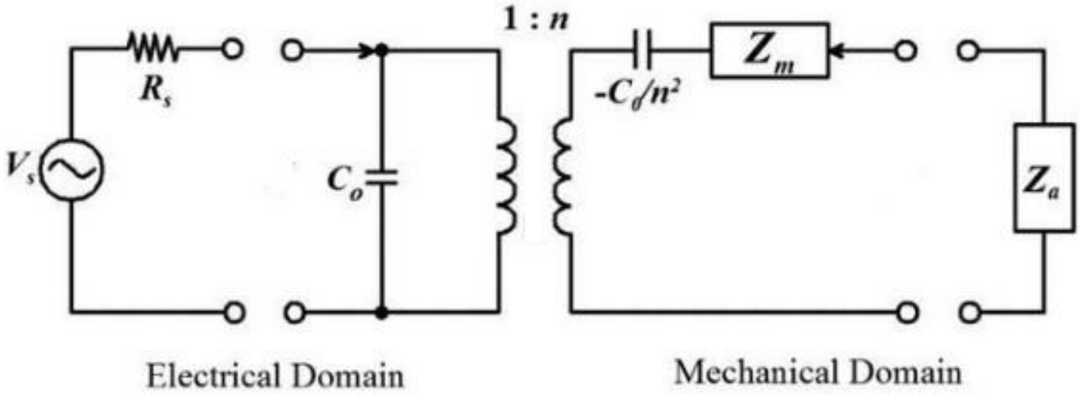

Figure 44: Mason's equivalent circuit model

2.3.1.1. Mason's Model Parameters

2.3.1.1.1. Shunt Capacitance

An approximate value for the variable CMUT capacitance, C(x), can be found with a parallel plate approximation. First, the effective gap between the two conductive electrodes is given as;

$$d_{eff} = t_0 + \frac{t_i + t_m}{\mathcal{E}_r} \tag{25}$$

where t_i is insulator thickness, t_0 is vacuum gap thickness and $\mathcal{E}_r$ is the relative dielectric constant of the membrane material.

$$C_x = \frac{\mathcal{E}_0 A}{d_{eff} - x} = \frac{\mathcal{E}_0 A}{d_{eff}\left(1 - \frac{x}{d_{eff}}\right)} \approx \frac{\mathcal{E}_0 A}{d_{eff}}\left(1 + \frac{x}{d_{eff}}\right) \tag{26}$$

Where $\mathcal{E}_0$ is the relative permittivity of free space and A is the area of the capacitor plates. The time derivative of the CMUT capacitance can be calculated using the derivative of CMUT capacitance with respect to displacement;

$$\frac{d}{dt}C(t) = \frac{d}{dx}C(x)\frac{dx}{dt} = \frac{C_0}{d_{eff}}\frac{dx}{dt} \tag{27}$$

dx/dt is the velocity of the membrane and shunt (static bias) CMUT capacitance is given as;

$$C_0 \approx \frac{A\mathcal{E}_0\mathcal{E}_r}{t_i + \mathcal{E}_r t_0} \tag{28}$$

Shunt (static) capacitance, C_0, is the capacitance that is formed between electrodes of the CMUT. C_0 gives rise to turns ratio. On the other hand, bandwidth decreases with increasing shunt capacitance.

2.3.1.1.2. Transformer and Turns Ratio

Transformer ratio, n, converts parameters in electrical domain to mechanical domain using the analogy between the domains and given as;

$$n = \frac{A\mathcal{E}_0\mathcal{E}_r^2}{(t_i + \mathcal{E}_r t_0)^2} V_{DC} \tag{29}$$

2.3.1.1.3. *Negative Capacitance*

When a DC bias is applied to the electrodes of a CMUT, the membrane moves towards the bottom electrode and hence the membrane experiences more electrostatic force. This phenomenon is called the spring softening effect. To show this effect in the equivalent circuit a negative capacitance,$-\frac{C_0}{n^2}$, is added to the circuit.

2.3.1.1.4. *Lumped medium impedance*

In the mechanical domain, Z_aS, stands for radiation impedance. Radiation impedance of the membrane is analogous to an electrical resistance. It is defined by the average pressure in the medium to the average velocity of the membrane. The radiation impedance value depends on the transducer dimensions. If the transducer dimensions are comparible to the wavelength, acoustic energy is stored in the vicinity of the radiating surface and the radiation impedance become complex quantity. However, when the transducer dimensions are relatively higher than the acoustic wavelength, the radiation impedance becomes mostly real [55]. In this case, the radiation impedance approaches to the acoustic impedance of the medium; $Z_a = \rho v_{med}$.

2.3.1.1.5. *Lumped Mechanical Impedance*

Lumped mechanical impedance, Z_mS, is the response to applied force. It is referred as the ratio of the uniform applied pressure to the average velocity of them membrane, $Z_m = \frac{P}{v}$. Z_m is composed of series LC circuit.

2.3.1.2. Limitations of Mason's Equivalent Circuit Model

Mason's equivalent circuit in Figure 44 is terminated with the fluid medium impedance of water, which is 1.5 $kgm^2s^{-1}x10^6$, and frequency bandwidth vs. pressure graph was obtained, then it was compared with FEM results. As it can be seen from the Figure 45. results don't match with each other. Mason's equivalent circuit model miscalculated the center frequency and predicted the frequency bandwidth much more than it is. Therefore, when the loading medium is not air the equivalent circuit fails.

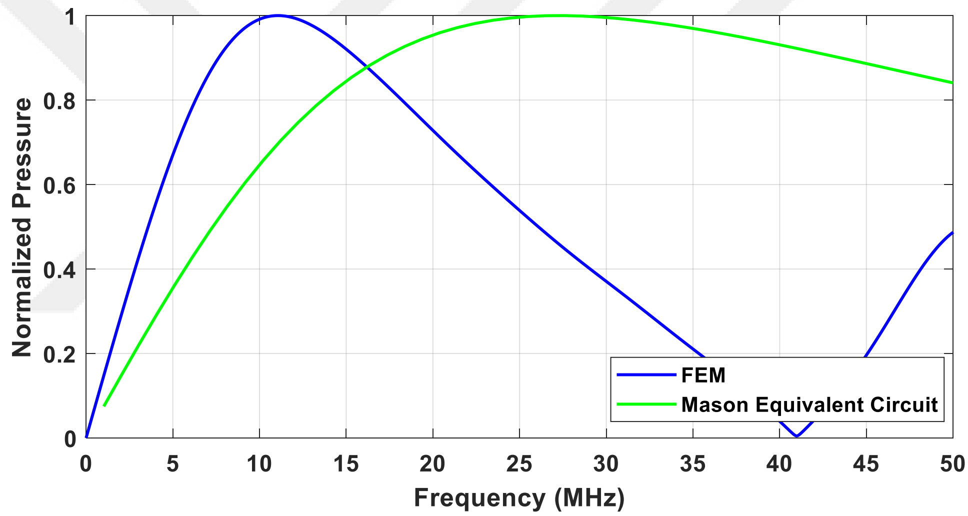

Figure 45: FEM vs Mason's equivalent circuit model

In Mason's equivalent circuit, the turns ratio of the electromechanical transformer, the spring softening capacitance and the shunt input capacitance are calculated by parallel plate and small signal assumptions. In addition, when deriving the LC mechanical impedance, average velocity of the membrane is considered. Therefore, the mass of the membrane is calculated 1.8 times of the actual mass of the membrane and hence spring constant is calculated 1.8 times less than the actual spring constant [143].

2.3.2. 1D Equivalent Circuit Model

1D model refers to the approximation of CMUT membranes' to a piston (Figure 46). In the model, the shape function is assumed to be independent of the displacement.

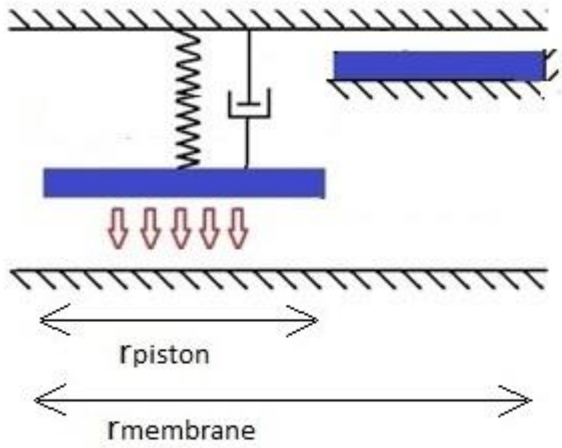

Figure 46: 1D piston assumption

The piston approximation was done assuming the critical displacement of a plate capacitor is 1⁄3 of the gap height, the piston area can be related with the membrane area;

$$A_{piston} \times \frac{1}{3} g = A_{pitch} \times w_{mean} \tag{30}$$

where the average dispalcemenent of the membrane which is given as;

$$w_{mean} = \frac{1}{A} \int_{0}^{r_{pitch}} w(r)\ 2\pi r\ dr \tag{31}$$

Kmem can be calculated with an applied force as;

$$p = \frac{k_{mem} w_{mean}}{A_{pitch}} \tag{32}$$

and kps can be calculated from the assumption of the same fluid volume for the same static fluid pressure;

$$\frac{k_{mem}w_{mean}}{A_{pitch}} = \frac{k_{ps}w}{A_{ps}} \tag{33}$$

Then, electrically active area, A_{el}, can be calculated from rearranging eq. (8);

$$A_{el} = \frac{8k_{ps}g_0^3}{27\mathcal{E}_0 V_{crit}^2} \tag{34}$$

The piston mass, m_{ps}, is calculated from the resonance frequency of the membrane as;

$$m_{ps} = \frac{k_{ps}}{(2\pi f_0)^2} \tag{35}$$

Piston damping, bps, can be calculated from the quality factor,Q;

$$Q = 2\pi f_0 \frac{m_{ps}}{b_{ps}} \tag{36}$$

The mechanical fluid impedance, Z_m, is given as;

$$Z_m = \frac{F}{v} = jwm_{fl} + b_{fl} \tag{37}$$

where mfl is fluid mass and bfl is the fluid damping.

$$b_{fl} = \mathrm{R}\left\{\frac{F}{v}\right\} = \mathrm{R}\left\{\frac{p}{v}\right\}\frac{A_{ps}^2}{A_{pitch}} = Z_{fl}\frac{A_{ps}^2}{A_{pitch}} \tag{38}$$

$$m_{fl} = \rho_{fl}A_{ps}h_{mfl} \tag{39}$$

hmfl is the fluid height and it is calculated as;

$$h_{mfl} = \frac{8r_{ps}}{3\pi}(1 - \frac{r_{ps}}{r_{pitch}})^{1.4} \tag{40}$$

The spring softening is calculated from;

$$k_{el} = -C_0\left(\frac{V_{dc}}{g_0 - w_{dc}}\right)^2 \tag{41}$$

The transformer ratio is given as;

$$N_u = C_0\frac{V_{dc}}{g_0 - w_{dc}} \tag{42}$$

2.3.2.1. Limitations of 1D Model

The model was constructed using the formulas above for a pitch radius 23um, a membrane radius 20um, an electrode radius 20um and a thickness of 1.4um. The result was compared with FEM. As it can be seen from the Figure 47 that 1D model [39] can only model the first mode frequency bandwidth. The reason is that the assumptions that was made to construct the 1D model. First of all, in reality, the membrane have a deflection profile which means that the center of the membrane deflect more than the anchored regions due to electrostatic force. When a piston like deflection is assumed, nonlinear deflection of the membrane is ignored and hence the only mode shape simulated is the first mode as given in Figure 47. Moreover, the radiation impedance was calculated assuming it is real. This is correct when the wavelength of the transducer is much smaller than the wavelenght. However, at high frequencies, transducer size and wavelength become comparible and hence radiation impedance will be complex.

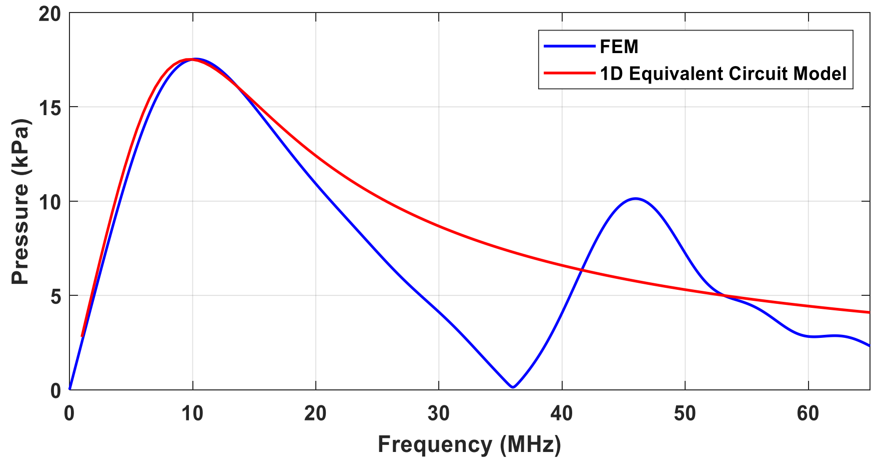

Figure 47: FEM vs 1D equivalent circuit model

2.3.3. An Equivalent Circuit Model with Modal Analysis

The previous equivalent circuit models mostly use the mechanical impedance of the membrane around the first resonance frequency and hence aim to provide frequency bandwidth for the first mode only. However, It is important to observe frequency responce for broader range in order to provide frequency bandwidth accurately. Recently, it was shown that model analysis can be used to find higher order modes of the membrane [58]. On the other hand, in the model anti resonances were not predicted accurately.

In modal analysis, the equation of motion of a membrane was solved for the transverse deflection of a prismatic beam with a function of the longitudinal coordinate x and the time t can be expressed as [143];

$$L[w(x,t)] + c\frac{\partial w(x,t)}{\partial t} + \rho bh\frac{\partial^2 w(x,t)}{\partial t^2} = q(x,t) \tag{43}$$

Where ρ denotes the specific mass of the beam material, b and h are the width and thickness of the beam, respectively. c is the viscous drag parameter. q(x,t) denotes a transverse force per unit length. L denotes a fourth order linear differential operator.

Applying modal analysis technique solution to (43) is given with;

$$w(x,t) = \sum_{n=1}^{\infty} \phi_n(x)\xi_n(t) \tag{44}$$

normalized mode shapes, $\phi_n(x)$, and generalized coordinates, $\xi_n(t)$. If the series expansion is applied to (43) and multiplying each term by a normal mode $\phi_m(x)$, integrating along the beam length and using orthogonality of the mode shapes;

$$M_n \frac{\partial^2 \xi_n}{\partial t^2} + r_n \frac{\partial \xi_n}{\partial t} + K_n \xi_n = P_n(t) = P_n e^{jwt} \tag{45}$$

For n=1,2,…

where;

$$M_n = \int_0^l \rho bh\, \phi_n^2(x) dx = \rho bhl = m \tag{46}$$

$$K_n = \int_0^l \phi_n(x) L[\phi_n(x)]\, dx = w_n^2 M_n \tag{47}$$

$$r_n = \int_0^l c\, \phi_n^2(x) dx = cl \tag{48}$$

$$P_n = \int_0^l q(x)\, \phi_n(x) dx \tag{49}$$

(46) is the generalized mass, (47) is the generalized stiffness, (48) is the generalized mechanical resistance and (49) is the generalized load corresponding to mode n, respectively [143]. The lumped parameters of the equivalent circuit model were calculated according to the each eigenmode, $\phi_n(x)$, which were formed using the modal information of the membrane at each axisymmetric mode. Therefore, total response of a CMUT membrane is obtained from the individual response of all axisymmetric modes.

For small signal where, Vac << Vdc, the applied electrostatic force to the membrane for ith mode is given as;

$$F_{ei} = \iint f_e(\mathrm{p},t)\phi_i(\mathrm{p})dA \cong \iint \frac{\mathcal{E}_0 V_{dc}\phi_i(\mathrm{p})}{\left(d_0 - w_0(\mathrm{p})\right)^2} V_{ac} dA + \iint \frac{\mathcal{E}_0 V_{dc}{\phi_i}^2(\mathrm{p})}{\left(d_0 - w_0(\mathrm{p})\right)^3} w(\mathrm{p},t) dA \quad (50)$$

For a variable electrostatic force $f_e(\mathrm{p},t)$, a linear relation between alternating voltage Vac and electrostatic force Fei is shown in equation (50).

And the transformer ratio is defined as;

$$r_i = \iint \frac{\mathcal{E}_0 V_{dc}\phi_i(\mathrm{p})}{\left(d_0 - w_0(\mathrm{p})\right)^2} dA \cong \chi_i \pi r^2 \frac{\mathcal{E}_0 V_{dc}}{d_{eff}^2} \quad (51)$$

In equation (50) the second term represents spring softening effect as a result of DC bias

$$K_i' = \frac{\mathcal{E}_0 V_{dc}{\phi_i}^2(\mathrm{p})}{\left(d_0 - w_0(\mathrm{p})\right)^3} dA = \Psi_i \pi r^2 \frac{\mathcal{E}_0 {V_{dc}}^2}{d_{eff}^3} \quad (52)$$

Moreover, in [58] the modal mass, spring constant and loss is given as;

$$M_i = \iint \rho h \phi_i^2(\rho) dA = \Psi_i \breve{\rho} \breve{h} \tag{53}$$

$$K_i = (2\pi f_i)^2 M_i = \Psi_i \gamma^4 \breve{D} \tag{54}$$

$$R_i = \frac{2\pi M_i}{Q_i} = \Psi_i \gamma^2 \frac{\sqrt{\breve{\rho}\breve{h}\breve{D}}}{Q_i} \tag{55}$$

If there are more than one membrane layer with different materials, equivalent values of the thickness, density and fluxural rigidity must be calculated. In the equations (53), (54) and (55); $\bar{h}$, $\breve{\rho}$ and $\breve{D}$ are the equivalent thickness, density and flexural rigidit, respectively. Moreover, the values of $\mathfrak{x}_i$, γ and Ψ_i are provided for the first three axisymmetric mode in Table 3 and Q_i in equation (55) is quality factor in the absence of loading.

Table 3: Modal information for the first three axisymetric modes

	Mode (0,1)	Mode (0,2)	Mode (0,3)
$\gamma_i r$	3.1962	6.3064	9.4295
$\mathfrak{x}_i = \frac{\iint \phi_i dA}{A}$	0.3116	-0.1313	0.0736
$\Psi_i = \frac{\iint \phi_i^2 dA}{A}$	0.1828	0.1018	0.0675

CHAPTER III

3. NEW EQUIVALENT CIRCUIT MODEL

The last equivalent circuit described in the previous chapter can find the resonance frequencies accurately in a medium. However, this model is still inadequate to predict anti-resonance of the plate. The anti-resonance determines the bandwidth of the transducer. The existing models based on only resonances estimates much larger bandwidth for the transducer. Therefore, it is important to include the effect of the anti-resonance for more accurate estimation of the transducer's bandwidth. We studied a simple equivalent circuit model which can predict anti-resonance frequencies, fundamental mode of the membrane, as well as with the higher order modes accurately.

Our proposed equivalent circuit makes use of the mode shapes of a membrane. Therefore, first we will look into the mode shapes of circular membranes. The deflection profiles of the membrane can be calculated analytically [39, 40]. The first two axisymmetric modes, which are (0, 1) and (0, 2), are shown in Figure 48. It should be noted that any circular membrane would possess the same mode shapes at the corresponding modes.

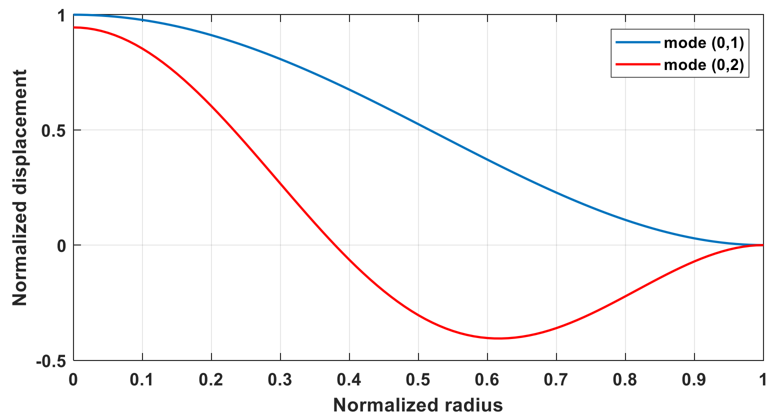

Figure 48: 1st and 4th mode shape of the membrane

It is clear from the Figure 48 that in the mode (0, 1), the maximum deflection occurs at the center region while the anchor side of the membrane moves negligibly. Therefore, the membrane motion can be modeled by a piston transducer whose volumetric displacement is equivalent to the volumetric displacement of the membrane. This modeling works very well around the first resonance [39, 40]. The models find an equivalent spring-mass model for the membrane impedance around the first resonant frequency of the membrane.

However, in mode (0, 2), the center and the anchor side of the membrane move towards opposite directions and hence, deflection of the anchor side of the membrane cannot be neglected. In this case, one can assume that the membrane composed of two moving rigid pistons at second axisymmetric; the first one at the center is a circular piston and the other one is a ring shaped piston, which is the area around the center piston. These two pistons are assumed to move simultaneously in opposite directions and hence CMUT is modeled by two parallel plate capacitors in one dimension as shown in Figure 49a and 49b.

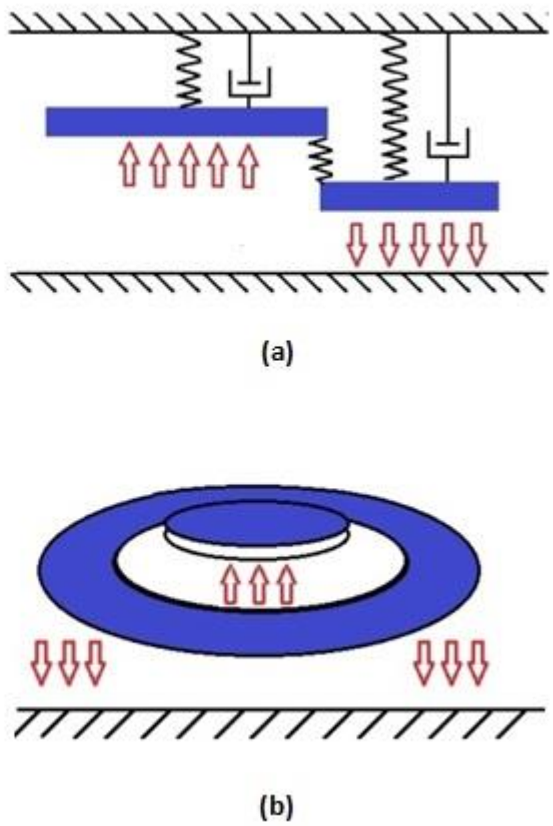

Figure 49: a) The two parallel plate pistons showing the pistons in 2D, b) The center and ring pistons in 3D

The center piston stands for the first mode of the membrane and the ring piston stands for the second axisymmetric mode of the membrane. The mechanics of the two moving plates were approximated by a spring- mass-damper system. The mechanical parameters of the pistons were calculated using well known parallel plate capacitor model with mass constants m_{cent} and m_{ring}, spring constants k_{cent} and k_{ring} for the piston at the center and for the ring shape pistons, respectively. The damping constants of the pistons were assumed to be very small compared to the medium damping constant and hence were ignored. The damping constants of the medium for the center piston and the ring shaped pistons are b_{cent} and b_{ring}, respectively. The equivalent circuit model was designed accordingly to the mechanical model. In the equivalent circuit model, which is shown in Figure 50, there are two branches. The mechanical parameters of each piston define a RLC branch in the mechanical port of the equivalent circuit model. The first RLC branch at the top of the model is composed of the mechanical impedance of the center piston, mass and damping of the medium on top of the center piston while the other RLC branch is composed of mechanical impedance of the ring shape piston, mass and damping of the medium on top of the ring shape piston. The masses of the center and ring pistons and corresponding medium loadings, the spring constants and damping constants of the medium are denoted with L_2 and L_3, $L_{flu_c}$and L_{flu_m}, C_2 and C_3 for the center piston and ring pistons, respectively. Additionally, the spring softening effect is denoted with C_{soft}. The model assumes piston-like motion neglecting deflection profile of a membrane which means that two pistons are free to move in the x direction radiating into circular medium. Also, in order to apply the same electrostatic force on the membranes, the electrode area is set equal to the membrane area.

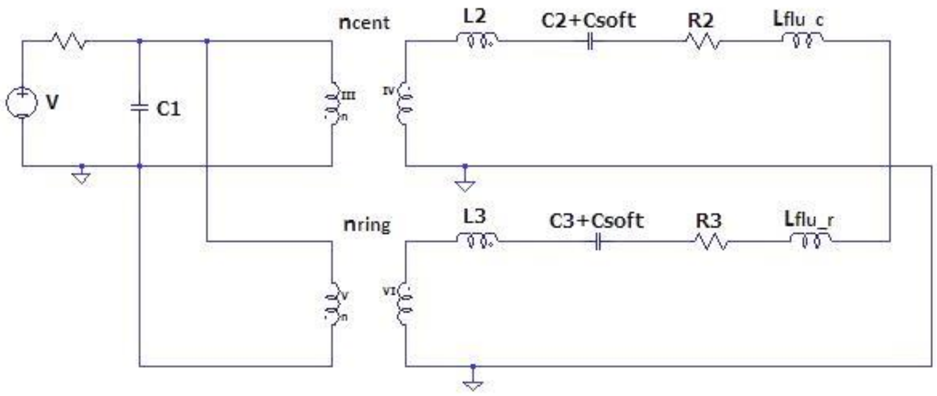

Figure 50: The proposed equivalent circuit model

3.1. Derivation of the Model Parameters

The first step is to find the center piston radius. To start, the deflection profile of the whole membrane was calculated. When an axial force is applied to a thin circular membrane, the deflection is calculated using the finite series formulas in which the membrane is segmented into nodes and the deflection of the each node is found as given in (56) and (57) [144].

$$w_i = \sum_{i=i}^{N} \frac{F_i}{8\pi D} [\frac{(a^2-r^2)(a^2+b_i^2)}{2a^2} + (b_i^2 + r^2) ln\frac{r}{a}] \qquad r > b_i \qquad (56)$$

$$w_i = \sum_{i=i}^{N} \frac{F_i}{8\pi D} [\frac{(a^2+r^2)(a^2-b_i^2)}{2a^2} + (b_i^2 + r^2) ln\frac{b_i}{a}] \qquad \mathrm{r} \leq b_i \qquad (57)$$

D is the membrane flexural rigidity and given as;

$$D = \frac{Et_m^3}{12(1 - \Upsilon^2)} \qquad (58)$$

E is the Young’s Modulus of the membrane, tm is the membrane thickness, ϒ is Poisson’s ratio, a is the membrane radius, r and b are the axial distance from the membrane center to the corresponding node and for the Force to the membrane center, respectively.

Then the mean displacement was calculated with the equation (31);

$$w_{mean} = \frac{1}{A}\int_0^{r_{pitch}} w(r)\, 2\pi r\, dr$$

where A is the area of the membrane. After that, the center piston radius (r_{cent}) was obtained relating the mean displacement of the whole membrane and the piston displacement at a bias voltage as described in [39]. The critical displacement of a parallel plate piston is 1/3 of the vacuum gap. The assumption is that the center piston displaces same volume as the whole membrane at any bias voltage and hence it leads to the equation (30) [39];

$$A_{piston} \times \frac{1}{3} g = A_{pitch} \times w_{mean}$$

Where A_{piston} and $A_{pitch}$are piston and cell areas, respectively. The mass of the center piston was obtained using the dimensions and the material properties of the membrane;

$$m_{cent} = \pi r_{cent}^2 t_m \rho_{silicon} \tag{59}$$

and the mass of the ring piston was calculated subtracting the piston mass from the total mass of the membrane;

$$m_{ring} = \pi r_{memb}^2 t_m \rho_{silicon} - m_{cent} \tag{60}$$

where $\rho_{silicon}$ is the density of the membrane. Spring constant of the center piston was calculated using the parallel plate capacitor model. In the parallel plate model, the relation between electrical force and spring constant is given with;

$$F_{elec} = k_{cent} x_{DC} \tag{61}$$

Here electrical force is given by;

$$F_{elec} = \frac{V^2 \mathcal{E}_0 \mathcal{E}_r \Pi r_{cent}{}^2}{2(g - x_{DC})^2} \tag{62}$$

and hence, the spring constant of the membrane was found as;

$$k_{cent} = \frac{V^2 \mathcal{E}_0 \mathcal{E}_r \Pi {r_{cent}}^2}{2x_{DC}(g - x_{DC})^2} \tag{63}$$

where V is bias voltage, x_{DC} is the membrane deflection under DC bias, $\mathcal{E}_0$ and $\mathcal{E}_r$ are relative permittivity of free space and silicon, respectively.

The spring softening effect is given with;

$$k_{soft} = -\frac{V^2 \mathcal{E}_0 \mathcal{E}_r \Pi a^2}{(g - x_{DC})^3} \tag{64}$$

When electrostatic force is applied to the CMUT membrane the anchor side of the membrane displace much less than the center of the membrane. The spring constant of the ring plate can be obtained from assuming the center piston and the membrane displace the same fluid volume for the same static fluid pressure [39] and hence spring constant of the ring piston was calculated with equation (33);

$$k_{ring} = \frac{k_{cent} \pi r_{pitch}^2}{\pi r_{cent}^2}$$

The imaginary part of the mechanical fluid impedances was added as an additional mass term which was calculated for the center piston as;

$$L_{flu\_c} = \pi {r_{cent}}^2 \rho_{fl} h_{fl} \tag{65}$$

And for ring piston as;

$$L_{flu\_r} = \pi(a^2 - {r_{cent}}^2)\rho_{fl} h_{fl} \tag{66}$$

Fluid height on the pistons and fluid damping were found with equation (40) as described in [39];

$$h_{flu} = \frac{8r_{cent}}{3\pi}(1 - \frac{r_{cent}}{r_{pitch}})^{1.4}$$

Real part of the fluid damping for the center piston is calculated with equation (38);

$$R_2 = \frac{v_{fl}\rho_{fl}(\pi {r_{cent}}^2)^2}{\pi {r_{pitch}}^2}$$

and for the ring piston;

$$R_3 = \frac{v_{fl}\rho_{fl}}{\pi {r_m}^2}(\pi(a^2 - {r_{cent}}^2))^2 \tag{67}$$

where $v_{fl}\ and\ \rho_{fl}$ are velocity of the wave in the medium and density of the fluid medium, respectively.

For a parallel plate capacitor transformer ratio is defined as;

$$n = E_0 C_0 \tag{68}$$

In the equivalent circuit n_{cent} and n_{ring} were calculated according to center piston radius and membrane radius, respectively.

where E_0 is electrical field;

$$E_0 = \frac{V}{(g - x_{DC})} \tag{69}$$

and C_0 is clamped capacitance;

$$C_0 = \frac{\mathcal{E}_0 \Pi a^2}{(g - x_{DC})} \tag{70}$$

Table 4: All the parameters in the new equivalent circuit

Circuit Parameters	Equations	Equation number
Transverse deflection	$w(x,t) = \sum_{n=1}^{\infty} \Phi_n(x)\xi_n(t)$	(44)
Mean displacement	$Wmean = \frac{1}{A}\int_0^{r_{pitch}} w(r)\, 2\Pi r\, dr$	(31)
Piston Area	$A_{piston} \times \frac{1}{3} g = A_{pitch} \times w_{mean}$	(30)
Piston Mass	$\pi r_{cent}^2 t_m \rho_{silicon}$	(59)
Ring Mass	$\pi r_{memb}^2 t_m \rho_{silicon} - m_{cent}$	(60)
Electrical force and spring constant	$F_{elec} = k_{cent} x_{DC}$	(61)

Electrical force	$F_{elec} = \frac{V^2 \mathcal{E}_0 \mathcal{E}_r \Pi r_{cent}{}^2}{2(g - x_{DC})^2}$	(62)
Center piston spring constant	$\frac{V^2 \mathcal{E}_0 \mathcal{E}_r \Pi r_{cent}{}^2}{2x_{DC}(g - x_{DC})^2}$	(63)
Spring softening effect	$-\frac{V^2 \mathcal{E}_0 \mathcal{E}_r \Pi a^2}{(g - x_{DC})^3}$	(64)
Ring piston spring constant	$\frac{k_{cent} \pi r_{pitch}^2}{\pi r_{cent}^2}$	(33)
Fluid mass on center piston	$L_{flu\_c} = \Pi r_{cent}{}^2 \rho_{fl} h_{fl}$	(65)
Fluid mass on ring piston	$L_{flu\_r} = \Pi(a^2 - r_{cent}{}^2)\rho_{fl} h_{fl}$	(66)
Fluid Height	$\frac{8r_{cent}}{3\pi}(1 - \frac{r_{cent}}{r_{pitch}})^{1.4}$	(40)
Fluid damping on center piston	$R_2 = \frac{v_{fl}\rho_{fl}(\Pi r_{cent}{}^2)^2}{\Pi r_{pitch}{}^2}$	(38)
Fluid damping on ring piston	$R_3 = \frac{v_{fl}\rho_{fl}}{\Pi r_m{}^2}(\Pi(a^2 - r_{cent}{}^2))^2$	(67)
Turns Ratio	$n = E_0 C_0$	(68)
Electrical field	$E_0 = \frac{V}{(g - x_{DC})}$	(69)
Capacitance	$C_0 = \frac{\mathcal{E}_0 \Pi a^2}{(g - x_{DC})}$	(70)

3.2. Model Verification

3.2.1. Finite Element Model vs. The Equivalent Circuit Model

The FEM used in this study were constructed using commercially available FEM package (ANSYS 14.5, ANSYS Inc., Canonsburg, PA). A single cell circular membrane was modeled. The membrane was composed of silicon. The membrane was modeled using axisymmetric plane elements (PLANE42). Symmetry boundary conditions were applied to cover the transducer area by periodic replication for mimicking a large CMUT element. The electrostatic force was applied between top and bottom electrodes by electromechanical transducer elements (TRANS126). The top nodes of these elements were attached to the membrane and the bottom nodes were clamped. The electrostatic gap was divided in to small segments and the elements (TRANS126) attached to these small segments which were used to apply the electrostatic pressure and hence the plate was deflected. The membrane profile is given in Figure 51.

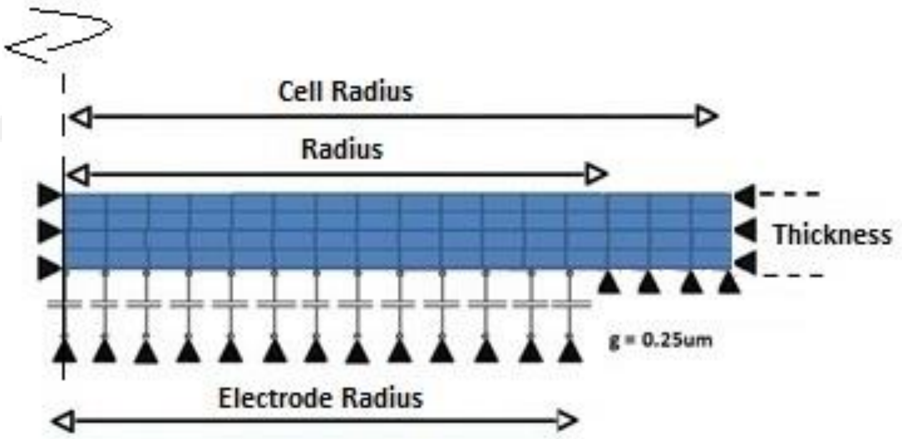

Figure 51: Axisymmetric membrane

The immersion medium into which the transducer radiates was approximated as a rectangular waveguide with rigid walls at the symmetry areas and it was modeled using FLUID29 elements as shown in Figure 52. The fluid solid interface was also modeled with FLUID29 element changing KEYOPT option to ‘0’.The medium was kept long enough so that the reflected waves did not reflected back to disturb the calculations.

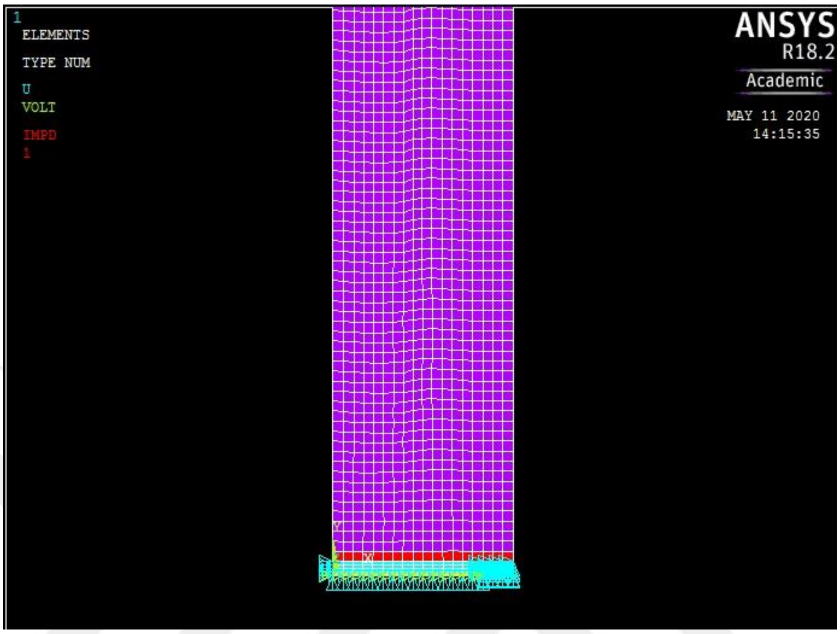

Figure 52: The fluid column on top of the axisymetric membrane

Transient analysis was used to find the transducer bandwidth throughout in this study. The collapse voltage of the membrane was found with static analysis by iterating the bias voltage until the solution did not converge. In subsequent analyses, the DC bias applied (Figure 53a) to the TRANS126 elements is set to 80% of the collapse voltage, which maximizes the transmit/receive sensitivity of a CMUT [145].

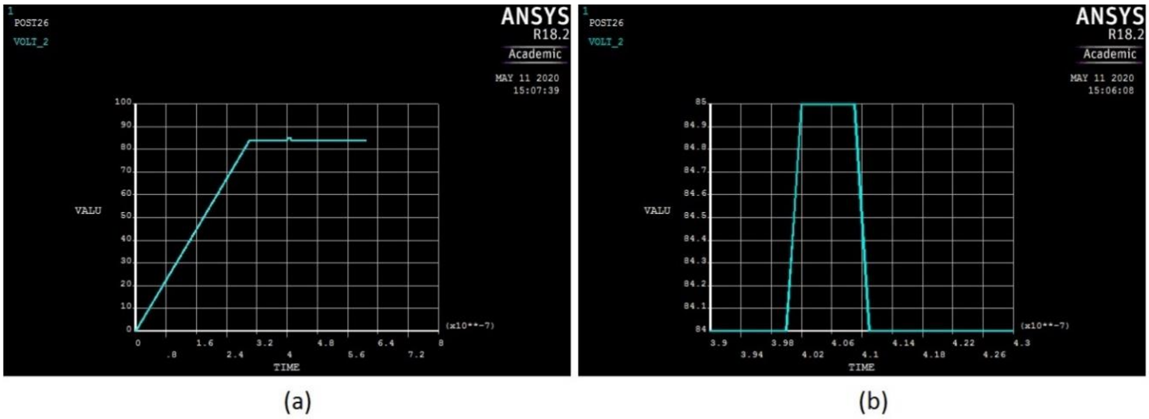

Figure 53: a) The applied DC bias and AC signal to the transducer, b) Zoomed version of 53(a). The applied 10nsec 1V AC signal to the membrane

The transient analysis was first run for a time duration long enough for the membrane to mechanically stabilize under the applied DC bias voltage. Then, a pulse of 10 ns duration and 1 V amplitude was superimposed on the DC bias voltage (Figure 53b). The displacement of the membrane was found in time domain as shown in Figure 54.

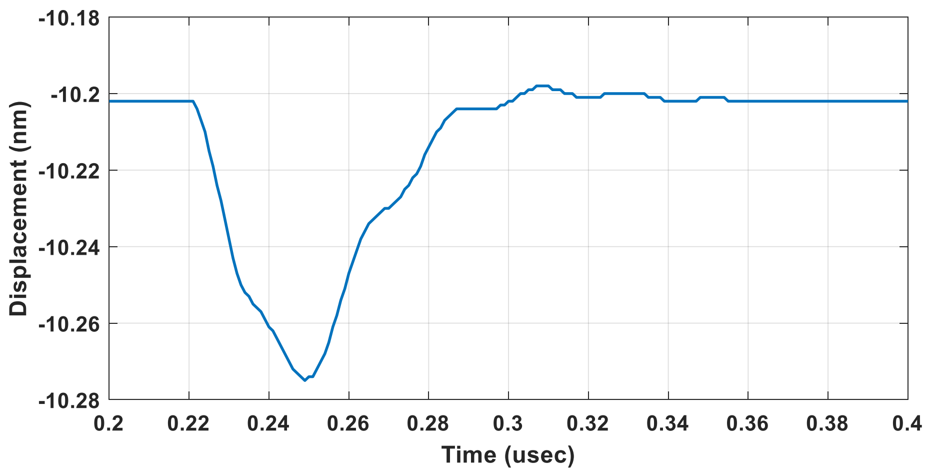

Figure 54: Displacement of the membrane after superimposing 10nsec 1V AC signal on DC bias

The velocity of the membrane was calculated taking the derivative of the displacement data. Then, the velocity data converted to frequency domain by Fast Fourier Transform (FFT). Velocity data was sampled with a predefined number (for example NFFT=2^{16}) and using Matlab function 'fft' the data converted to frequency domain. The height of the vacuum gap (g) was 250 nm. The plate was composed of silicon. Young's modulus, density and Poisson's ratio used for silicon were 169×10^9 Pa, 2328 kg/m^3 and 0.17, respectively.

The equivalent circuit model is evaluated at the designs shown in Table 5.

Table 5: Plate Designs

	Cell radius (µm)	**Membrane radius (µm)**	**Thickness (µm)**	**Electrode radius (µm)**
Design 1	13	10	0.5	10
Design 2	20	17	1.2	17
Design 3	33	30	2.2	30

The solutions and simulations for the equivalent circuit model were done with MATLAB® (The MathWorks Inc., Natick, MA.). The equivalent circuit model provides a good match with FEM for the fundamental, anti-resonance and second axisymmetric mode of the membrane as shown in Figure 52. According to the results, not only the fundamental mode peak but also, the second axisymmetric mode (0, 2) peak and anti-resonance response can be simulated for various membrane geometries. The equivalent circuit model was also capable of finding the device behavior at frequencies beyond the second axisymmetric.

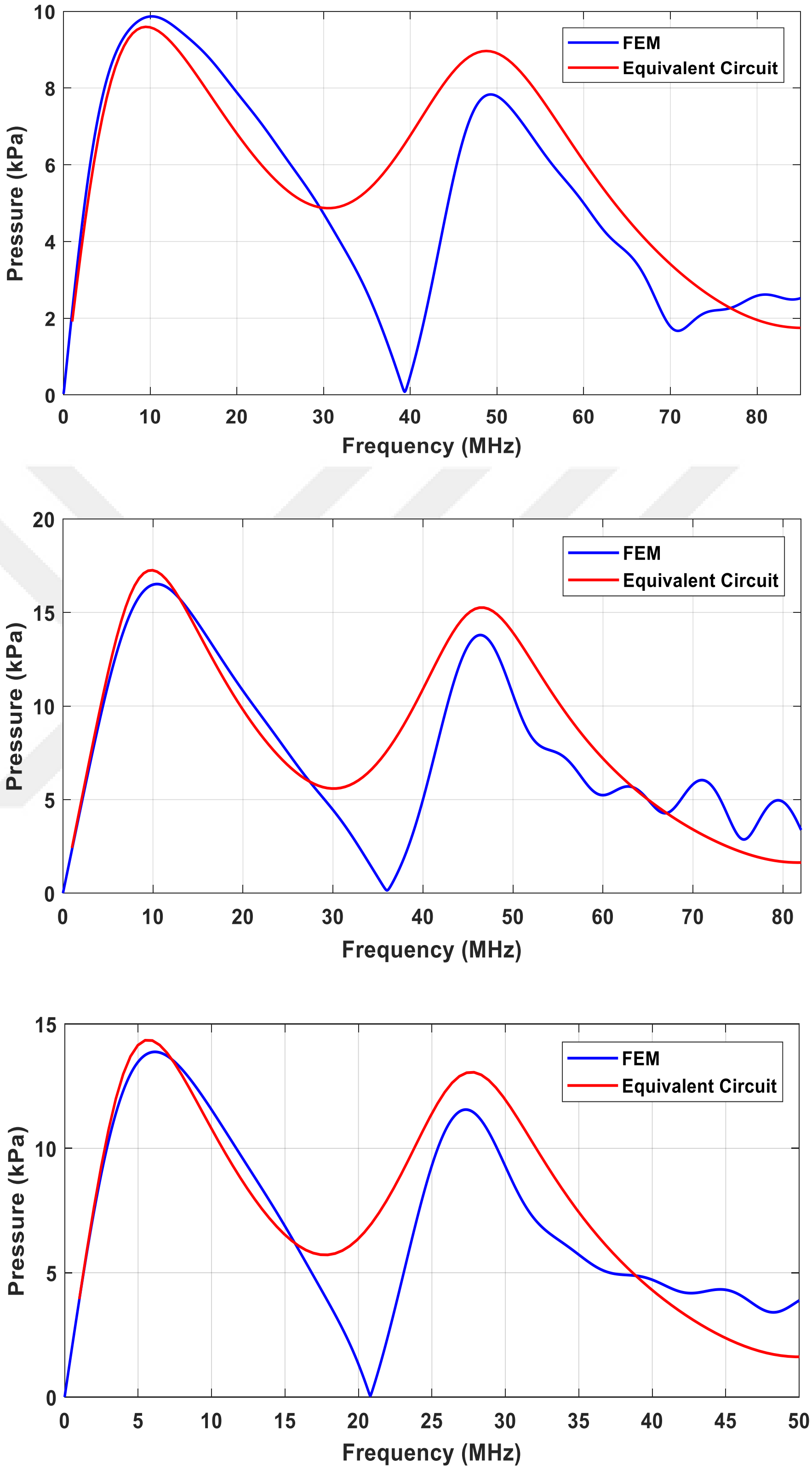

Figure 55: Comparison of FEM and new equivalent circuit results for output pressure vs. frequency for a membrane radii 10 μm, 17 μm and 30 μm, respectively.

3.2.2. Equivalent Circuit Model vs. Experiment

We further investigated our model comparing the results with the experimental data which was used in [58] for transmission mode (TX) of a CMUT. The experimental data which was used belongs to a 60 μm radius membrane design that has three layers; 0.4 μm thick SiC, 3.6 μm thick SiGe and 1.5 μm thick SiO_2 from bottom to the top of the membrane, respectively. Also, the membrane has full bottom electrode coverage with a vacuum gap of 200 nm. The immersion medium in which the CMUT cell was tested is Fluorinert (FC-84, 3M, USA). The density and speed of sound of the fluid are 1730 kg/m^3 and 537 *m/s*, respectively. Acoustic pressure was detected a few millimeters away from transducers surface using a hydrophone (HNP1000, Onda Inc., USA). A pre-amplifier was used to amplify hydrophone signal and the signal was recorded with an oscilloscope (TDS3014B, Tektronix, Inc., USA). All the instruments were controlled with a Labview (Labview, National Instruments, USA). program. The CMUT cell was driven with a 15 V, 50 ns duration pulse and 100 V DC bias. It is clear from the Figure 56 that our model is in good agreement with the experiment.

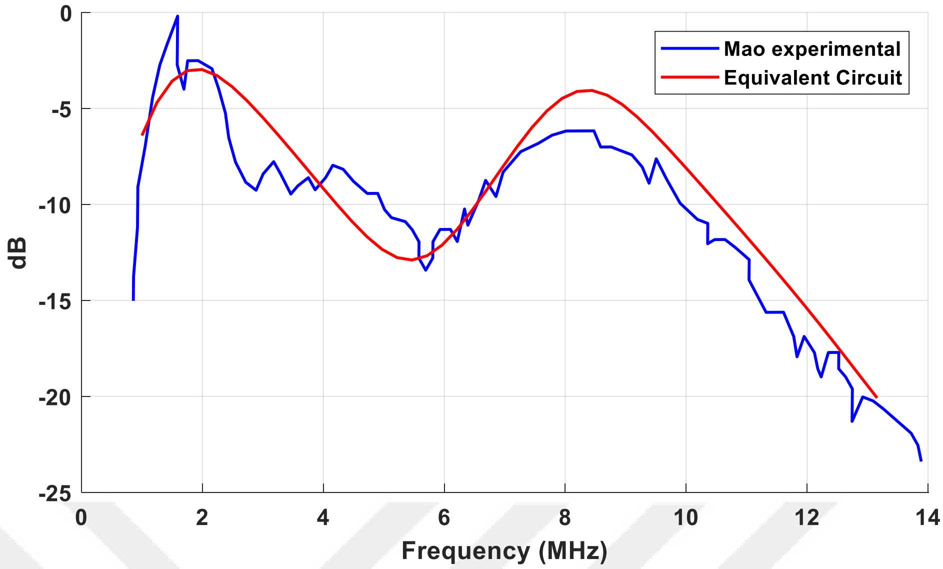

Figure 56: Comparison of equivalent circuit model with experimental data and FEM. Experimental data was taken from [59]. Exact value of 0 dB wasn't provided in the experiment. In the equivalent circuit, bias voltage was kept at 80% of the collapse voltage and 1 V excitation signal was superimposed on DC bias. 0 dB corresponds to 6.35 kPa under these conditions.

3.2.3. Summary

In this work, we have developed and presented an equivalent circuit model for a single circular CMUT. Circuit parameters can be calculated using simple, well known equations and material properties of a membrane. The circuit tested for several different membrane dimensions and the results agreed with FEM simulations. We showed that the model predicts CMUT dynamics accurately over a wide frequency range, including anti-resonances.

CHAPTER IV

4. ULTRA WIDE BANDWIDTH CMUTs

4.1. Harmonic Imaging

When a low pressure (<0.5 MPa) is applied to tissues, the propagation of ultrasound waves is linear, which means that the deformation is elastic, in which wave velocity at the compression and expansion is same. On the other hand, when the tissue is exposed to pressure higher than 0.5 MPa, ultrasound wave propagation becomes nonlinear [146]. This means that the sound travels faster through compressed tissue than relaxed tissue. This behavior generates harmonics. The distortion depends on the emitted pulse amplitude and wave's travel distance. In addition, for low amplitudes it is hard to observe the effect whereas, for high amplitudes the effect is substantial [147]. The nonlinear acoustic wave propagation was first observed by Cartensen et al [158]. Later, tissue harmonic imaging (THI) was introduced in 1997, in which the image was constructed from second harmonic energy [146]. Tissue harmonics are produced as the pulse travels through the tissue. As the transmitted wave travels through, infinitesimal amount of harmonics are produced and harmonic intensity increases [149] as shown in Figure 57.

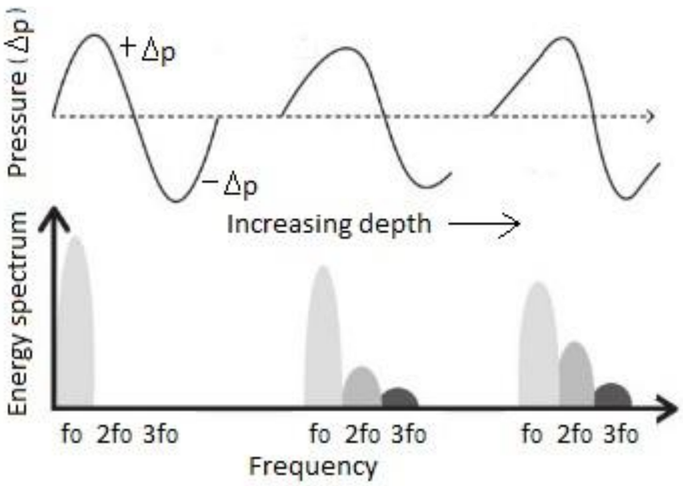

Figure 57: Harmonic wave generation with increasing depth [171]

For example, if the fundamental frequency is (fo) integral multiples of the fundamental frequency, 2fo, 3fo are generated as shown in the Figure 58.

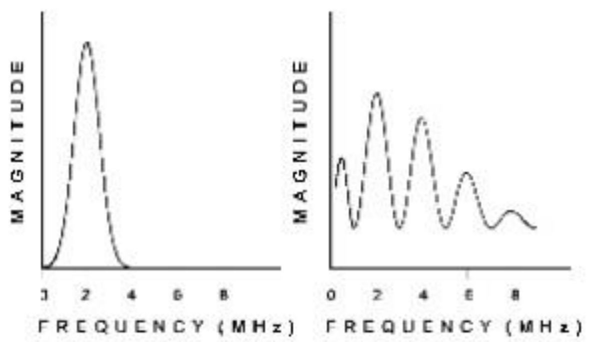

Figure 58: Transmitted fundamental frequency and received harmonic frequencies [170]

Fundamental frequency attenuate linearly as the penetration depth is increased. Tissue harmonic intensity increases with depth until tissue attenuation becomes high to stop this built-up [149] as shown in Figure 59.

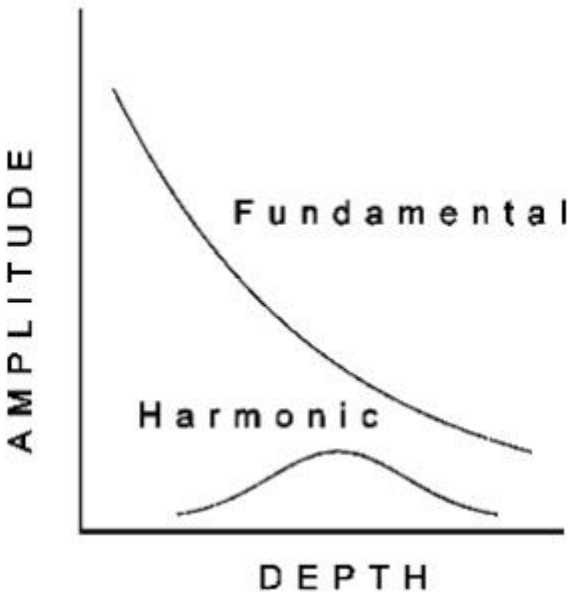

Figure 59: Behaviour of harmonic and fundamental waves in tissue [170]

On the transmit cycle, only the fundamental frequency must be sent through the tissue and hence on the receive cycle, the harmonics will come only from the tissue. Otherwise, the fundamental and harmonics will overlap and the image contrast will be affected adversely [149].

4.2. Why Harmonic Imaging?

THI has advantages over fundamental frequency imaging. First of all, in conventional fundamental mode ultrasound imaging, the beam must pass through the body wall twice. This causes a clutter in image. Also, the beam at the focal zone is narrower in harmonic beam, this increases the resolution. Moreover, increased signal to-noise ratio results in better tissue contrast enhancement. Furthermore, due to less artifacts both axial and lateral resolution is improved. Harmonics can also be generated by the contrast agents [150]. In this case, harmonics are generated by contrast agents but not by the tissue.

4.2.1. Artifacts

In conventional B-mode Ultrasonography imaging suffers from artifacts. Artifacts in ultrasound imaging disrupt the image quality by displacing, masking, enhancing or duplicating image elements [151]. When waves travel through between the layers of fat and muscle image degradation may occur because the acoustic properties of the tissues are different. Such mismatches between the tissue boundaries generate artifacts. Moreover, beams may project radially from the main beam axis, which may create echoes detectable by the transducer. In addition, when two reflective interfaces are closely spaced, artifacts may be generated. The origin of these artifacts is weaker beams, produced on either side of the main lobe of the transmitted beam [147]. Artifacts can be divided into two categories depending upon the direction of the ultrasonic wave. These are axial and lateral artifacts as given in Figure 60.

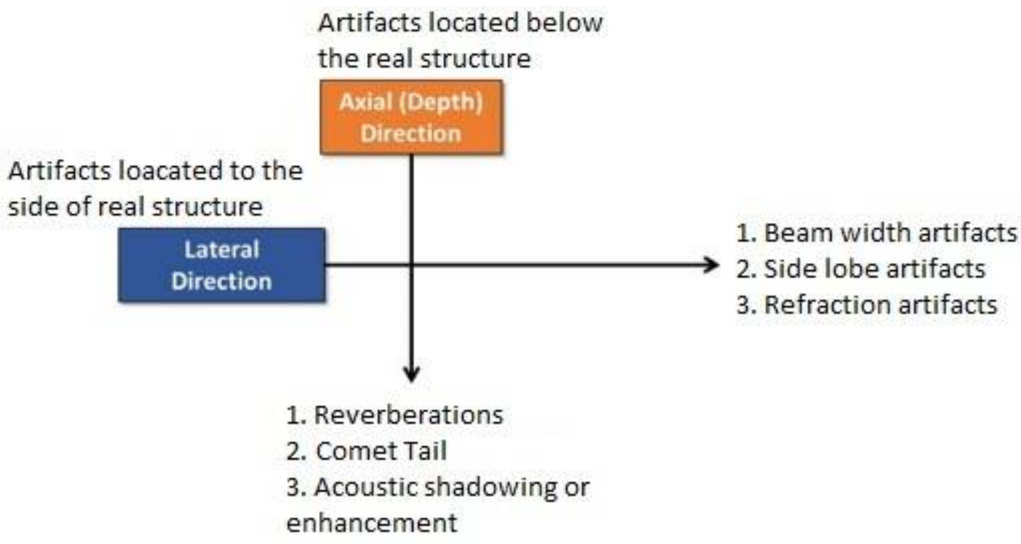

Figure 60: Ultrasound Artifacts [151]

4.2.1.1. *Artifacts in Axial Direction*

The axial artifacts include simple and complex reverberations, mirror image artifacts and acoustic shadowing [151].

4.2.1.1.1. *Simple Reverberations*

In an ideal pulse echo duration, the emitted ultrasonic wave from the transducer travels through the surface of the structure and reflected back through the transducer surface. However, some of the reflected wave from the structure surface may be reflected again due to some other reflector and hence may return to the structure. The ultrasonic wave essentially goes back to the transducer after second round trip. The imaging system interprets this ultrasonic wave is coming from a structure that is further away from the original structure. Therefore, a secondary image is produced below the original image at twice the distance between transducer and the structure [151] as shown in Figure 61.

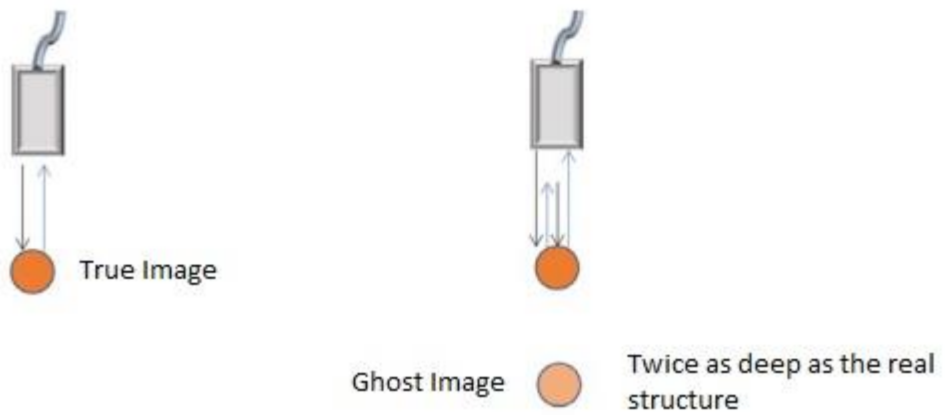

Figure 61: Reverberation Artifact [151]

4.2.1.1.2. Comet Tail

Comet tail is also known as complex reverberation artifact. It occurs due to two or more reflectors on the direction of the ultrasonic wave propagation. Due to these multiple reflectors, the ultrasonic wave does multiple round trips. Each roud trips produce ghost images all of which are further away from the original structure.

4.2.1.1.3. Acoustic shadowing and enhancement

Ultrasonic waves don't attenuate uniformly by all tissues. If a ultrasound is attenuated by a tissue much greater than the other tissues around, the strenght of the beam away from the tissue will be much weaker. Therefore, other tissues will appear too dark [151]..

4.2.1.2. Artifacts in lateral direction

4.2.1.2.1. Refraction artifacts

Ultrasound wave paths are assumed to be linear. However, the wave may encounter a structure which behaves like a lens [151]. In addition to this, while the wave goes through one medium to the other, the path of the wave bents and the speed of the wave is changed. Therefore, the object may be duplicated [151].

4.2.1.2.2. Beam width artifacts

Images aren't always obtained from the main ultrasound beam. The ultrasound beam width looks like an hourglass. The beam is as large as transducer width when it is emitted. Then, it narrows to the focal point and after that the beam is widen again. If there is a highly refractive object on the propagation path when the beam is wide, a ghost images will arise [152].

4.2.1.2.3. *Side lobe artifacts*

Most of the energy of an ultrasound beam is generated at the center of the beam. However, some of the energy is carried along the side of the beam. These beams don’t create any echoes dispersing through a tissue. On the other hand, if there is a strong reflector on the path of these weak ultrasonic beams, an artificial arc like image is produced next to the real image [147], [154].

4.2.2. How to mitigate Artifacts

Harmonic waves are predominantly created in the center of the transmitted beam. Therefore, artifacts can be reduced using harmonic waves. Harmonic beam focal beam narrower than the fundamental beam and therefore lateral resolution increases. In conventional fundamental mode, the transmitted beam passes through the tissue. The beam is reflected back towards the transducer. During this round trip the signal strength decreases. However, harmonic echoes originate within the tissue, meaning that harmonic echoes pass through the tissue only ones. Their intensity increases with depth. In summary harmonic images have improved resolution compared to fundamental mode [155].

4.2.2.1. *Ultrasound Contrast Agents*

In medical ultrasound imaging, it is crucial to increase signal strength. Therefore, contrast agents are used to alter acoustic properties of the tissue. They contain either air or low solubility gases in a lipid or albumin shell [155] as shown in Figure 62. Typically, their diameters can be 1 um to 10 um. Contrast agents resonate at the ultrasound frequency and their resonance frequency increases as their diameter decreases [156, 157]. They provide additional clinical information since echoes reflected from the microbubbles contain harmonic frequencies of the incident wave, which makes easier to distinguish objects from surrounding medium. Microbubbles generate higher harmonics than tissue does [157]. For example, in super-harmonic imaging, low frequency (f_0) ultrasound waves are transmitted to excite microbubbles and the higher order of harmonics are received with a high frequency transducer. When the amplitude of the acoustic wave increases, the harmonic content produced by a single interaction between microbubbles and acoustic wave increases [158]. Nevertheless, because of the limited frequency bandwidth of transducers super-harmonic imaging requires transducers that can transmit at a low frequency and receive harmonic components at many times higher than the transmitted frequency.

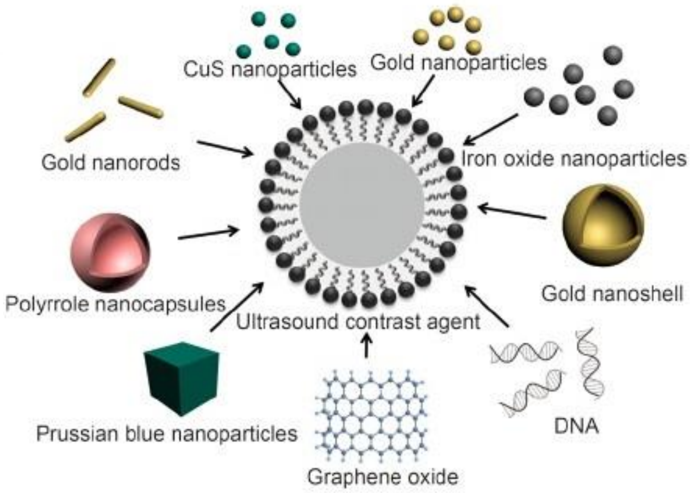

Figure 62: Ultrasound contrast agent [159].

Combination of different types of UCAs and nanomaterials including superparamagnetic iron oxide nanoparticles (SPIOs), CuS nanoparticles, DNA, gold nanoparticles (GNPs), gold nanorods (GNRs), gold nanoshell (GNS), graphene oxides

(GOs), Prussian blue (PB) nanoparticles, and polypyrrole (PPy) nanocapsules have been used (Figure 62) [159].

4.3. *Current Technology*

4.3.1. Dual-Frequency Transducers

Dual Frequency transducers are made to form images of micro-bubble harmonics by transmitting acoustic waves at lower frequencies near micro-bubble resonance (app. 1-6MHz) and receiving only higher order harmonics produced by microbubbles (app.10-30MHz). In dual frequency transducers imaging, two separate transducers for transmission and reception are used. Dual frequency piezoelectric transducers have been designed by several groups and various piezoelectric transducer have been suggested; vertically and horizontally stacked transducers [160], [161], piezo-polymers [162] and piezo-composited [163]. Recently, 6.5 MHz transmit, 30MHz receive was performed with stacked piezoelectric plates for super-harmonic imaging [164]. However, the current contrast imaging methods, the restricted frequency bandwidth of standard PZT probes limits the ability to image several non-linear components [165]. Also, they suffer from cross talk and impedance mismatch. In addition to these problems, they are difficult to fabricate especially at the smaller scale. Capacitive micromachined ultrasonic transducers have been investigated for dual frequency because they offer ease of fabrication using well known micromachining processes and large bandwidth. The CMUT operation has particularly good characteristics for dual frequency imaging. The option of a collapse mode makes it possible during the imaging procedure to switch between two modes with different characteristics. The switch between modes was adopted in dual frequency imaging. For example; in conventional mode, 70% fractional bandwidth around a center frequency of 8.3 MHz and in collapse mode, 69% fractional bandwidth was measured around 19 MHz [166]. Recently, 3-dB fractional bandwidth (FBW) for the conventional mode is 95% with 4.8 MHz center frequency and the collapse mode, the FBW is 137% with 7.8 MHz center frequency were demonstrated with CMUTs [167]. Also, there are also studies that focuses on very large band CMUT transducers that can transmit at very low frequencies and receive at high frequencies without changing the mode (e.g only conventional mode) [168].

4.4. CMUT design for Acoustic Angiography Applications

The possibility of obtaining very wide bandwidth makes capacitive micromachined ultrasonic transducers (CMUTs) the most promising candidate for acoustic angiography applications. CMUTs in excess of 100% fractional bandwidth have been demonstrated in the past. Knight et al. proposed a membrane structure with non-uniform region which was covering 80% of the membrane area. It was shown that electromechanical coupling coefficient can be improved with the new structure [20]. Later, membrane configurations, which were square, rectangular and tent shaped, were optimized to improve transmission and reception efficiencies. It was shown that tent and rectangular shaped membranes were superior to square shaped membranes in terms of transmission and reception efficiencies by 46% and 43% for tent shaped and 44% and 65% for rectangular membrane, respectively [23]. Thick gold layer was used as a center mass on the membrane to obtain more output pressure due to its high density. Hyo-Seon Yoon et al., used heavy gold electrodes aiming to obtain more piston-like motion and hence more output pressure [26]. They measured output pressures as high as 2 MPa and 1.875 MPa, respectively [26]. Sato et al. deposited thick mass layer on the membrane and with etching and shaping the mass, they achieved 3 times higher sensitivity compared to conventional uniform membranes [27]. Multiple moving membrane configuration was proposed by Emadi et al. for more signal transmission and detection. In this structure; a stack of two vibrating membrane was placed over a fixed bottom electrode [28]. Embossed pattern was used for collapse mode operation by Yu et al. Carefully placing the embossed pattern on vibrating center of the membrane, the proposed structure increased the output pressure by 51.1% and 88.1% for embossed pattern made of Silicon Nitride and Nickel, respectively [29]. Jiang et al. used slotted membrane structure (tranches obtained etching the membrane at the anchor side) and modified the structure adding rings on the non-slotted regions between trenches (corrugated structure). They reported an increase in electromechanical coupling coefficient and receive sensitivity up to 20.9% and 50.5% for slotted membrane and 5% and 38.3% for corrugated membrane, respectively [30]. Embedded silicon springs were implemented in to the vacuum gap of Silicon piston plates to improve efficiency by Lee et al. They achieved higher transmission efficiency (21kPa/V) than that was obtained with several piezoelectric material such as lead zirconate titanate (PZT) [31]. A six mask sacrificial release process was proposed for annular embossed CMUT made of Nickel by Yu et al. [32]. For bandwidth improvement various methods and membrane geometries have been proposed. One straight forward method is to use membranes with different radii. In [21], two mixed size CMUT arrays optimized in terms of membrane thickness, radius and gap width to maximize the gain and bandwidth. It was shown that fractional bandwidth can be increased 55% and 58% for arrays with mixed sized CMUTs compared to conventional arrays. Although it is easy to integrate membranes with multiple radii on the same substrate, it is not easy to change the gap. Therefore, all the membranes should have the same gap height. This result in varying collapse voltage with membrane radius and it is not possible to operate all the membranes with the same efficiency. A.Hall et al. deposited thick gold layers at peak displacement locations to control the higher order modes of the membrane. They managed to increase both receive sensitivity and bandwidth [22]. Senlik et al. used a rigid mass on the center of the membrane to push the anti-resonance frequency to higher frequencies and hence increased the bandwidth. It was shown that it is possible to trade between gain and bandwidth [25]. Guldiken et al. proposed non-uniform membrane with dual electrode aiming to increase both electromechanical coupling coefficient and FBW. They obtained a coupling coefficient of 0.82 and FBW of 136% [33]. Huang et al. developed piston shaped membranes. The developed structures achieved 100% improvement in transduction efficiency and the 150% and 175% FBWs were obtained for square and rectangular piston shaped membranes, respectively [34]. We designed high frequency ultra-wideband 1D CMUT arrays for acoustic angiography applications. We used a non-uniform membrane profile, which was constructed adding a mass on top of the vibrating plate, and optimized the mass dimensions. Moreover, the bottom electrode shape and size were designed to improve bandwidth of the devices. In the following section, we report the design steps in detail.

4.4.1. Membrane geometry

Figure 63 shows the cross section of a single cell of the proposed membrane geometry. The membrane is composed of silicon layer on top of silicon passivation layer. This structure was built using the fabrication process developed previously [69].

The top silicon plate is non-uniform and has an annular ring as shown in the Figure 63. The total radius (a+b+c), the thickness of the mass (d) and the electrode radius of the plate (e) were optimized to obtain maximum bandwidth with a reasonable output pressure. The height of the vacuum gap was fixed at 0.25um (g=0.25 micron). The plate thickness was chosen as thin as possible to obtain broad bandwidth without causing any fabrication failure or complexity. Therefore, the fabrication process was optimized for 0.2 micron thick silicon on 0.2um silicon nitride plate (t1=0.2 micron, t2=0.2 micron). Young's modulus, density and Poisson's ratio used for Silicon were $148 * 10^9$ Pa, 2328 kg/m^3 and 0.17, respectively [171]. For Silicon nitride, Young's modulus, density and Poisson's ratio were $260 * 10^9$ Pa, 3187 kg/m^3 and 0.27, respectively [169].

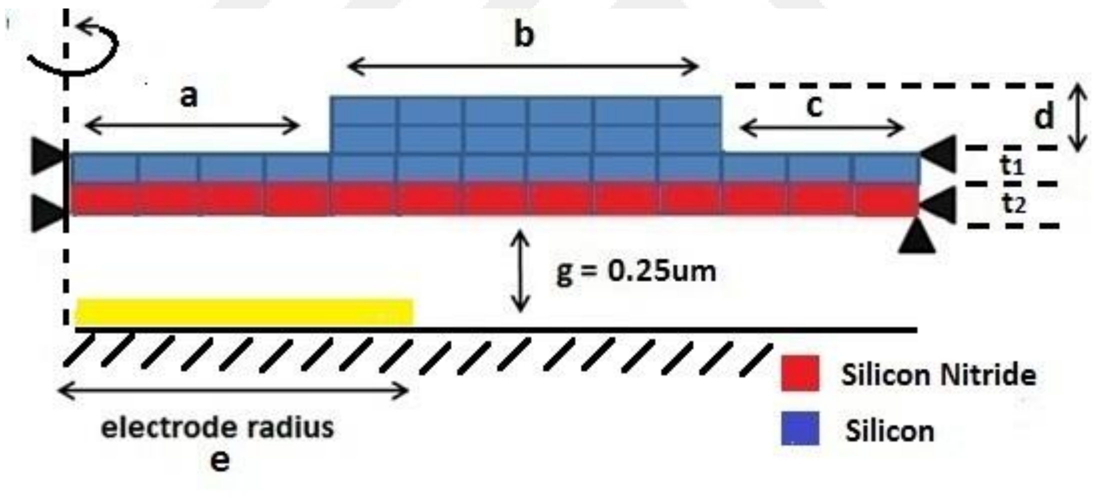

Figure 63: The proposed plate design. The geometry is axisymmetric along the line going through the membrane center.

4.4.2. FEM Calculations

We optimized the parameters of the membrane shown in Figure 63 using finite element analysis. There were several FEM models developed in the literature to simulate CMUTs. 2D as well as 3D modeling of CMUTs was demonstrated [39-51].

The models used in this study were constructed using commercially available FEM package (ANSYS 14.5, ANSYS Inc., Canonsburg, PA). The membrane (the annular ring shaped silicon mass, the silicon plate and the silicon nitride passivation layer) was built using axisymmetric plane elements (PLANE42) and solid elements (SOLID45) in 2-D and 3-D, respectively. Symmetry boundary conditions were applied to cover the transducer area and hence a periodic replication of the membranes was obtained to imitate large CMUT element. The electrostatic force was applied between the top and the bottom electrodes by electromechanical transducer elements (TRANS126). The top nodes of these elements were attached to the membrane and the bottom nodes were clamped. The immersion medium was modeled using FLUID29 elements in 2-D models. In 3-D models, FLUID30 elements were used. The immersion medium was made long enough so that the reflections from the end of the fluid medium didn't disturb the calculations which were made using transient analysis. 2D models were used to optimize the membrane geometry since they run much faster than 3D models. 2D models last 20 to 30 minutes while 3D models may take several hours to calculate output pressure.

4.4.2.1. 2-D FEM

In the 2-D model described above, the collapse voltages of the devices were found using static analysis (Figure 64). In static analysis, starting form 0 volt a DC bias was applied (Figure 65), and iterated until the maximum converged voltage, which was collapse voltage. Then, the bias voltage was set to 80% of the collapse voltage and time-transient analysis was performed to obtain the bandwidth and the output pressure.

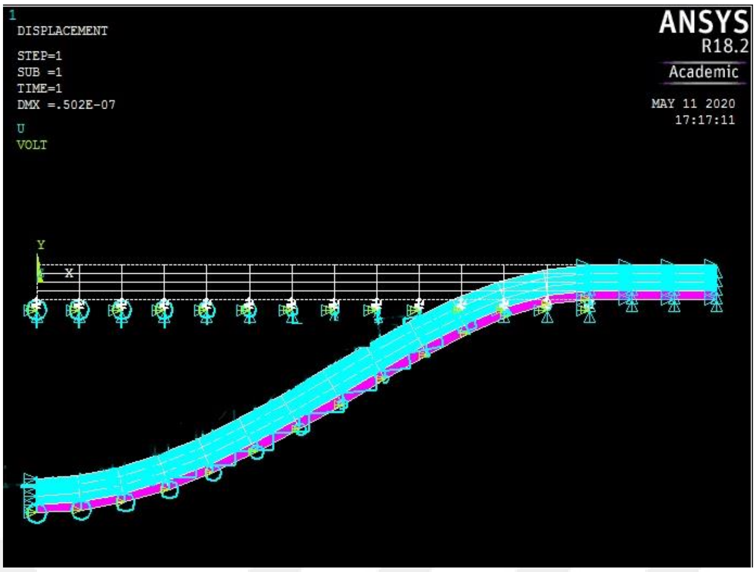

Figure 64: An example of a deflection of a membrane under DC bias

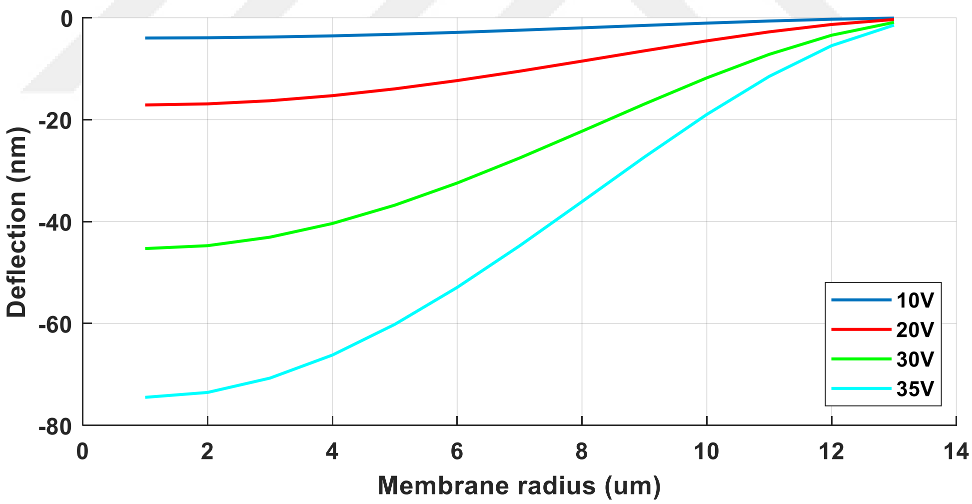

Figure 65: Deflection profile for different bias voltages of a membrane with 13um radius, 0.4um thickness and 13um electrode radius (the second design which is shown on the table 6)

First, the effects of plate dimensions on bandwidth and output pressure were evaluated. Therefore, no mass was added on the top of the membrane (d=0um).

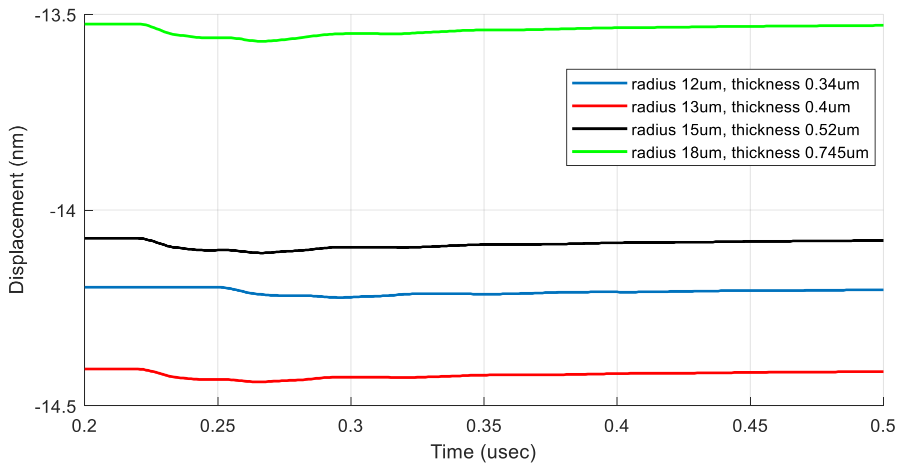

Figure 66: Transient deflection of the membranes of various thicknesses and radii

Figure 66 shows results for various membrane thickness and radius pairs in time domain. The bandwidth was calculated by finding the Fourier transform of the deflections of the membrane in time domain. As previously explained, velocity was found taking the derivative of the deflection. Then, using Matlab fft function for Fast Fourier Transform, velocities of the membranes were converted in frequency domain. After that, velocities were multiplied by the impedance of the water which is 1.5 MRaly and hence output pressures were obtained as shown in Figure 67.

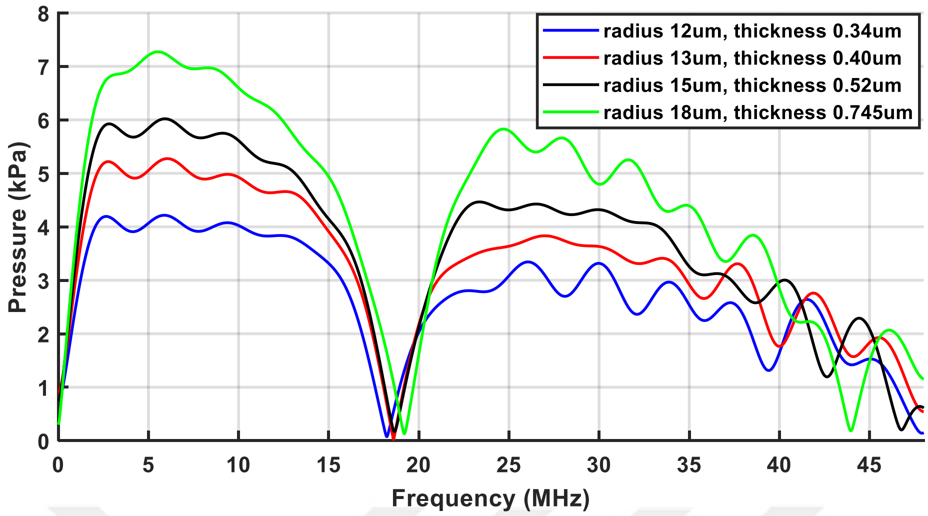

Figure 67: Effect of plate dimensions on bandwidth and output pressure

Table 6 summarizes the plate dimensions and corresponding bandwidths that were evaluated. Thin plates (<0.8um) were used because among the membranes that have the same center frequency the thinnest one has the broadest bandwidth due to their low stiffness. The plate radii (a+b+c) were chosen to keep resonant frequency constant. The resonant frequencies of MCAs that will be used in this application are 3 MHz and hence we kept the 3dB low cut frequency less than 3MHz. All the membranes were fully metallized (e was equal to a+b+c).

Table 6: The plates' radius and thickness pairs that were used for the CMUT designs and their corresponding bandwidths

Radius (um)	Thickness (um)	Bandwidth (MHz)
12	0.34	14.6
13	0.40	14.4
14	0.46	14
15	0.52	13.7
16	0.59	13.4

17	0.67	13.2
18	0.75	12.8

It was observed that; as the thickness and radius of a membrane was decreased, bandwidth increased. The maximum bandwidth was achieved when the thickness and radius were 0.34um and 12um, respectively. However, due to fabrication difficulties that might arise, radii smaller 13um and thicknesses smaller than 0.4um weren't considered and hence we fixed the plate radius and thickness to 13um and 0.4um, respectively for the rest of the design steps.

As a second design step, the effect of electrode radius (e) on bandwidth and output pressure was investigated. It is known that small electrode area is required in order to increase electrical bandwidth [137]. The change of bandwidth and output pressure with respect to the electrode radius can be seen in Figure 68. It was observed that as the electrode radius was decreased, the third mode peak shifted towards to higher frequencies with decreasing amplitude (Third mode peaks (a)) while reappearing inside the band which resulted in larger bandwidth (Third mode peaks (b)). On the other hand, reduced electrode radius resulted in lower pressure. Therefore, there is a trade-off between bandwidth and pressure. The corresponding bandwidths and output pressure are given in Table 7. Furthermore, the negative peak pressure must be at least 0.8MPa to properly excite the MCAs and hence the minimum electrode radius that could be used was found to be 5um.

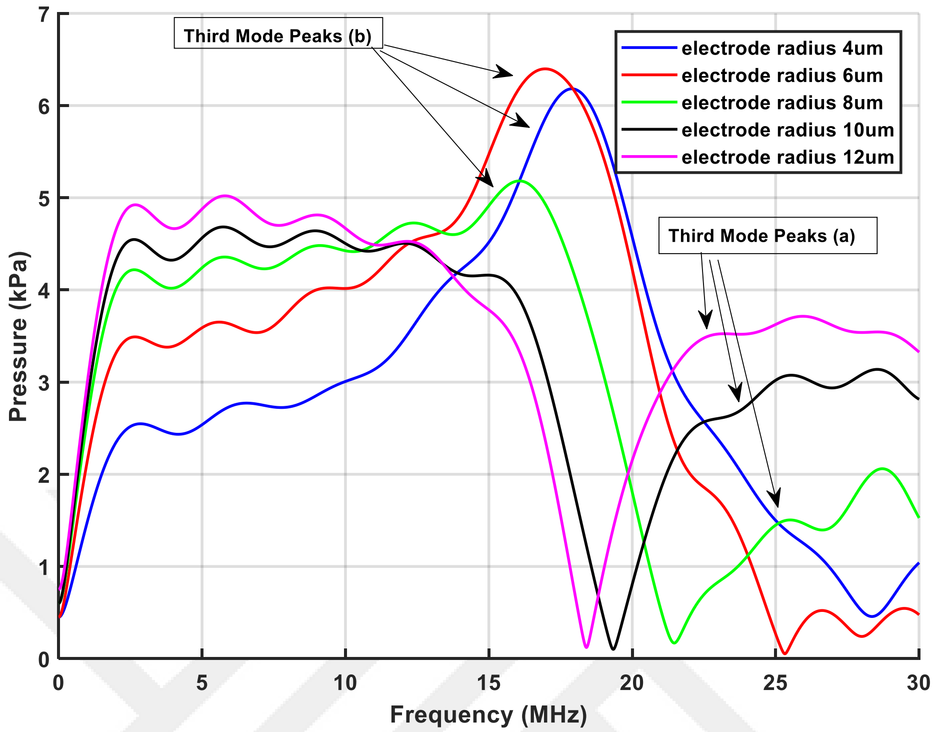

Figure 68: Effect of Electrode radius on bandwidth and output pressure

Table 7: The Electrode radii of CMUTs and corresponding output parameters

Electrode Radius (um)	Bandwidth (MHz)	Pressure (kPa)
4	22.1	2.77
5	21.2	3.23
6	19.5	3.64
7	18.7	4.15
8	17	4.36
9	16.4	4.68
10	14.9	4.72
11	14.8	4.92
12	14.5	5.02

The next step was to add a silicon mass on top of the plate ($d \neq 0$) while keeping the electrode radius (e) fixed at 5um. We found out that adding a mass on the top of the membrane, the third mode peak can be further shifted towards the higher frequencies.

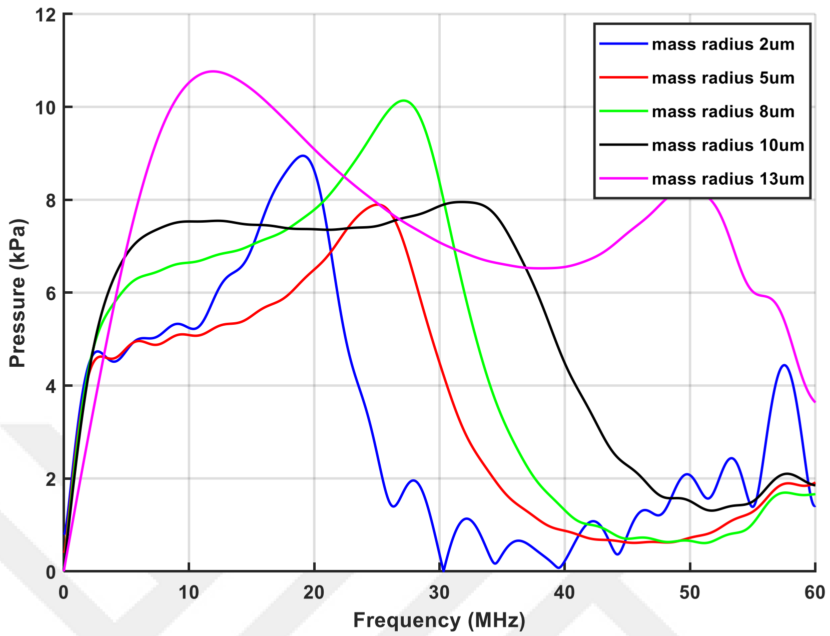

Figure 69: Effect of mass radius on bandwidth and output pressure

Here, there is no etching on the center portion of the membrane and hence the mass radius was uniform on the plate. The effect of the mass on bandwidth and pressure is shown in Figure 69. For simplicity, first, the mass thickness was chosen equal to the plate thickness ($t_1 + t_2$ was equal to d). It is clear from the Figure 70 that as the mass radius was increased bandwidth also increased whereas, the bandwidth decreased when the mass radius was bigger than 12um because mass stiffness became more dominant than the membrane stiffness. Moreover, we observed that when the mass radius was increased more than 10um a notch started to appear in the band between the first and third mode peaks close to 3dB level. Therefore, we kept the mass radius at 10um (a+b was 10um and c was 3um) in the next design steps. Pressure was found to be increasing as the mass radius increased since the total stiffness of the membrane increased. In

Table 8, the mass radii and corresponding bandwidths and output pressures were summarized.

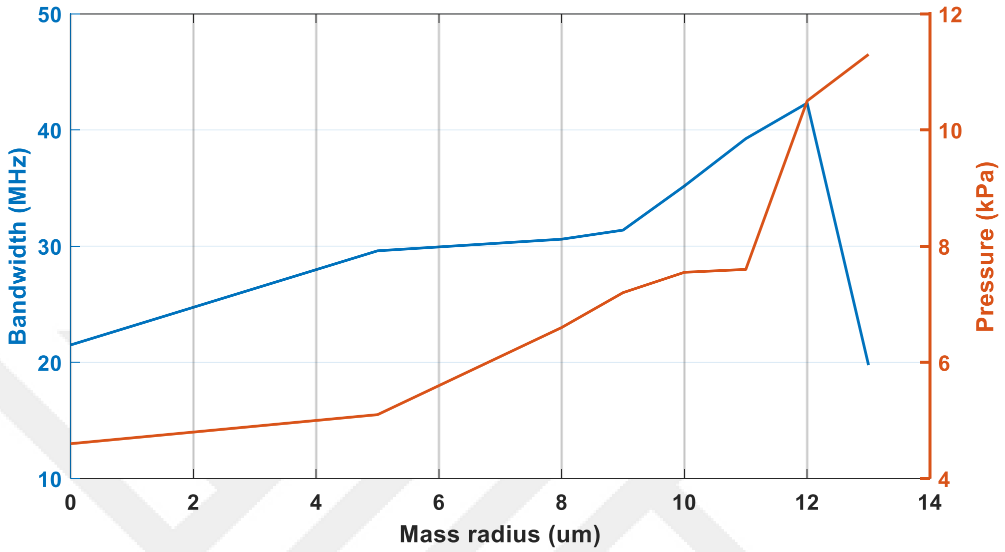

Figure 70: Effect of Mass radius on bandwidth and output pressure

Table 8: Mass radius and corresponding bandwidth and output pressure

Mass Radius (um)	Output Pressure (kPa)	Bandwidth (MHz)
0	4.6	21.5
2	5.02	22.75
5	5.1	29.6
8	6.6	30.6
9	7.2	31.38
10	7.55	35.18
11	7.6	39.25
12	10.5	42.31
13	11.3	19.76

In the next step, we analyzed and optimized the mass thickness (d) to obtain broader bandwidth. In this step, the mass radius (a+b) and electrode radius (e) were fixed at 10um and 5um, respectively. Several mass thicknesses were evaluated on top of vibrating plate as shown in Figure 71.

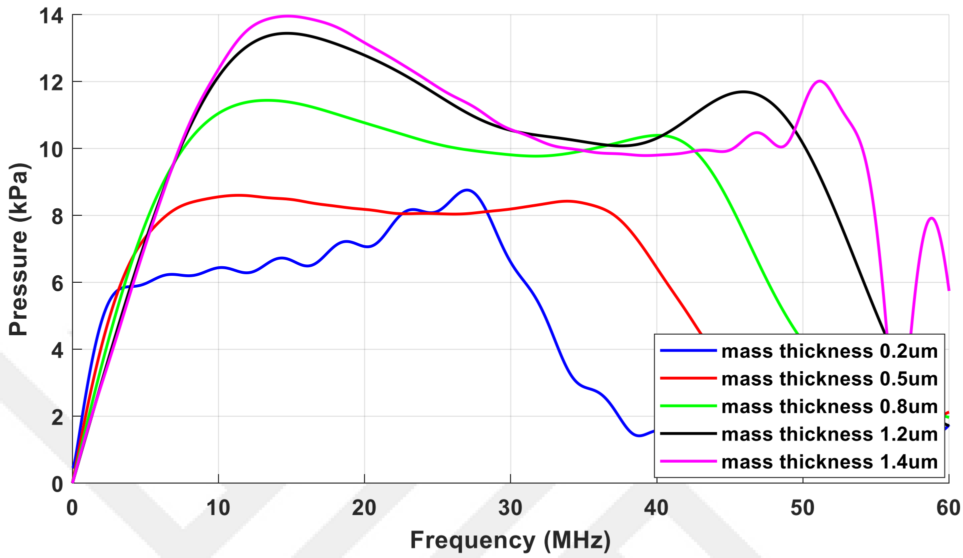

Figure 71: Effect of mass thickness on bandwidth and output pressure

Bandwidth was found to be increasing up to mass thickness of 1.2um, and then a decrease was observed (Figure 72). The reason of this decrease is that the stiffness of the mass overcomes the stiffness of the membrane [25].

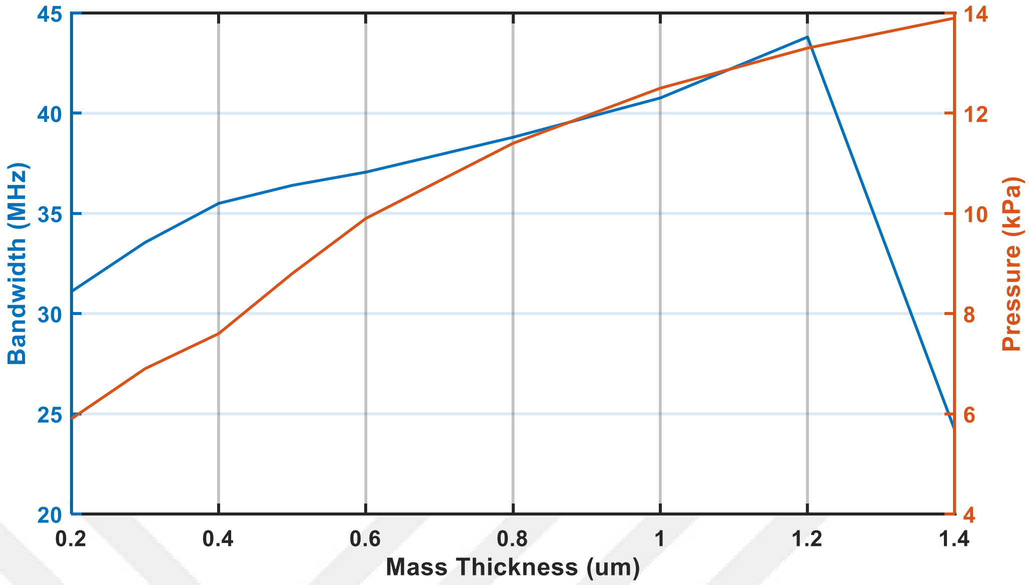

Figure 72: Effect of Mass thickness on bandwidth and output pressure

Table 9: The bandwidth and output pressure for different mass thicknesses on CMUT plate.

Mass Thickness (um)	Bandwidth (MHz)	Pressure (kPa)
0.2	30.9	5.8
0.4	35.3	7.5
0.5	37	8.5
0.6	38	10
0.8	40	11.3
1	42.1	12.7
1.2	43.8	13.4
1.4	24.2	14

Moreover, it was observed that as the mass thickness increased the band shifted to higher frequencies. The 3dB bandwidth was found as high as 43.8 MHz, whereas when the mass thickness was 1.2um 3dB low cut of reached 6.9 MHz as shown in Table

10, and therefore increasing the mass thickness over 0.4um wouldn't be practical for acoustic angiography applications that require low transmit frequency.

Table 10: The change of 3dB low & high cut off frequencies depending upon the mass thickness.

Mass Thickness (um)	0.2	0.4	0.6	0.8	1	1.2	1.4
3dB low cut off (MHz)	1.7	2.7	4.1	5.3	6.2	6.9	7.2
3dB high cut off (MHz)	32.6	38.1	42.1	45.3	48.3	50.7	31.4

Consequently, the most suitable mass thickness was found as 0.4um and hence the final design has 0.4um thick (d), 10um mass radius $(a + b)$ on the top of 0.4um thick $(t_1 + t_2)$ and 13um plate radius $(a + b + c)$ with 5um radius bottom electrode (e). The corresponding bandwidth was shown in Figure 73. The 3dB low cut off and high cut off were measured as 2.7 MHz and 38.1MHz, respectively.

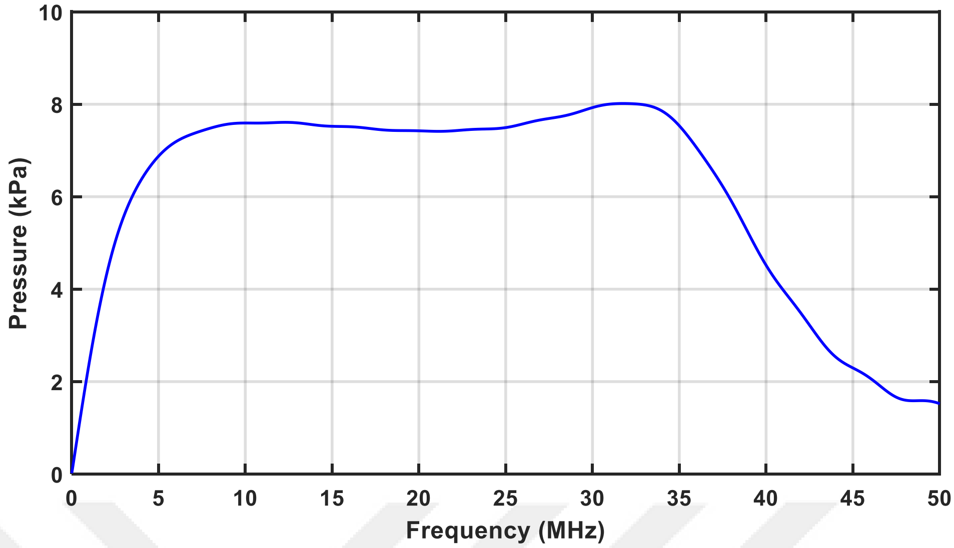

Figure 73: The optimized 2D FEM design of a CMUT

Figure 73 shows a very wide bandwidth operation. This CMUT operates from 2.7 MHz to 38.1 MHz which is very suitable for harmonic imaging. Another requirement for harmonic imaging is to generate high negative pressure in the medium. To demonstrate this capability, the CMUT is biased at 80% of the collapse voltage and it is driven by 3 MHz pulse excitation. The obtained pressure output is shown in Figure 74. The maximum negative pressure output is 0.86 MPa which is enough to generate harmonics in the tissue.

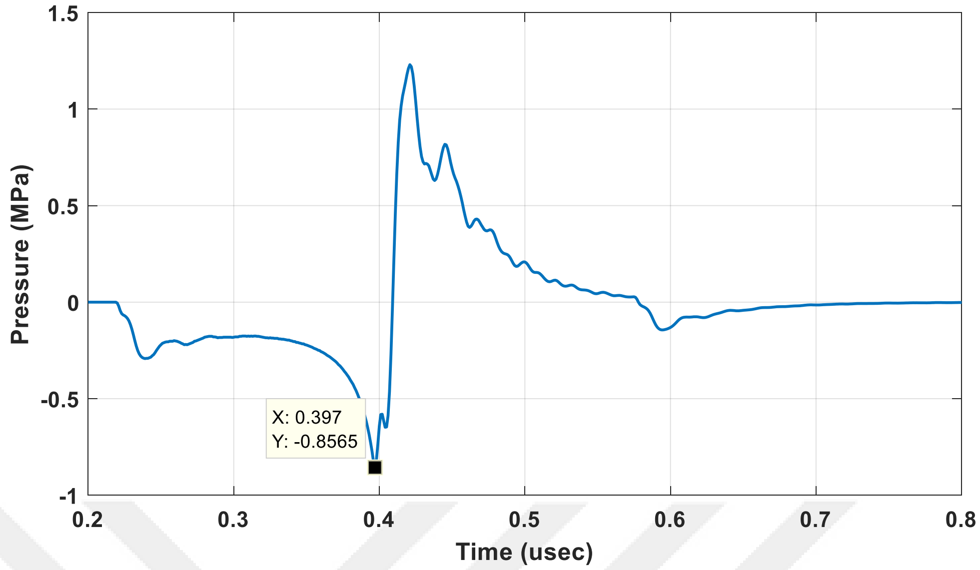

Figure 74: Maximum negative peak pressure that can be obtained from the design.

4.4.2.2. 3-D FEM

In the previous section we demonstrated the design of a very wide bandwidth CMUT. Our 2D FEM models run in relatively reasonable time duration and we managed to do the optimization using a 2D model. However, 3D models are more accurate compared to 2D models. In this section we will verify the results using our 3D models.

3-D models were constructed using the optimized plate & mass dimensions and electrode radius that were found with 2-D FEM simulations to verify the results that were obtained using 2D FEMs. There were slight changes between 2-D and 3-D models in terms of bandwidth and pressure. The difference arises because in 3-D models, we implemented the bottom metal connection lines, which were neglected in 2-D FEM as well as 3D models reflects more accurate boundary conditions. When the CMUT is fully metallized the effect of the bottom connection lines are negligible. However, when the electrode radius gets smaller the effect can't be neglected anymore because connection lines changes both collapse voltage and average velocity of the plate. Therefore, FBW that obtained from 3-D FEM was smaller than that was found with 2-D FEM as shown in Figure 75. The 3dB low cut off was slightly shifted to lower frequency (2.3 MHz) and high cut off decreased to 33MHz.

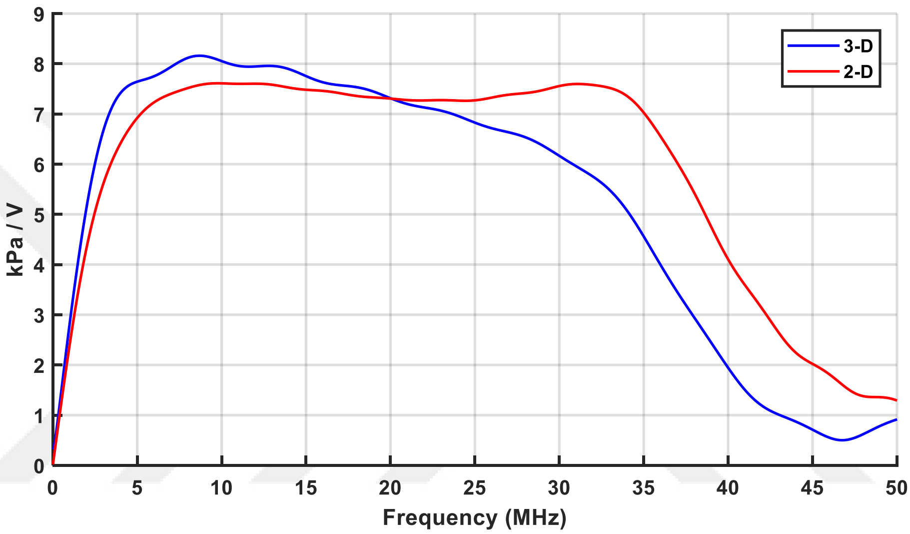

Figure 75: Comparison of 2D and 3D FEMs with the same parameters

Based on the 3D simulations we slightly modified the membrane geometry. The membrane was etched from its center which means that a ring shaped mass was left on top of the plate (b=5.5um, d=0.4um). As a result, the 3dB low cut of decreased to 1.8MHz and bandwidth slightly increased to 33.5 MHz as shown in Figure 76.

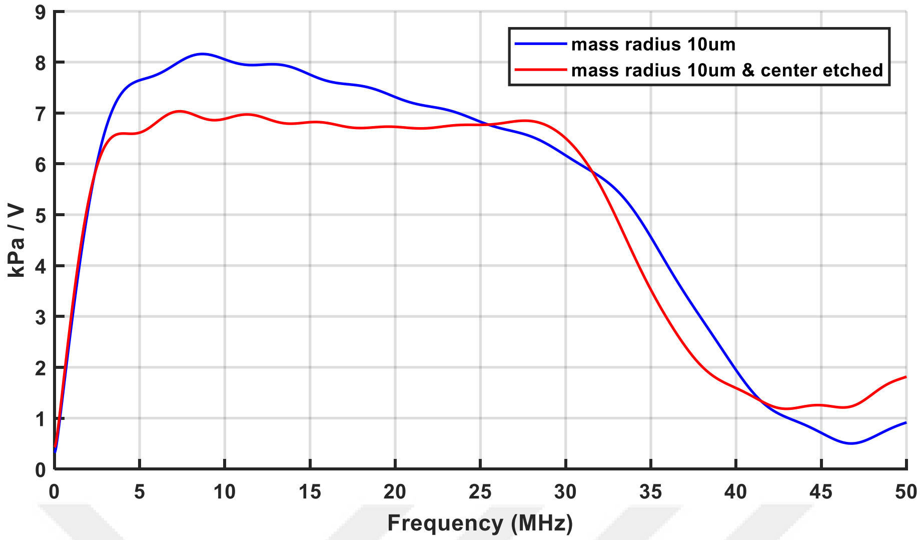

Figure 76: Comparison of two 3D FEMs; one was center etched and the other one was without an etch.

The plate topology is now similar that was used in [22]. However, in [22], the gold mass on the top of the plate was chosen because of its low stiffness and high density, whereas the silicon mass only serves as a stiffener in our plate design. In Figure 77, the effect of material properties of the mass on bandwidth was investigated. Therefore, density and Young's Modulus of the silicon mass was changed. First, the density of the silicon mass was decreased to 1164 kg/m^3 (half of the original value) while Young's Modulus was kept the same. Then, Young's Modulus was taken as $74 * 10^9$ Pa (half of the original value) and 296*10^9 (double of the original value), respectively while the density of the silicon mass was kept at 2328 kg/m^3.

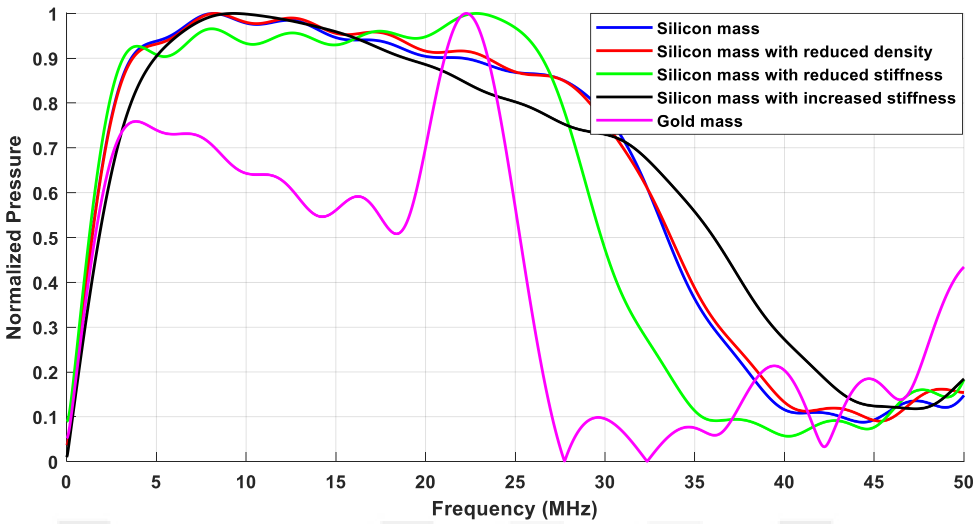

Figure 77: The effect of material properties on bandwidth

As it is clear from the Figure 77, decreasing the density of the silicon mass on top of the plate didn't affect the bandwidth. Moreover, using heavy gold mass instead of silicon drastically reduced the bandwidth. On the other hand, when the stiffness of the mass was increased the bandwidth was increased slightly and decreasing the stiffness led lower bandwidth. After the design steps explained above, the complete CMUT membrane is shown in Figure 78.

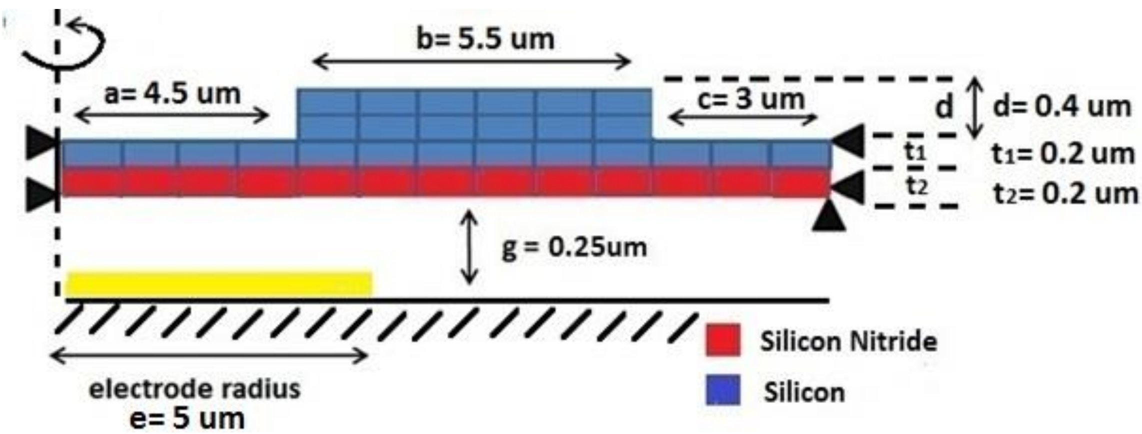

Figure 78: The complete membrane design

4.4.2.3. Fabrication of the FEM design

We fabricated the above design in Nanofabrication Facility (NNF), a facility of North Carolina State University, North Carolina, USA. We fabricated the CMUTs on a glass substrate. The substrate was a standard 0.7-mm thick, 100-mm borosilicate glass wafer (Borofloat® 33, Schott AG, Germany). The substrate was cleaned with Piranha solution to remove contaminants (Figure 79a). The cavities were patterned using a positive tone photoresist (Shipley 1813), and the patterned features on the glass substrate were etched using deep reactive ion etching (Figure 79b). After the dry-etching, using 10:1 BOE solution the cavities were smoothened out to reduce the roughness in the cavities. A total etch depth of 400nm is achieved (Figure 79b). After the etch process, the photoresist was removed and the bottom electrodes were patterned using LOR and positive photoresist (Figure 79b). Using e-beam evaporation and lift-off, 150-nm thick bottom electrodes were defined (Figure 79b). Figure 80 shows the optical images of the devices with different bottom electrode structures. Figures 81 (a) and (b) show the optical image and AFM image of the reduced bottom electrode structure, respectively. Then, 200-nm conformal PECVD silicon nitride is deposited that serves as insulation layer and passivation layer on the device layer of the SOI wafer. The silicon nitride layer prevents the short-circuiting of the electrodes and at the same time acts as a passivation layer. Therefore, so that the trapped gases in the cavities after anodic bonding are not leaked in the silicon device layer. The SOI and the processed glass wafers were anodically bonded (Figure 79c).

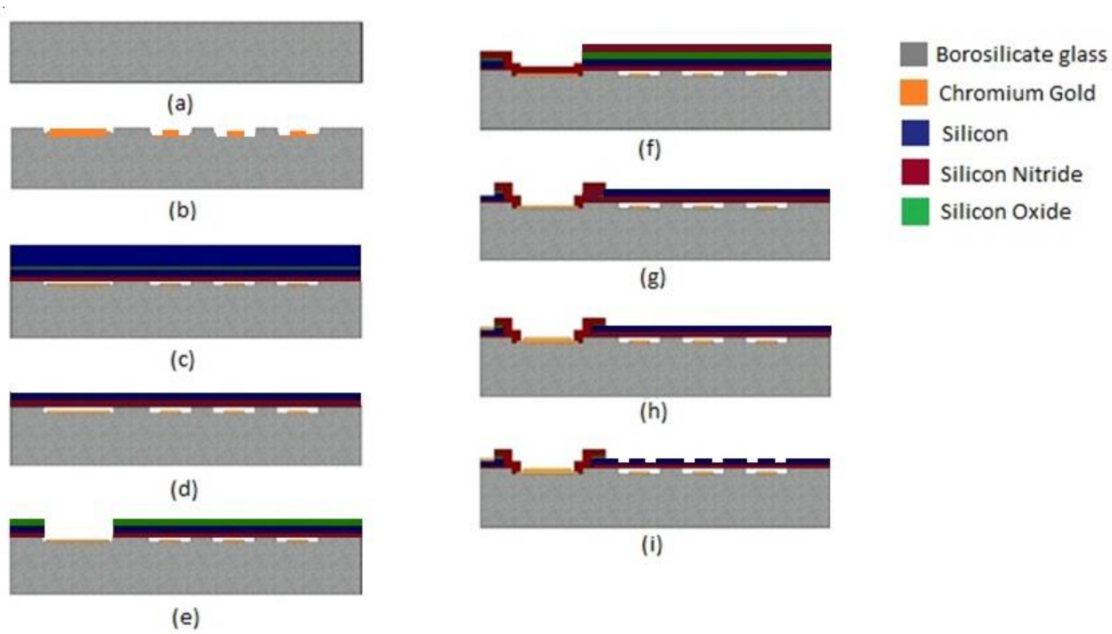

Figure 79: (a) Clean glass substrate. (b) Bottom electrode definition after the first two photolithography steps. (c) Anodic bonding of the patterned glass wafer and SOI wafer. (d) Handle layer removal. (e) Outgassing of trapped gases. (f) PECVD silicon nitride deposition for vacuum-sealing. (g) Silicon nitride etch on both the active plate area and on the bottom pads locations. The plate is also thinned-down at this step. (h) Top metal deposition. (i) Plate patterning.

After bonding, the handle wafer was thinned to 100μm by grinding, and the rest was removed by heated TMAH solution. The underlying buried oxide layer was kept on the membrane and used as an etch buffer/stop layer for etching the nitride on top of the plate in the consequent steps (Figure 79d). Next, we dry-etched through the buried oxide, silicon, silicon nitride layers (Figure 79e) at the pad locations. This step helps evacuate the trapped gases in the cavities generated during anodic bonding, allows access to the bottom electrodes on the contact pads, and defines the dicing lines for separating the devices. We then deposited 1.5-μm conformal PECVD silicon nitride to seal the cavities (Figure 79f). After sealing, we dry-etched the silicon nitride on the bottom electrode pads to form contacts. Then, another dry-etch process was used to remove silicon nitride on the active areas. The buried oxide layer under the silicon nitride acts as an etch barrier so that the thin silicon plate is not etched since the selectivity of the dry etch was low. After the silicon nitride was fully etched on the active area, the remaining buried oxide layer was removed with 10:1 BOE solution. At this step, the 1.5-μm plate was also thinned down by dry etching to 600 nm to match the design parameters of the devices (Figure 79g). The reason behind thinning down the plate was because we started with a SOI wafer that has 1.5-μm plate thickness to fabricate the devices. One can use a SOI wafer with 600-nm silicon device layer to eliminate this step. Later, a stack layer of 20-nm chromium and 180-nm gold were deposited, and then used lift-off process to form the electrical contact pads (Figure 79h). Finally, we patterned the plate of the fabricated devices (Figure 79i). The mask was designed so that we have devices with various plate structures for comparison. 400-nm silicon was dry-etched on the edges of the cells in some arrays, and the plates on the cells on some of the arrays were not etched. Figure 82(a) and (b) show the optical images of the plate patterning where the clamped edge side of the cells is etched, and the other plate with no other etch step. At this step, the fabrication process was completed [175].

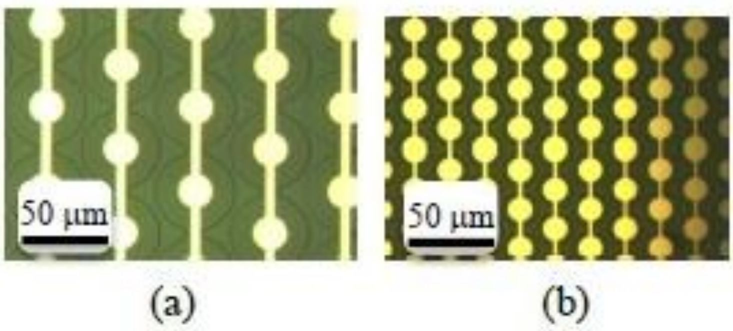

Figure 80: Bottom electrode pattern optical images: (a) Reduced bottom electrode area (b) Full bottom electrode area [175].

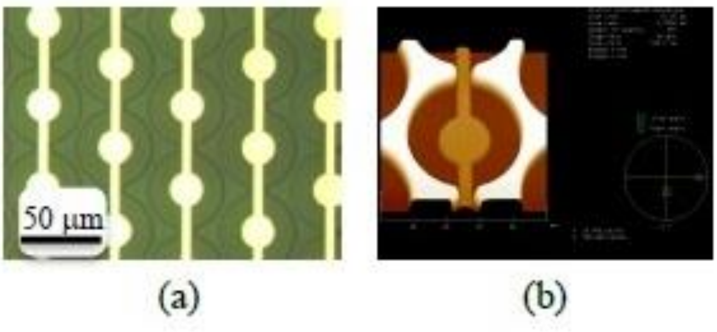

Figure 81: (a) Optical image showing the reduced bottom electrode (b) AFM image showing the surface profile before bonding [175].

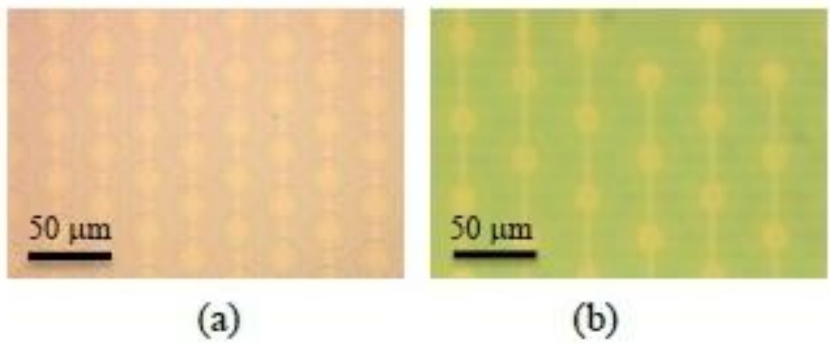

Figure 82: Plate pattern optical images: (a) Cells with partially etched plates on the clamped side. (b) Cells with flat plates [175].

4.4.3. Measurements

The immersion test was performed in a tank filled with water. The frequency response of the element in transmit was measured using a hydrophone (Model HGL-0200, Onda Corporation, Sunnyvale, CA) at a distance of 5mm. The element was biased at 50-V DC and a 20 V pulse excitation with 13ns pulse width was applied using a pulser/receiver (Model 5073PR, Olympus Corporation, Waltham, MA.

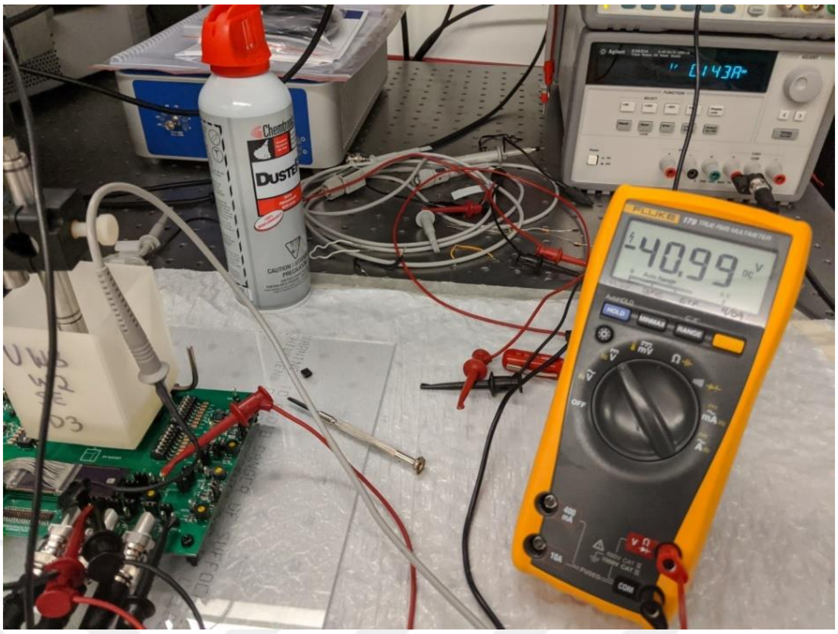

Figure 83: Experimental setup [176]

The signal received by the hydrophone was collected and FFT was applied to obtain the corresponding frequency spectrum (Figure 83). The data was corrected for the pulse spectrum. The frequency spectrum shows the transducer center frequency is 13.8 MHz and the 3-dB FBW is 135%.

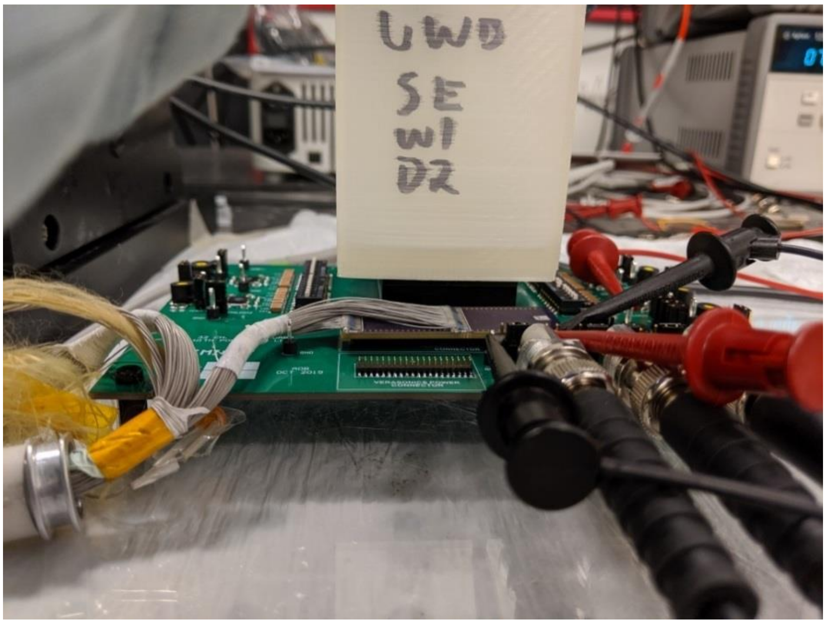

Figure 84: The IC and water filled tank used in the experiment [176]

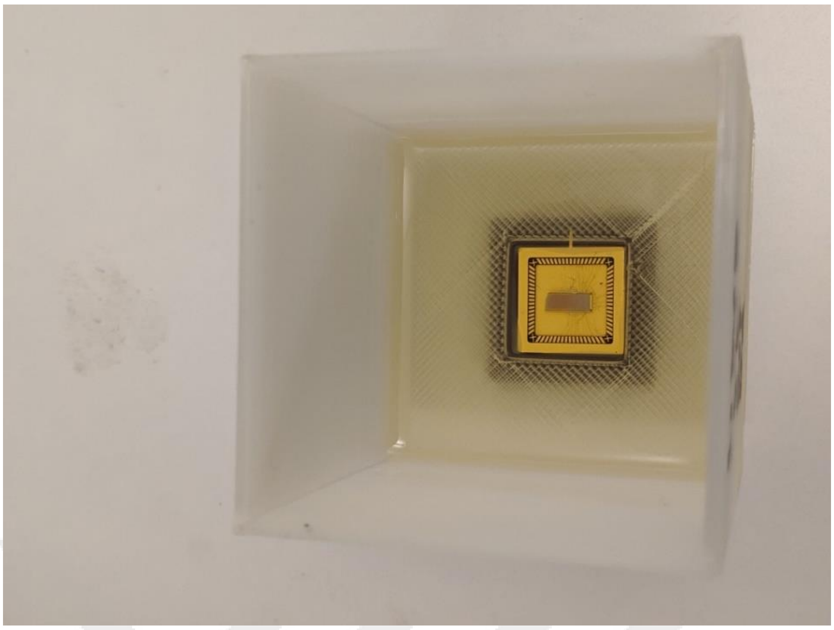

Figure 85: The 1D CMUT array used in the experiment [176]

The experimental and FEM results which are provided in Figure 86 belongs to a slightly thicker CMUT design. In the design; the thickness of passivation silicon nitride layer was 220nm, the silicon layer was 450nm and the silicon mass on top was 320nm. The radius of the plate and mass were 13um and 10um, respectively. The post width was 3um and the cavity height was 0.25um. The experimental and FEM were found to be matched well. The 3dB low and high cut off was found 5.5 MHz and 21 MHz, respectively. The design was 200nm thicker in total and the mass thickness is 80nm thinner than the optimized design and hence the bandwidth that was obtained was smaller compared to our FEM optimized model.

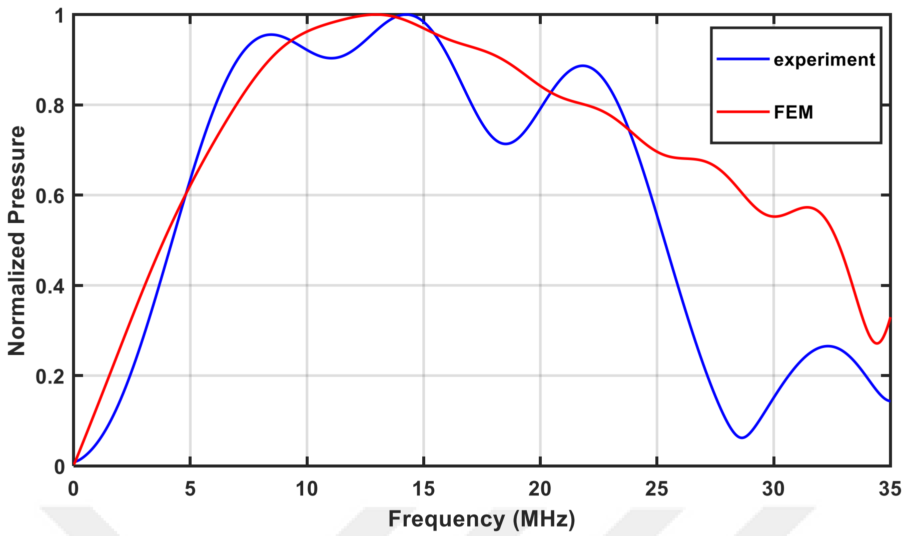

Figure 86: Verification of 3D FEM with experimental data

We demonstrated design of a UWB CMUTs adding a mass on the CMUT to modify the bandwidth on the transducer. While the additional mass gives more control on third mode and hence on bandwidth, etching the center of the mass gives more control over the fundamental mode. Therefore, low cut off and high cut off frequencies can be designed independently. We developed UWB 2-D and 3-D CMUT finite element models for acoustic angiography. The plate & mass dimensions, radius and thickness, also electrode radius were optimized to maximize bandwidth. We demonstrated low transmit around 2 MHz and high receive around 33 MHz. With such a CMUT, super-harmonics coming from excited MCAs can be detected and therefore, tissue separation from surrounding medium will be much easier.

CHAPTER V

CONCLUSION

The contribution of this thesis is twofold. First, we developed an accurate equivalent circuit and second, we designed an ultra-wide bandwidth CMUT using a novel non-uniform membrane geometry.

Equivalent circuit modeling approach is valuable because it provides quick estimates of the device performance. The major parameters of a CMUT transducer are the output pressure and the bandwidth. These calculations typically take couple of hours for a given membrane geometry using FEM since one needs to model the propagation medium where the medium has to be extended for multiple wavelengths to prevent reflections coming back to the membrane surface cluttering the results. Up to date, the most accurate equivalent circuit modeling included the higher order resonances to estimate the bandwidth. This approach works well when the second resonance peak is away from the first resonance. However, for relatively thin and small membrane geometries the second resonance is close to the first resonance therefore the anti-resonance usually determines the bandwidth of the transducer. In this thesis, we presented an equivalent circuit which includes the effect of the anti-resonance therefore the proposed method works for all the membrane geometries regardless of the aspect ratio of the membrane.

In the second part of the thesis we developed an ultrawide bandwidth transducer for harmonic imaging. If the membrane geometry is kept uniform, the maximum bandwidth that can be achieved is typically limited to 6-7 MHz around 10 MHz. This bandwidth is typically limited by the anti-resonance since small and thin membranes generate larger bandwidth. To push the anti-resonance to a higher frequency, one can use a non-uniform membrane geometry as shown in this thesis. But the location of the non-uniformity needs to be optimized. In this thesis, we proposed a novel membrane geometry as well as we optimized the geometry to obtain an exceptionally large bandwidth. We used 2D FEM analysis for this optimization since the equivalent circuit models only works for uniform membranes. We also verified the geometry using 3D FEM models as well as experimental measurements to demonstrate 30 MHz bandwidth which is very desirable for tissue harmonic imaging.

In the scope of this thesis we demonstrated the design and the operation of the wide bandwidth CMUTs. In the future, we are planning to use the fabricated CMUT arrays in a medical imaging set-up to demonstrate tissue harmonic imaging with enhanced contrast.

BIBLIOGRAPHY

[1] Karl Theo Dussik, Weitere Ergebnisse, “der Ultraschalluntersuchung bei Gehirnerkrankungen Acta Neurochirurgica”, Springer Verlag Wien, Volume 2, Numbers 3-4, September 1952, 379 - 401.

[2] Wild J. J, Reid J. M., “Further pilot echographic studies on the histologic structure of tumors of the living intact human breast”, Am J Pathol. 1952;28(5):839-861.

[3] Donald, I., Mac Vicar, J, and Brown, T, G., “Investigation of abdominal masses bu pulsed ultrasound”, Lancet 1: 1188,1958.

[4] Stuart Campell, “Placental localization by ultrasonic compound scanning”, J.Obstet. Gynaec. Brit. Cwlth. Oct. 1968. Vol. 75. pp. 1007-1013.

[5] Olaf T. Von Ramm and Frederick L. Thurstone, “Cardiac Imaging Using a Phased Array Ultrasound System”, 1976, 53 (2), 258-262

[6] Robert W. Gill, “Measurement of blood flow by ultrasound: Accuracy and sources of error”, July–August, 1985,Volume 11, Issue 4, Pages 625–641

[7] Cammarota T, Pinto F, Magliaro A, et al. “Current uses of diagnostic highfrequency ultrasound in dermatology”, Eur J Radiol. 1998;27(suppl 2):S215- S223.

[8] Chimenti, S., Carlo, E., Masson, S., Bai, A., and Latini, R. (2004). “Myocardial infarction: animal models. Methods”, Mol. Med. 98: 217 – 226, 18

[9] Haller, MI., Khuri-Yakub BT., “A surface micromachined electrostatic ultrasonic air transducer”, *Proc. IEEE Ultrason. Symp.*; 1994. p. 1241-1244.

[10] I. Ladabaum, Xuecheng Jin, H. T. Soh, A. Atalar and B. t. Khuri-Yakub, "Surface micromachined capacitive ultrasonic transducers", *IEEE Transactions on Ultrasonics, Ferroelectrics, and Frequency Control*, vol. 45, no. 3, pp. 678-690, May 1998.

[11] Xuecheng Jin, I. Ladabaum and B. T. Khuri-Yakub, "The microfabrication of capacitive ultrasonic transducers", *Journal of Microelectromechanical Systems*, vol. 7, no. 3, pp. 295-302, Sept. 1998.

[12] Xuecheng Jin, I. Ladabaum, F. L. Degertekin, S. Calmes and B. T. Khuri-Yakub, "Fabrication and characterization of surface micromachined capacitive ultrasonic immersion transducers," in *Journal of Microelectromechanical Systems*, vol. 8, no. 1, pp. 100-114, March 1999.

[13] Schindel DW, Hutchins DA. “The design and characterization of micromachined aircoupled capacitance transducers”. *IEEE Trans. Ultrason., Ferroelect., Freq. Contr*. Jan..1995 vol. UFFC-42:42–50.

[14] M. I. Haller and B. T. Khuri-Yakub, "A surface micromachined electrostatic ultrasonic air transducer," in *IEEE Transactions on Ultrasonics, Ferroelectrics, and Frequency Control*, vol. 43, no. 1, pp. 1-6, Jan. 1996.

[15] P. Eccardt, K. Niederer, T. Scheiter and C. Hierold, "Surface micromachined ultrasound transducers in CMOS technology," *IEEE Ultrasonics Symposium. Proceedings*, San Antonio, TX, USA, 1996, pp. 959-962 vol.2.

[16] P. C. Eccardt, K. Niederer and B. Fischer, "Micromachined transducers for ultrasound applications," *IEEE Ultrasonics Symposium Proceedings*. An International Symposium (Cat. No.97CH36118), Toronto, Ont., Canada, 1997, pp. 1609-1618 vol.2.

[17] Cianci E, Foglietti V, Caliano G, Pappalardo, Fabrication of capacitive ultrasonic transducers by a low temperature and fully surface-micromachined process, Journal of the International Societies for Precision Engineering and Nanotechnology 26 (2002) 347–354.

[18] [18] Yongli Huang, A. S. Ergun, E. Haeggstrom, M. H. Badi and B. T. Khuri-Yakub, "Fabricating capacitive micromachined ultrasonic transducers with wafer-bonding technology," in *Journal of Microelectromechanical Systems*, vol. 12, no. 2, pp. 128-137, April 2003.

[19] Soh H.T., Ladabaum I., Atalar A., Quate C.F., Khuri-Yakub B.T., “Silicon micromachined ultrasonic immersion transducers”. *Appl. Phys. Lett*. 1996, 69, 3674–3676.

[20] J. Knight and F. Degertekin, “Capacitive micromachined ultrasonic transducers for forward looking intravascular imaging arrays.” in *Proc. of IEEE Ultrasonics Symposium*, 2002, pp. 1079–1082.

[21] C. Bayram, S. Olcum, M. N. Senlik and A. Atalar, "Bandwidth improvement in a cMUT array with mixed sized elements," *IEEE Ultrasonics Symposium*, 2005., Rotterdam, The Netherlands, 2005, pp. 1956-1959.

[22] N. A. Hall, R. Guldiken, J. McLean and F. L. Degertekin, "Modeling and design of CMUTs using higher order vibration modes [capacitive micromachined ultrasonic transducers]," *IEEE Ultrasonics Symposium*, 2004, Montreal, Quebec, Canada, 2004, pp. 260-263 Vol.1.

[23] Yongli Huang, E. O. Haeggstrom, Xuefeng Zhuang, A. S. Ergun and B. T. Khuri-Yakub, "Optimized membrane configuration improves CMUT performance," *IEEE Ultrasonics Symposium,* 2004, Montreal, Quebec, Canada, 2004, pp. 505-508 Vol.1.

[24] Serena H. Wong, Ira O. Wygant, David T. Yeh, Xuefeng Zhuang, Baris Bayram, Mario Kupnik, Omer Oralkan, A. Sanli Ergun, Goksen G. Yaralioglu, and Butrus T. Khuri-Yakub, "Capacitive Micromachined Ultrasonic Transducer Arrays for Integrated Diagnostic/Therapeutic Catheters", *AIP Conference Proceedings* 829, 395 (2006)

[25] M. N. Senlik, S. Olcum and A. Atalar, "Improved performance of cMUT with nonuniform membranes," *IEEE Ultrasonics Symposium,* 2005., Rotterdam, The Netherlands, 2005, pp. 597-600.

[26] Hyo-Seon Yoon, Min-Chieh Ho, Nikhil Apte, Paul Cristman, Srikant Vaithilingam, Mario Kupnik, Kim Butts-Pauly, and Butrus T. Khuri-Yakub, "Fabrication of CMUT Cells with Gold Center Mass for Higher Output Pressure", *AIP Conference Proceedings* 1359, 183 (2011).

[27] M. Sato, Y. Hirai, K. Sugano, T. Tsuchiya, O. Tabata, "Capacitive micromachined ultrasonic transducers with novel membrane design*", Procedia Chemistry* Volume 1, Issue 1, September 2009, Pages 389-392

[28] Tahereh Arezoo Emadi, Douglas Andrew Buchanan, "A novel 6 × 6 element MEMS capacitive ultrasonic transducer with multiple moving membranes for high performance imaging applications", *Sensors and Actuators* A: Physical, Volume 222, 1 February 2015, Pages 309-313

[29] Yuanyu Yu, Sio Hang Pun, Peng Un Mak, Ching-Hsiang Cheng, Jiujiang Wang, IEEE, Pui-In Mak, and Mang I Vai, "Design of a Collapse-Mode CMUT With an Embossed Membrane for Improving Output Pressure", *IEEE Transactions on Ultrasonics, Ferroelectrics, and Frequency Control*, Vol. 63, No. 6, June 2016.

[30] Xiao Jiang, Yuanyu Yu, Jiujiang Wang, Xin Liu, U. Kin Che , Sio Hang Pun, Mang I. Vai, and Peng Un Mak, "Reception Performance Enhancement of Capacitive Micromachined Ultrasonic Transducers Via Modified Membrane Structures", Springer Nature Singapore Pte Ltd. 2017 J. Goh et al. (eds.), *The 17th International Conference on Biomedical Engineering IFMBE Proceedings* 61.

[31] Byung Chul Lee, Amin Nikoozadeh, Kwan Kyu Park and Butrus T. Khuri-Yakub, "High-Efficiency Output Pressure Performance Using Capacitive Micromachined Ultrasonic Transducers with Substrate-Embedded Springs", *Sensors 2018*, 18, 2520; doi:10.3390/s18082520.

[32] Yuanyu Yu, Jiujiang Wang, Sio Hang Pun, Ching-Hsiang Cheng, Kin Fong Lei, Mang I Vai, Shuang Zhang, and Peng Un Mak, "Fabrication of embossed capacitive micromachined ultrasonic transducers using sacrificial release process", *IEICE Electronics Express,* 2018, Vol.16, No.2, 1–11.

[33] Rasim O. Guldiken, Jaime Zahorian, F. Y. Yamaner, and F. Levent Degertekin, "Dual-Electrode CMUT With Non-Uniform Membranes for High Electromechanical Coupling Coefficient and High Bandwidth Operation", *IEEE Transactions on Ultrasonics, Ferroelectrics, and Frequency Control*, vol. 56, no. 6, June 2009.

[34] Yongli Huang, Xuefeng Zhuang, Edward O. Haggstrom, A. Sanli Ergun, Ching-Hsiang Cheng, and Butrus T. Khuri-Yakub, "Capacitive micromachined ultrasonic transducers with piston-shaped membranes: Fabrication and Experimental Characterization", *IEEE Transactions on Ultrasonics, Ferroelectrics, and Frequency Control*, Vol. 56, No. 1, January 2009.

[35] Anthony Novell, Christopher B. Arena, Sandeep Kasoji, and Paul A. Dayton, "Optimization of Multi-Pulse Sequences For Nonlinear Contrast Agent Imaging Using a cMUT array", *Phys Med Biol*. 2015 April 21; 60(8): 3111–3127.

[36] Frinking PJ, Bouakaz A, Kirkhorn J, Ten Cate FJ, De Jong N. "Ultrasound contrast imaging: current and new potential methods", *Ultrasound in Medicine & Biology*, Volume 26, Issue 6, July 2000, Pages 965-975.

[37] Ryan C. Gessner, C. Brandon Frederick, F. Stuart Foster, and Paul A. Dayton, "Acoustic Angiography: A New Imaging Modality for Assessing Microvasculature Architecture", Hindawi Publishing Corporation International, *Journal of Biomedical Imaging* Volume 2013, Article ID 936593.

[38] [38] Sarah E. Shelton, Yueh Z. Lee, Mike Lee, Emmanuel Cherin, F. Stuart Foster, Stephen R. Aylward, and Paul A. Dayton, "Quantification of microvascular tortuosity during tumor evolution utilizing acoustic angiography", *Ultrasound in Medicine & Biology*, Volume 41, Issue 7, July 2015, Pages 1896-1904

[39] Annette Lohfink and Peter-Christian Eccardt, "Linear and Nonlinear Equivalent Circuit Modeling of CMUTs", *IEEE transactions on Ultrasonics, Ferroelectrics, and Frequency Control,* Vol. 52, No. 12, December 2005.

[40] Goksen G. Yaralioglu, A. Sanli Ergun, and Butrus T. Khuri-Yakub, "Finite-Element Analysis of CapacitiveMicromachined Ultrasonic Transducers", *IEEE Transactions on Ultrasonics, Ferroelectrics, and Frequency Control*, Vol. 52, no. 12, December 2005.

[41] Goksen G. Yaralioglu , Baris Bayram, Amin Nikoozadeh, B.T. Pierre Khuri-Yakub, "Finite Element Modeling of Capacitive Micromachined Ultrasonic Transducers", Proc.

SPIE 5750, Medical Imaging 2005: *Ultrasonic Imaging and Signal Processing*, 12 April 2005.

[42] S.J. Ballandras, M. Wilm, J.-F. Gelly, "Theoretical analysis of micro-machined ultrasonic transducer using a simple 1-D model", *Ultrasonics Ferroelectrics and Frequency Control IEEE Transactions* on, vol. 53, no. 1, pp. 209-223, 2006.

[43] B. Bayram, G. G. Yaralioglu, A. S. Ergun, M. Oralkan and B. T. Khuri-Yakub, "Dynamic FEM analysis of multiple cMUT cells in immersion [capacitive micromachined ultrasonic transducers]," *IEEE Ultrasonics Symposium*, 2004, Montreal, Quebec, Canada, 2004, pp. 252-255 Vol.1.

[44] B. Bayram, M. Kupnik, G. G. Yaralioglu, O. Oralkan, A. S. Ergun, D.-S. ¨Lin, S. H. Wong, and B. T. Khuri-Yakub, “Finite element modeling andexperimental characterization of crosstalk in 1-D CMUT arrays,” *IEEETrans. Ultrason., Ferroelec., Freq. Contr*., vol. 54, no. 2, pp. 418–430,2007.

[45] G. Wojcik, J. Mould, P. Reynolds, A. Fitzgerald, P. Wagner, and I. Ladabaum, “Time-domain models of MUT array cross-talk in silicon substrates,” in Proc. *IEEE Ultrason. Symp*., 2000, pp. 909–914.

[46] M. Engholm et al., "Simulating CMUT arrays using time domain FEA," *2017 IEEE International Ultrasonics Symposium (IUS)*, Washington, DC, 2017, pp. 1-4.

[47] Theoretical investigation on the dynamic performance of CMUT for design optimization, TingYu, WenchaoZhou, PengXu, FengqiYuaQinQianb, *Acta Mechanica Solida Sinica* Volume 26, Issue 1, February 2013, Pages 99-110

[48] S. Ballandras et al., "Simulation of cMUT radiating in water using a mixed finite element/boundary element approach," *2002 IEEE Ultrasonics Symposium*, 2002. Proceedings., Munich, Germany, 2002, pp. 1075-1078 vol.2.

[49] S. Satir, J. Zahorian and F. L. Degertekin, "A large-signal model for CMUT arrays with arbitrary membrane geometry operating in non-collapsed mode," in *IEEE Transactions on Ultrasonics, Ferroelectrics, and Frequency Control*, vol. 60, no. 11, pp. 2426-2439, November 2013.

[50] M. Kaltenbacher, H. Landes, K. Niederer, and R. Lerch, “3D simulation of Controlled Micromachined Capacitive Ultrasound Transducers,” *Ultrasonics, 1999 IEEE Symposium* on, Vol 2, pp. 1155-1158, Oct. 1999.

[51] Mason, W.P. Electromechanical Transducers and Wave Filters, D. Van Nostrand: New York, NY, USA, 1942.

[52] A. Caronti, G. Caliano, A. Iula and M. Pappalardo, "An accurate model for capacitive micromachined ultrasonic transducers," in *IEEE Transactions on Ultrasonics, Ferroelectrics, and Frequency Control*, vol. 49, no. 2, pp. 159-168, Feb. 2002.

[53] G. G. Yaralioglu, M. H. Badi, A. S. Ergun, and B. T. Khuri-Yakub, "Improved equivalent circuit and finite element method modeling of capacitive micromachined ultrasonic transducers," *in Proc. IEEE Ultrason. Symp.*, 2003, pp. 469–472.

[54] H. K. Oguz, A. Atalar and H. Köymen, "Equivalent circuit-based analysis of CMUT cell dynamics in arrays," in *IEEE Transactions on Ultrasonics, Ferroelectrics, and Frequency Control*, vol. 60, no. 5, pp. 1016-1024, May 2013.

[55] Ayhan Bozkurt, "A lumped-circuit model for the radiation impedance of a circular piston in a rigid baffle, *IEEE Transactions on Ultrasonics, Ferroelectrics, and Frequency Control*, vol. 55, no. 9, September 2008.

[56] H. Köymen, A. Atalar and H. K. Oğuz, "Designing circular CMUT cells using CMUT biasing chart,*" 2012 IEEE International Ultrasonics Symposium*, Dresden, 2012, pp. 975-978.

[57] S. Olcum, F. Y. Yamaner, A. Bozkurt, H. Koymen and A. Atalar, "An equivalent circuit model for transmitting capacitive micromachined ultrasonic transducers in collapse mode," *in IEEE Transactions on Ultrasonics, Ferroelectrics, and Frequency Control*, vol. 58, no. 7, pp. 1468-1477, July 2011.

[58] Shengping Mao, Xavier Rottenberg, V Rochus, P Czarnecki, P Helin, S Severi, B Nauwelaers and H A C Tilmans, "Modal analysis based equivalent circuit model and its verification for a single cMUT cell", 19 January 2017 • © *2017 IOP Publishing Ltd*.

[59] Shengping Mao et al., "A general multi-mode lumped equivalent circuit model for circular cMUT cells," *2016 IEEE International Ultrasonics Symposium (IUS)*, Tours, 2016, pp. 1-4.

[60] http://bme.elektro.dtu.dk/jw/webbook/Ultrasound/main.pdf, [accessed at 02.04.2020]

[61] http://eeweb.poly.edu/~yao/EL5823/Ultrasound_imaging_ch11.pdf, accessed at [09.04.2020]

[62] T. L. Szabo, Diagnostic ultrasound imaging: inside out: Academic Press, 2004.

[63] Gokce Gurun, Integrated Electronics Design for high-Frequency Intravascular Ultrasound Imaging, A dissertation of Georgia Institute of Technology, December 2011.

[64] https://thoracickey.com/echocardiography/, accessed 15.04.2020.

[65] Hyo-Seon Yoon, Capacıtive Micromachined Ultrasonic Transducers (CMUTs) for Therapeutic Applications, A Dissertation of Stanford University, December 2015.

[66] Wonseok Lee, Yongrae Roh, “Ultrasonic transducers for medical diagnostic imaging”, *Korean Society of Medical and Biological Engineering and Springer 2017.*

[67] O. Oralkan et al., "Initial pulse-echo imaging results with one-dimensional capacitive micromachined ultrasonic transducer arrays," *2000 IEEE Ultrasonics Symposium. Proceedings*. An International Symposium (Cat. No.00CH37121), San Juan, Puerto Rico, USA, 2000, pp. 959-962 vol.1.

[68] U. Demirci, O. Oralkan, J. A. Johnson, A. S. Ergun, M. Karaman and B. T. Khuri-Yakub, "Capacitive micromachined ultrasonic transducer arrays for medical imaging: experimental results," *2001 IEEE Ultrasonics Symposium. Proceedings*. An International Symposium (Cat. No.01CH37263), Atlanta, GA, USA, 2001, pp. 957-960 vol.2.

[69] Omer Oralkan, A.Sanli Ergun, Jeremy A.Johnson, Mustafa Karaman, Utkan Demirci, Kambiz Kaviani, Thomas H. Lee and Butrus T.Khur-Yakub, “Capacitive Micromachined Ultrasonic Transducers: Next-Generation Arrays for Acoustic Imaging*?”, IEEE Transactions on Ultrasonics, Ferroelectrics and Frequency Control*, Vol. 49, No.11, November 2002.

[70] D. M. Mills and L. S. Smith, "Real-time in-vivo imaging with capacitive micromachined ultrasound transducer (cMUT) linear arrays," *IEEE Symposium on Ultrasonics*, 2003, Honolulu, HI, USA, 2003, pp.568-571 vol. 1

[71] Douglas G. Wildes, Richard Y. Chiao, Chris M. W. Daft, K. W. Rigby, Member, L. Scott Smith and Kai E. Thomenius, “Elevation Performance of 1.25D and 1.5D Transducer Arrays*”, IEEE Transactions on Ultrasonics, Ferroelectrics and Frequency Control*, vol. 44, no. 5, September 1997.

[72] B. Savord and R. Solomon, "Fully sampled matrix transducer for real time 3D ultrasonic imaging," in Ultrasonics, *2003 IEEE Symposium* on, 2003, pp. 945-953 Vol.1.

[73] C. Daft, S. Panda, P. Wagner, and I. Ladabaum, "Two approaches to electronically scanned 3D imaging using cMUTs," in *Ultrasonics Symposium*, 2006. IEEE, 2006, pp. 685-688.

[74] S. W. Smith and E. D. Light, “Two-dimensional array transducers using thick film connection technology*,” IEEE Trans. Ultrason., Ferroelect., Freq. Contr*., vol. 40, no. 6, pp. 727–734, 1993

[75] R. E. Davidsen and S. W. Smith, "Two-dimensional arrays for medical ultrasound using multilayer flexible circuit interconnection," in *IEEE Transactions on Ultrasonics, Ferroelectrics, and Frequency Control*, vol. 45, no. 2, pp. 338-348, March 1998.

[76] R. A. Noble et al., "Cost-effective and manufacturable route to the fabrication of high-density 2D micromachined ultrasonic transducer arrays and (CMOS) signal conditioning electronics on the same silicon substrate," *2001 IEEE Ultrasonics Symposium. Proceedings. An International Symposium* (Cat. No.01CH37263), Atlanta, GA, USA, 2001, pp. 941-944 vol.2.

[77] B. Savord and R. Solomon, "Fully sampled matrix transducer for real time 3D ultrasonic imaging," in *Ultrasonics, 2003 IEEE Symposium* on, 2003, pp. 945-953 Vol.1.

[78] O. Oralkan, Xuecheng Jin, F. L. Degertekin and B. T. Khuri-Yakub, "Simulation and experimental characterization of a 2-D capacitive micromachined ultrasonic transducer array element," in *IEEE Transactions on Ultrasonics, Ferroelectrics, and Frequency Control*, vol. 46, no. 6, pp. 1337-1340, Nov. 1999.

[79] X. Zhuang, I. O. Wygant, D. -. Lin, M. Kupnik, O. Oralkan and B. T. Khuri-Yakub, "Wafer-bonded 2-D CMUT arrays incorporating through-wafer trench-isolated interconnects with a supporting frame," in *IEEE Transactions on Ultrasonics, Ferroelectrics, and Frequency Control*, vol. 56, no. 1, pp. 182-192, January 2009.

[80] I. O. Wygant et al., "2C-3 An Integrated Circuit with Transmit Beamforming and Parallel Receive Channels for 3D Ultrasound Imaging: Testing and Characterization," *2007 IEEE Ultrasonics Symposium Proceedings*, New York, NY, 2007, pp. 25-28.

[81] T. Ma et al., "3-D Deep penetration photoacoustic imaging with a 2-D CMUT array," *2010 IEEE International Ultrasonics Symposium*, San Diego, CA, 2010, pp. 375-377.

[82] Anshuman Bhuyan , Jung Woo Choe , Byung Chul Lee , Ira Wygant , Amin Nikoozadeh , Omer Oralkan, Butrus T. Khuri-Yakub, “3D Volumetric Ultrasound Imaging with a 32×32 CMUT Array Integrated with Front-End ICs Using Flip-Chip Bonding Technology”, *2013 IEEE International Solid-State Circuits Conference.*

[83] http://www.ndt-kits.com/Matrix-2D-1.5D-Phased-Array-Transducer-UT0036-s-381-613.html, [accessed at 15.04.2020].

[84] J. A. Ketterling, O. Aristizabal, D. H. Turnbull and F. L. Lizzi, "Design and fabrication of a 40-MHz annular array transducer," in *IEEE Transactions on Ultrasonics, Ferroelectrics, and Frequency Control*, vol. 52, no. 4, pp. 672-681, April 2005.

[85] C. I. Zanelli, C. W. Hennige and N. T. Sanghvi, "Design and characterization of a 10 cm annular array transducer for high intensity focused ultrasound (HIFU)

applications," *1994 Proceedings of IEEE Ultrasonics Symposium*, Cannes, France, 1994, pp. 1887-1890 vol.3.

[86] Yang, Diwu; Ming, Zenglv; Zhou, Xin; Huang, Zhong; Xiao, Lijun, "Photoacoustic Imaging of Biological Tissues Based on Annular Transducer Array", *Nanoscience and Nanotechnology Letters*, Volume 8, Number 12.

[87] F. L. Degertekin, R. O. Guldiken and M. Karaman, "Annular-ring CMUT arrays for forward-looking IVUS: transducer characterization and imaging," in *IEEE Transactions on Ultrasonics, Ferroelectrics, and Frequency Control*, vol. 53, no. 2, pp. 474-482, Feb. 2006.

[88] D. T. Yeh, O. Oralkan, I. O. Wygant, M. O'Donnell and B. T. Khuri-Yakub, "3-D ultrasound imaging using a forward-looking CMUT ring array for intravascular/intracardiac applications," in *IEEE Transactions on Ultrasonics, Ferroelectrics, and Frequency Control*, vol. 53, no. 6, pp. 1202-1211, June 2006.

[89] Arditi M, Foster FS, Hunt JW. "Transient fields of concave annular arrays". *Ultrason. Imaging* 1981;3(1):37–61.

[90] Martinez O, Akhnak M, Ullate LG, de Espinosa FM. "A small 2D ultrasonic array for NDT applications". *NDT&E Int* 2003;36:57–63.

[91] Norton SJ. "Annular array imaging with full-aperture resolution". *J Acoust Soc Am* 1992;92(6):3202–6.

[92] Mondal S, Wilcox PD, Drinkwater BW." Design of two-dimensional ultrasonic phased array transducers". *Trans ASME—J Pressure Vessel Technol* 2005;127(3):336–44.

[93] Bruce W. Drinkwater, Paul D. Wilcox, "Ultrasonic arrays for non-destructive evaluation: A review", *NDT&E International 39* (2006) 525–541.

[94] https://www.imv-imaging.co.uk/veterinary-learning/small-animal-learning/general-imaging-techniques/new-year-s-resolutions/, accessed 16.02.2020

[95] W. G. Cady, Piezoelectricity. New York: McGraw-Hill, 1946.

[96] G. H. Haertling, "Ferroelectric ceramics: history and technology", *J Am Ceram Soc.* 82, 797–818 (1999).

[97] P. K. Panda, "Review: Environmental friendly lead-free piezoelectric materials", *J Mater Sci*., 44, 5049–5062 (2009).

[98] E. Ringgaard, T. Wurlitzer, and W. W. Wolny, "Properties of lead-free piezoceramics based on alkali niobates", *Ferroelectrics*. 319, 323–333 (2005).

[99] T. Takenaka and H. Nagata, "Current status and prospects of lead-free piezoelectric ceramics", *J Euro Ceram Soc*. 25, 2693–2700 (2005)

[100] W. Liu and X. Ren, “Large piezoelectric effect in Pb-free ceramics”, *Phy Rev Lett*. 103, 257602 (2009)

[101] Sai babu KARIMISETTI, Piezo electric ceramic: Manufacture, mechanical and electrical analysis, A Master’s degree Thesis of Universite Francois – Rabelais, Tours.

[102] https://www.pc-control.co.uk/piezoelectric_effect.htm, accessed 23.04.2010

[103] Victor I. Mikla, Victor V. Mikla, “Medical Imaging Technology”, *Elsevier Science*, August 2013.

[104] M. Yoichi, “Applications of piezoelectric actuators”, *NEC Technical Journal*. 1, 82–86, (2006).

[105] E. F. Crawley, “Intelligent structures for aerospace: A technology overview and assessment”, *AIAA Journal*, 32, 1689–1699 (1994).

[106] K. Uchino, “Ceramic actuators: principles and applications”, *Mater Res Soc Bull* 18, 42–48 (1993).

[107] J. F. Tressler, “Piezoelectric transducer designs for sonar applications”. In A. Safari, and E. K. Akdogan, eds. Piezoelectric and Acoustic Materials for Transducer Applications: Springer publication; 2008: 217–239.

[108] H. A. Sodano and D. J. Inman, “A review of power harvesting from vibration using piezoelectric materials”, *The Shock and Vibration Digest*. 36, 197–205 (2004).

[109] B. Gromek and J. J. Shen, Multiple stack piezoelectric actuator for a fuel injector. United States Patent, 2000; 6345771.]

[110] Brown LF, “Ferroelectric Polymers: Current and Future Ultrasound Applications” *I992 IEEE Ultrasonics Symp. Proc*. 539, 1993.

[111] K. K. Shung and M. Zippuro, "Ultrasonic transducers and arrays," in *IEEE Engineering in Medicine and Biology Magazine*, vol. 15, no. 6, pp. 20-30, Nov.-Dec. 1996, doi: 10.1109/51.544509.

[112] [https://www.ndk.com/en/sensor/ultrasonic/basic02.html, [accessed at 20.04.2020]

[113] https://www.nde-ed.org/EducationResources/CommunityCollege/Ultrasonics/ EquipmentTrans/ characteristicspt.htm, [accessed at 02.12.2020]

[114] Kinsler LE, Frey AR, Coppens AB, Sanders, JV: Fundamentals ofAcoustics, 3rd Ed. John Wiley, New York, 1982.

[115] Xiao Zhang, Capacitive Micromachined Ultrasonic Transducers (CMUTs) on Glass Substrates for Next-Generation Medical Imaging and Beyond, A dissertation submitted to the Graduate Faculty of North Carolina State University, 2017.

[116] Cheng, X., Lemmerhirt, DF., Kripfgans, OD., Zhang, M., Yang, C., Rich, CA., Fowlkes, JB. “CMUT-IN-CMOS ultrasonic transducer arrays with on-chip electronics”. *Proc. Int. Conf. Solid-State Sensors and Actuators*; 2009. p. 1222-1225,

[117] Y. Tsuji, M. Kupnik and B. T. Khuri-Yakub, "Low temperature process for CMUT fabrication with wafer bonding technique," *2010 IEEE International Ultrasonics Symposium*, San Diego, CA, 2010, pp. 551-554.

[118] www.hitachi-medical.co.jp/medix/pdf/vol51/P31-34.pdf

[119] Danhua Zhao, S. Zhuang and R. Daigle, "A commercialized high frequency CMUT probe for medical ultrasound imaging," *2015 IEEE International Ultrasonics Symposium (IUS)*, Taipei, 2015, pp. 1-4.

[120] http://www.yole.fr/MedicalImaging_SolidStateIC.aspx#.Xl5TLiEzbDc, [accessed at 12.03.2020]

[121] O. Oralkan, B. Bayram, G.G. Yaralioglu, a S. Ergun, M. Kupnik, D.T. Yeh, I.O.Wygant, and B.T. Khuri-Yakub, “Experimental characterization of collapse-modeCMUT operation.,” *Ultrasonics, Ferroelectrics and Frequency Control, IEEE Transactions* on, vol. 53, Aug. 2006, pp. 1513-23.

[122] Huang Y., Ergun A.S., Haeggstrom E., Khuri-Yakub B.T., “Fabrication of Capacitive Micromachined Ultrasonic Transducers (CMUTs) Using Wafer Bonding Technology for Low Frequency (10 kHz–150 kHz) Sonar Applications”, *In Proceedings of the IEEE Oceans*, Biloxi, MI, USA, 29–31 October 2002; pp. 2322–2327.

[123] http://selimolcum.mit.edu/sites/default/files/documents/Olcum_PhD_Thesis.pdf, accessed at 05.03.2020],

[124] Der-Song Lin, Interface Engineering of Capacıtive Mıcromachined Ultrasonic Transducers for Medıcal Applications, a Dissertation of Stanford University , June 2011.

[125] Igal Ladabaum and B. T. Khuri-Yakub, “Micromachined ultrasonic transducers: 11.4 MHz transmission in air and more”, *Appl. Phys. Lett.* 68, 7 (1996).

[126] J. Knight, J. McLean and F. L. Degertekin, "Low temperature fabrication of immersion capacitive micromachined ultrasonic transducers on silicon and dielectric substrates," in *IEEE Transactions on Ultrasonics, Ferroelectrics, and Frequency Control*, vol. 51, no. 10, pp. 1324-1333, Oct. 2004

[127] D. Lin, X. Zhuang, S. H. Wong, A. S. Ergun, M. Kupnik and B. T. Khuri-Yakub, "6F-5 Characterization of Fabrication Related Gap-Height Variations in Capacitive Micromachined Ultrasonic Transducers," *2007 IEEE Ultrasonics Symposium Proceedings*, New York, NY, 2007, pp. 523-526.

[128] Cheng C.H., Chow E.M., Jin X., Ergun S., Khuri-Yakub B.T., An Efficient Electrical Addressing Method Using Through-Wafer Vias for Two-Dimensional Ultrasonic Arrays, In *Proceedings of the IEEE International Ultrasonics Symposium (IUS),* San Juan, PR, USA, 22–25 October 2000; pp. 1179–1182.

[129] I. O. Wygant et al., "Integration of 2D CMUT arrays with front-end electronics for volumetric ultrasound imaging," in *IEEE Transactions on Ultrasonics, Ferroelectrics, and Frequency Control*, vol. 55, no. 2, pp. 327-342, February 2008.

[130] A. Moini et al., "Fully integrated 2D CMUT ring arrays for endoscopic ultrasound," *2016 IEEE International Ultrasonics Symposium (IUS),* Tours, 2016, pp. 1-4.

[131] T. R. Anthony, "Forming electrical interconnections through semiconductor wafers", *J. Appl. Phys*. 52(8), August 1981.

[132] E. M. Chow, A. Partridge, C. F. Quate, T. W. Kenny, "Through-Wafer Electrical Interconnects Compatible with Stanford Semiconductor Processing", *Solid-state Sensor and Actuator Workshop*, Hilton Head Island, South Carolina, June 4-8, 2000, pp. 343-6 (2000).

[133] https://sst.semiconductor-digest.com/2005/04/through-wafer-via-etching/, [accessed at 16.04.2020]

[134] K. K. Park, H. Lee, M. Kupnik and B. T. Khuri-Yakub, "Fabrication of Capacitive Micromachined Ultrasonic Transducers via Local Oxidation and Direct Wafer Bonding," *in Journal of Microelectromechanical Systems*, vol. 20, no. 1, pp. 95-103, Feb. 2011.

[135] S. E. Alper and T. Akin, "A Single-Crystal Silicon Symmetrical and Decoupled MEMS Gyroscope on an Insulating Substrate," *J. Microelectromech. Syst*., vol. 14, no. 4, pp. 707–717, 2005. 138]

[136] S. E. Alper and T. Akin, "Symmetrical and decoupled nickel microgyroscope on insulating substrate," in *The 17th European Conference on Solid-State Transducers*, 2004, vol. 115, pp. 336–350

[137] Ayhan Bozkurt, Igal Ladabaum, Abdullah Atalar and Butrus T. Khuri-Yakub, "Theory and Analysis of Electrode Size Optimization for Capacitive Microfabricated Ultrasonic Transducers", *IEEE Transactions on Ultrasonics, Ferroelectrics, and Frequency Control*, vol. 46, no. 6, November 1999.

[138] B. Bayram, E. Haeggstrom, G. G. Yaralioglu and B. T. Khuri-Yakub, "A new regime for operating capacitive micromachined ultrasonic transducers," in *IEEE Transactions*

on Ultrasonics, Ferroelectrics, and Frequency Control, vol. 50, no. 9, pp. 1184-1190, Sept. 2003.

[139] Y. Roh and B. T. Khuri-Yakub, "Finite element analysis of underwater capacitor micromachined ultrasonic transducers," in *IEEE Transactions on Ultrasonics, Ferroelectrics, and Frequency Control*, vol. 49, no. 3, pp. 293-298, March 2002.

[140] B. Bayram, G. G. Yaralioglu, A. S. Ergun, and B. T. KhuriYakub, "Influence of the electrode size and location on the performance of a CMUT," in *Proc. IEEE Ultrason. Symp.*, 2001, pp. 949–952.

[141] H. Kagan Oguz, Selim Olcum, Muhammed N. Şenlik, Vahdettin Taş, Abdullah Atalar, and Hayrettin Köymen, "Nonlinear Modeling of an Immersed Transmitting Capacitive Micromachined Ultrasonic Transducer for Harmonic Balance Analysis", *IEEE Transactions on Ultrasonics, Ferroelectrics, and Frequency Control*, vol. 57, no. 2, February 2010

[142] Meirovitch L., 1975 Elements of Vibration Analysis, NewYork: McGraw-Hill.

[143] Harrie A C Tilmans, "Equivalent circuit representation of electromechanical transducers: II. Distributed-parameter systems", *J. Micromech. Microeng*. 7 (1997) 285–309.

[144] S.Timoshenko, Theory of Plates and Shells. New York:McGraw-Hill, 1940.

[145] M. Legros, A. Novell, A. Bouakaz, G. Férin, R. Dufait and D. Certon, "Tissue harmonic imaging with CMUTs," *2011 IEEE International Ultrasonics Symposium*, Orlando, FL, 2011, pp. 2249-2252

[146] M. A. Averkiou, D. N. Roundhill and J. E. Powers, "A new imaging technique based on the nonlinear properties of tissues," *1997 IEEE Ultrasonics Symposium Proceedings*. An International Symposium (Cat. No.97CH36118), Toronto, Ont., Canada, 1997, pp. 1561-1566 vol.2.

[147] Arash Anvari, Flemming Forsberg, Anthony E. Samir, "A Primer on the Physical Principles of Tissue Harmonic Imaging", *RadioGraphics* 2015; 35:1955–1964.

[148] E.L.Carstensen, W.K.Law, N.D.McKay, T.G.Muir, "Demonstration of nonlinear acoustical effects at biomedical frequencies and intensities", *Ultrasound in Medicine & Biology* Volume 6, Issue 4, 1980, Pages 359-36.

[149] F. Tranquart, N. Grenıer, V. Eder and L. Pourcelot, "Clinical use of ultrasound tissue harmonic imaging", *Ultrasound in Med. & Biol.*, Vol. 25, No. 6, pp. 889–894, 1999.

[150] Burns PN. "Harmonic imaging with ultrasound contrast agents", *La Radiologia Medica*, 01 May 1994, 87(5 Suppl 1):71-82.

[151] Mary M. Quien, Muhamed Saric, “Ultrasound imaging artifacts: How to recognize them and how to avoid them”, *2018 Wiley Periodicals, Inc., Echocardiography*. 2018;1–14.

[152] Buttery B, Davidson G. “The ghost artifact”. *J Ultrasound Med.* 1984;3:49–52.

[153] Feldman MK, Katyal S, Blackwood MS. US artifacts. Radiographics. 2009;29:1179–1189.

[154] Desser TS, Jeffrey RB ,”Tissue Harmonic Imaging Techniques: Physical Principles and Clinical Applications”, *Semin Ultrasound* CT MR. 2001 Feb;22(1):1-10.

[155] Barry B. Goldberg, Ji-Bin Liu and Flemming Forsberg, “Ultrasound contrast agents: A Review”, *Ultrasound in Med. & Biol*., Vol. 20, No. 4, pp. 319-333, 1994.

[156] P. N. T. Wells, “Ultrasound imaging”, *Phys. Med. Biol*. 51 (2006) R83–R98.

[157] P.N.T.Wells, “Ultrasound imaging”, *Journal of Biomedical Engineering* Volume 10, Issue 6, November 1988, Pages 548-55.

[158] Ainslie MA, Leighton TG ,”Review of scattering and extinction cross-sections, damping factors, and resonance frequencies of a spherical gas bubble”, *J Acoust Soc Am*. 2011 Nov;130(5):3184-208.

[159] Lei Fu, Heng-Te Ke, “Nanomaterials incorporated ultrasound contrast agents for cancer theranostics”, *Cancer biology and medicine*, August 13, 2016.

[160] J. A. Hossack, P. Mauchamp and L. Ratsimandresy, "A high bandwidth transducer optimized for harmonic imaging," *2000 IEEE Ultrasonics Symposium. Proceedings*. An International Symposium (Cat. No.00CH37121), San Juan, Puerto Rico, USA, 2000, pp. 1021-1024 vol.2.

[161] G. Ferin, M. Legros, N. Felix, C. Notard and L. Ratsimandresy, "3F-6 Ultra-Wide Bandwidth Array for New Imaging Modalities," *2007 IEEE Ultrasonics Symposium Proceedings*, New York, NY, 2007, pp. 204-207.

[162] Foster FS, Harasiewicz KA, Sherar MD., “A history of medical and biological imaging with polyvinylidene fluoride (PVDF) transducers”, *IEEE Trans Ultrason Ferroelectr Freq Control.* 2000;47(6):1363-71.

[163] K.A. Snook, Jian-Zhong Zhao, C.H.F. Alves, J.M. Cannata, Wo-Hsing Chen, R.J. Meyer, T.A. Ritter ,”Design, fabrication, and evaluation of high frequency, single element transducers incorporating different materials”, *IEEE Transactions on Ultrasonics, Ferroelectrics, and Frequency Control*, Volume: 49 , Issue: 2 , Feb. 2002.

[164] J. Ma, K. H. Martin, P. A. Dayton and X. Jiang, "A preliminary engineering design of intravascular dual-frequency transducers for contrast-enhanced acoustic angiography and molecular imaging," in *IEEE Transactions on Ultrasonics, Ferroelectrics, and Frequency Control*, vol. 61, no. 5, pp. 870-880, May 2014.

[165] Anthony Novell, Jean-Michel Escoffre, AyacheBouakaz ,Second Harmonic and Subharmonic for Non-Linear Wideband Contrast Imaging Using a Capacitive Micromachined Ultrasonic Transducer Array, *Ultrasound in Medicine & Biology* Volume 39, Issue 8, August 2013, Pages 1500-151.

[166] D.T. Yeh, O. Oralkan, I.O. Wygant, M. O'Donnell, B.T. Khuri-Yakub ,"3-D Ultrasound Imaging Using a Forward-Looking CMUT Ring Array for Intravascular/Intracardiac Applications*", IEEE Transactions on Ultrasonics, Ferroelectrics, and Frequency Control* Volume: 53 , Issue: 6 , June 2006.

[167] M. M. Mahmud et al., "Improved CMUT structure and method of operation for dual-frequency acoustic angiography," *2017 IEEE International Ultrasonics Symposium (IUS)*, Washington, DC, 2017, pp. 1-4.

[168] O. J. Adelegan, R. E. Kemal, F. Y. Yamaner, P. A. Dayton and Ö. Oralkan, "Design and Fabrication of High-Frequency Ultra-Wideband 1D CMUT Arrays for Acoustic Angiography Applications - Preliminary Results," *2018 IEEE International Ultrasonics Symposium (IUS)*, Kobe, 2018, pp. 1-4.

[169] F. Y. Yamaner, X. Zhang and Ö. Oralkan, "A three-mask process for fabricating vacuum-sealed capacitive micromachined ultrasonic transducers using anodic bonding," *in IEEE Transactions on Ultrasonics, Ferroelectrics, and Frequency Control*, vol. 62, no. 5, pp. 972-982, May 2015.

[170] Hedrick, W. R., & Metzger, L. (2005). "Tissue Harmonic Imaging: A Review*". Journal of Diagnostic Medical Sonography*, 21(3), 183–189.

[171] William R. Hendee, Imaging in medical diagnosis and theraphy, 2013, CRC press.

[172] Thomas L. Szabo, Diagnostic Ultrasound Imaging: Inside Out, 2004, Elsevier Inc.

[173] Alessandro S. Savoia, Giosuè Caliano , "MEMS-Based Transducers (CMUT) and Integrated Electronics for Medical Ultrasound Imaging", *Springer International Publishing*, 2017

[174] Nanofabrication facility, North Carolina State University, North Carolina, USA

[175] O. J. Adelegan, R. E. Kemal, F. Y. Yamaner, P. A. Dayton and Ö. Oralkan, "Design and Fabrication of High-Frequency Ultra-Wideband 1D CMUT Arrays for Acoustic Angiography Applications - Preliminary Results," *2018 IEEE International Ultrasonics Symposium (IUS)*, Kobe, 2018, pp. 1-4, doi: 10.1109/ULTSYM.2018.8579874.

[176] Photo credit to Jeanne Sanders, PhD candidate in the depatment of Electrical Engineering in North Carolina State University, North Carolina, USA

[177] Graphs credit to Jeanne Sanders, PhD candidate in the depatment of Electrical Engineering in North Carolina State University, North Carolina, USA